Combined experimental and computational study of the meta-stable Mg-Ti-H system

Ingvild Julie Thue Jensen

Thesis submitted in partial fulfillment
of the requirements for the degree of
Philosophiae Doctor

Department of Physics
University of Oslo

December 2012

© Ingvild Julie Thue Jensen, 2013

Series of dissertations submitted to the
Faculty of Mathematics and Natural Sciences, University of Oslo
No. 1327

ISSN 1501-7710

All rights reserved. No part of this publication may be
reproduced or transmitted, in any form or by any means, without permission.

Cover: Inger Sandved Anfinsen.
Printed in Norway: AIT Oslo AS.

Produced in co-operation with Akademika publishing.
The thesis is produced by Akademika publishing merely in connection with the
thesis defence. Kindly direct all inquiries regarding the thesis to the copyright
holder or the unit which grants the doctorate.

To my parents

Summary

$Mg_{1-y}Ti_yH_x$ (Mg-Ti-H) thin films have electrical and optical properties that can be tuned by changing the hydrogen content. This makes them interesting for a number of applications, such as optical hydrogen sensors and semiconductor devices or as switchable coating on solar collectors and smart windows. However, Mg and Ti do not mix or form alloys under normal circumstances and samples have to be made using non-equilibrium techniques, like magnetron sputtering. This has made the structure of such samples a topic for discussion. In this work experimental and computational methods have been combined to investigate the electronic structure and atomic distribution in the meta-stable Mg-Ti-H system.

Density functional theory (DFT) was used to calculate the stability of atomistic models with nano-cluster (NC) and quasi-random (QR) distribution of Ti atoms in Mg. For Mg-rich compositions it was found that arranging Ti in nano-clusters of sizes below the X-ray detectable limit lowers the mixing enthalpy of the system, which is the cohesive energy of the elements in the model system relative to that of the standard states. In other words, nano-scale segregation of Ti makes the meta-stable Mg-Ti system less unstable than having Ti randomly distributed in the Mg matrix. Bader analysis, which is a method for dividing the valence electron density calculated by DFT into regions corresponding to the atoms in the structure, showed that a large transfer of electrons takes place from Mg to Ti and that clustering of Ti allowed some of the Ti atoms to be shielded from this extra charge. The Ti atoms in the middle of the clusters exhibited an electronic state close to that of pure Ti. It was also found that near the Fermi level the density of states (DOS) was distinctly different in the NC and QR cases. This inspired a comparison of the DFT derived DOS with the valence spectrum obtained by X-ray photoelectron spectroscopy (XPS) from a thin film sample with composition $Mg_{80}Ti_{20}$. The experimental data corresponded best with the DOS calculated for the NC model, supporting the presence of Ti nano-clusters in Mg-Ti.

XPS investigations were performed on both pure Mg and Mg-Ti thin film samples, with and without hydrogen. In the Mg-Ti-H samples a distinct new peak was discovered in the Mg *KLL* spectrum, located between the metallic and the oxide component. No traces of contaminating species were found, leaving influence from hydrogen as a likely suspect. This inspired a DFT investigation of the hydrogenation process of Mg-Ti. A single hydrogen atom was introduced on different interstitial sites in the metallic Mg-Ti crystal structure, which revealed a substantial lowering of the mixing enthalpy upon addition of H. It was found that hydrogen prefers to occupy octahedral sites with one or more Ti atoms as nearest neighbors. Contrary to prior assumptions

in the literature, the sites at the interface between Mg and Ti were thermodynamically preferred over the sites inside the Ti nano-clusters. Bader analysis showed that much of the charge lost from Mg could be attributed to the H atoms at the interface, which provided an ”electron shield” for Ti. However, *both* the sites at the interface and inside the Ti clusters were found to be very stable, with hydrogenation energies down to -115 kJ/(mol H_2), likely to keep a certain amount of H trapped in the system even after hydrogen unloading was attempted by heating in vacuum. This could explain previous reports in literature about the maximum hydrogen content obtained experimentally being lower than the stoichiometric ratio expected for Mg-Ti. The hydrogen content in the DFT model was increased gradually according to the calculated relative stabilities for H on the different sites, starting with the ones at the Mg-Ti interface, which were the most stable. It was found that with respect to the mixing enthalpy, the Mg-Ti-H system changed from meta-stable to stable for hydrogen contents above 0.07 H per metal. The results from this study helped explain why the reversibility of Mg-Ti thin films, which are initially meta-stable, can be preserved over many cycles of attempted loading and unloading of hydrogen. Returning to the initial XPS data, it was concluded that the hydride samples had lost H due to the Ar^+ sputtering that had to be employed to remove the Pd caplayer which protected the samples from oxidation. The new peak found in the Mg *KLL* spectrum of Mg-Ti-H corresponded well with the interface trapped H suggested by DFT.

In a high-energy XPS investigation using Cr Kβ radiation further details of the oxidation process of Mg-Ti were uncovered. It was found that immediately after Pd removal no traces of oxidation were found in the Mg *KLL* spectrum. Instead, a peak was found in the high kinetic energy (E_K) shoulder of the metallic Mg component. This peak disappeared and oxidation progressed rapidly in the time it took to acquire high resolution spectra. However, the high E_K peak was not observed for the hydride phase. Previously, no significant effect of introducing Ti had been found in Mg spectra obtained by XPS, which was somewhat puzzling considering the magnitude of the charge transfer predicted by DFT. With the DFT study of hydrogen in Mg-Ti as a backdrop, it was considered whether oxygen could play a similar role in shielding Ti from the charge transfer from Mg. Using DFT it was found that introducing O to octahedral sites in the crystal structure dramatically lowered the mixing enthalpy of the system. In the case of oxygen the sites inside the clusters were preferred, with the energy gain decreasing with increasing number of Ti nearest neighbors. In this context the high E_K peak in the Mg *KLL* spectrum could be explained by the interaction with Ti, which would disappear as soon as the sites at the interface between Mg and the Ti nano-clusters were filled with hydrogen. In the hydrogenated sample prior to oxygen exposure, these sites would already be filled by H, possibly explaining why the high E_K peak was not seen in the Mg *KLL* spectrum of the hydrogenated material.

Acknowledgments

As this PhD project is coming to an end I would like to express my gratitude towards the numerous people who have helped along the way. Firstly, my supervisors Ole Martin Løvvik and Spyros Diplas, both at SINTEF, who have guided me with enthusiasm and skill all the way from start to finish. I don't think I could have picked a better team for this task! In particular I am impressed by your willingness to keep up with my ambitious schedule in the last months before handing in this thesis. Secondly, I would like to thank Bernard Dam and Herman Schreuders at the Technical University Delft, for providing the thin film samples and for contributing to this project with their experience and ideas. Thanks also to John Watts and Steve Hinder at the University of Surrey, where I stayed for three months as a guest scientist.

Among the people I've occasionally tortured with details from my research I would like to mention my good friend and SINTEF colleague Annett Thøgersen, who glanced at my data with an unbiased mind and put me on the trail of the central idea of the last paper. Furthermore I would like to thank the Structure physics group at the University of Oslo, where I've served my time as a PhD student. Particular thanks to my office mates Demie Kepapsoglou and Kjetil Valset, and to Øystein Prytz, for being an even bigger science policy geek than I am.

Above all I would like to thank my partner, Klaus Magnus Johansen, to whom I probably own my (relative) sanity. We share love, ideas and aspirations, as well as a beautiful daughter and a slightly neglected dog. Without you this whole process would have been meaningless. Last but not least I would like to thank my two year old daughter Katja, although I'm not exactly sure she really did that much to help the progress of this project...

After being in and out of the University of Oslo for more than a decade, it seems our relationship has finally come to an end. It's been challenging, life altering and above all fun, but now it's time to move on. So long, UiO, hope we can stay friends!

Ingvild Thue Jensen
December 2012

Preface

Work on this thesis started in the autumn of 2007, and has been funded by the University of Oslo. In total one year was devoted to teaching obligations. The major part of the research was carried out at the Department of Physics, under the supervision of Ole Martin Løvvik and Spyros Diplas. The main focus of the work has been combining X-ray photoelectron spectroscopy (XPS) and density functional theory (DFT) to improve the understanding of the meta-stable Mg-Ti-H material system. All samples were prepared by Herman Schreuders in the group of Professor Bernard Dam at the Technical University of Delft (The Netherlands).

During the spring of 2009 three months were spent in the group of Professor John Watts at the University of Surrey (UK) and in the summer of 2010 high-energy XPS was performed at the former National Centre for Electron Spectroscopy and Surface Analysis (NCESS) at Daresbury Laboratory (UK).

Table of Contents

Acknowledgments **vii**

Preface **ix**

1 Motivation **1**
References 7

2 Methodology **11**
2.1 X-ray photoelectron spectroscopy 11
2.1.1 The binding energy and chemical shifts 13
2.1.2 Additional features in XPS spectra 17
2.1.3 Quantification 20
2.1.4 Auger parameters 21
2.1.5 Instrumentation 22
2.1.6 Experimental details 24
2.2 Density functional theory calculations 28
2.2.1 Solving the Schrödinger equation 28
2.2.2 Atoms in crystals: Bader analysis and local DOS 33
2.2.3 DOS vs. XPS valence spectra 35
2.2.4 Computational details 36
References 43

3 The Mg-Ti-H system **47**
3.1 Structure 47
3.2 Electrical and optical properties 54
3.3 XPS parameters 56
References 59

4 Overview of results **63**
References 68

Paper I:
X-ray photoelectron spectroscopy study of MgH_2 thin films grown by reactive sputtering.
I.J.T. Jensen, S. Diplas, O. M. Løvvik, J. Watts, S. Hinder, H. Schreuders, and B. Dam
Surface and interface analysis **42**, 1140-1143 (2010) **69**

Paper II :
Density functional calculations of Ti nano-clusters in the meta-stable Mg-Ti system.
I.J.T. Jensen, S. Diplas, and O. M. Løvvik
Physical review B **82**, 174121 (2010) **75**

Paper III:
Combined XPS and first principle study of meta-stable Mg-Ti thin films.
I.J.T. Jensen, O. M. Løvvik, H. Schreuders, B. Dam and S. Diplas
Surface and interface analysis **42**, 1140-1143 (2012) **87**

Paper IV:
Hydrogen induced stabilization of meta-stable Mg-Ti.
I.J.T. Jensen, S. Diplas, and O. M. Løvvik
Applied physics letters **100**, 111902 (2012) **93**

Paper V:
X-ray photoelectron spectroscopy investigation of magnetron sputtered Mg-Ti-H thin films.
I.J.T. Jensen, A. Thøgersen, O. M. Løvvik, H. Schreuders, B. Dam, and S. Diplas
Submitted to International journal of hydrogen energy (2012) **99**

Paper VI:
High energy XPS and X-AES study of $Mg_{80}Ti_{20}$ thin films with and without hydrogen
I.J.T. Jensen, A. Thøgersen, O. M. Løvvik, B. Dam,H. Schreuders, J. Watts and S. Diplas
In preparation **113**

Chapter 1

Motivation

We live in a world that is high on energy consumption. In spite passing trends to ”*go green*” and face ”*inconvenient truths*” there is little to suggest that environmental concerns are enough to make a sufficient amount of people give up on the commodities of modern life. Rather it seems that all though ”*Life in the woods*”-fantasies [1] are frequently dusted off and thrown around their lifetime appear to have an astonishing correlation with the battery life of the latest portable Apple product. This picture becomes even more alarming when considering the vast number of people still living in poverty around the globe. Figure 1.1 a) shows a map of the world where the area of each country is scaled according to their fuel usage. Comparing this with the corresponding map scaled with population, figure 1.1 b), may serve to put things into perspective. After all, there is no reason to think that people in the developing world will not strive to achieve the same standard of living as we take for granted in the West. However, if all people on earth were to live like Norwegians, for instance, we would actually need about 2.7 planets to supply the resources [2]. Needless to say, this represents a bit of a problem. Yet amidst all this despair there is also opportunity, at least for the scientist. It is not without a certain sense of irony one observes that after decades of thorough dethroning the scientists are once more called to the rescue. First we were heroes, then we were villains and now, maybe we can be heroes again?

The threat of climate change has had a notable impact on science funding, and materials science is one of the fields that has been both willing and able to shift its focus in a big way, for political and moral reasons alike. Materials play an important role in many renewable energy systems [3, 4], from solar cells [5] and wind mills [6] to fuel cells [7] and hydrogen storage [8]. Materials are also essential in energy saving efforts, like white light emitting diodes that are far superior to other sources of illumination when it comes to both life time and efficiency [9, 10] or thermoelectric materials that utilize waste heat from sources like car exhaust pipes and industrial processes

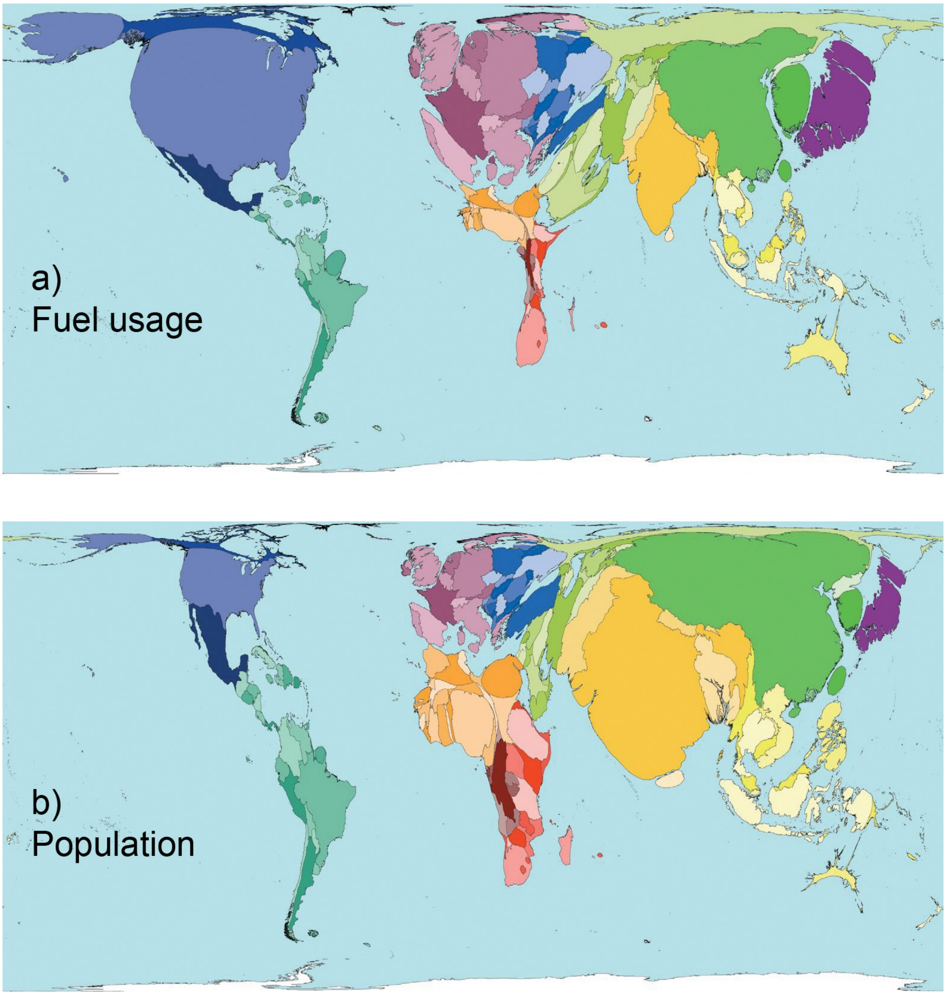
a)
Fuel usage
b)
Population

Figure 1.1: *Territory size proportional to the percentage of world fuel usage (a) and population (b). Illustration from www.worldmapper.com, based on data from 2000/2001.*

to produce electricity [11]. However, before picking out superhero costumes it is worth dwelling for a moment on the possible downside of the current ”save the world by next election”-approach to science funding. Are we in danger of shooting ourselves in the foot when we rush to accept this pre-order for innovation? Of course we *do* want to save the world, but does it not come with a sneaking suspicion that we are operating on different time scales from that of the politicians? What happens when expectations are not met? And where do we go from here if basic research is neglected? There lies a phenomenal pedagogical challenge in explaining to the general public how science really works. After all, if the scientist *was* to wear a superhero costume it should probably have a giant P on the chest. P for *patience*. Or perhaps P for *puzzle*, which is a word that actually describes the nature of science quite well. A puzzle, with its progress depending on the players' ability to add the right pieces at the right place, usually without a clear idea of what the picture is supposed to look like. Sometimes it turns out to be something completely unexpected. Sometimes it just doesn't fit. Some very few individuals, brilliant or just plain lucky, get the pleasure of being present when the pivotal piece is put down and everything starts to unravel. Those moments are few and far between, which the recent discovery of a possible Higgs particle [12, 13] illustrates in a grand way. One of the papers is even dedicated to ”*the memory of our ATLAS colleagues who did not live to see the full impact and significance of their contributions to the experiment.*”

On a more modest scale the project presented in this thesis illustrates quite well the many levels of details and the large number of small steps that are necessary in science to make up a greater picture. It originated in the context of materials for hydrogen storage, which is an important prerequisite in realizing the exhaust free car running on hydrogen produced by energy from renewable sources. More specifically, however, the project was derived from a fascinating discovery by Huiberts *et al.* in 1996 [14]; the so-called switchable mirrors. Thin films of yttrium and lanthanum are reflective and act as mirrors in the metallic state (figure 1.2 top), but upon hydrogenation they turn into transparent semi-conductors (figure 1.2 bottom). As can be seen in the picture YH_3 is quite yellow in colour, while LaH_3 is said to be more red. The following year van der Sluis *et al.* found optical switching also in Mg-La thin films, this time with a colourless transparent state [15]. Richardson *et al.* [16] followed up in 2001 with Mg-Ni films showing similar behaviour and from then on the ball has kept on rolling. Right from the start the possibility for new physics was evident. In a review by Griessen *et al.* some of the early players sum it up as follows [17]: ”*One of the most surprising results (...) was, however, that the films retained their structural integrity even though they expanded by typically 15 % during hydrogenation of the pure parent metal to the trihydride. This meant that for the first time physical properties, such as* *electrical resistivity, Hall effect, optical transmission, reflection and absorption, were amenable to experimental investigations. This led to the discovery of new phenomena in the electrical, optical and mechanical properties of these materials. Furthermore, the possibility to fine-tune their properties by alloying and the ease to change continuously their hydrogen content made them especially attractive for fundamental condensed matter physics. Soon after their discovery it became clear that switchable metal-hydride films would pose intriguing questions."* One such question emerged with the discovery of partially hydrogenated Mg_2Ni thin films exhibiting an unusual optical black state, which disappeared when the film was fully hydrogenated [18]. As it turns out this black state was caused by preferential nucleation of Mg_2NiH_4 at the substrate interface and is in reality an interference effect due to light reflecting on the interfaces on either side of Mg_2NiH_4. A similar intermediate black state was also seen in Mg, Mg-Y and Mg-La thin films [19], but this was found to be due to coexistence of metallic Mg and insulating MgH_2 particles and not an interference effect. Finally, a stable black state was reported for optically switchable Mg-Ti thin films in the fully hydrogenated state [20]. Mg-Ti films are interesting for a number of reasons, not just for its exotic optical behaviour. For starters, Mg and Ti are immiscible, which means that they can only be produced by non-equilibrium techniques such as for instance magnetron sputtering [20] or physical vapour deposition [21]. They show excellent hydrogen storage capacity and kinetics, even at room temperature [22], and what is more: they are stable over repeated cycles of hydrogen loading and unloading [23]. The latter is really quite remarkable considering the inherent meta-stability of Mg-Ti. Rather one would expect segregation into pure Mg and Ti upon cycling, as is the case for several other Mg containing alloys [24, 19, 25, 26]. In short there are a lot of questions arising from the observed properties of hydrogenated Mg-Ti thin films, especially about the microstructure of such samples, and this is where the present work aims to make a contribution. Hopefully this brief history of switchable mirrors will give a sense of the careful work that tends to lie between discovery and applications. For switchable mirrors the possible applications are many, ranging from coatings on solar collectors [20] and smart windows [27] to optical hydrogen sensors [28] and semiconductor devices such as solar cells [29]. The discovery also prompted the development of a new technique, called *hydrogenography* [30], where a compositional gradient film can be used to map the formation enthalpy of thousands of alloy compositions at once, speeding up the search for suitable new hydrogen storage materials.

In this thesis the electronic structure and atomic distribution of Mg-Ti thin films were studied both theoretically through density functional calculations (DFT) and experimentally by X-ray photoelectron spectroscopy (XPS). The methods were chosen for their relevance to the problem at hand, as well as for their generic usefulness in the face of the ongoing nanotechnology revolution. As the size of components and devices are decreased, precise understanding and control of the material properties become critical. In this work atomistic modeling and spectroscopy were combined to investigate local interactions between immiscible elements in a meta-stable system, thus contributing to the gathering of atomic scale knowledge of materials properties. In combination with atomistic modeling results from XPS, which has a lateral resolution in the order of tens of micrometers, can be used also to investigate local electronic structure. As an experimentalist turned to computation the work was always focused on the real material. How do the calculations fit with experimental observations? How can the two be combined to reach further knowledge? The two main methods, XPS and DFT, are described in chapter 2, while a more detailed background on Mg-Ti thin films is given in chapter 3. Chapter 4 sums up the work presented in the papers that follow.

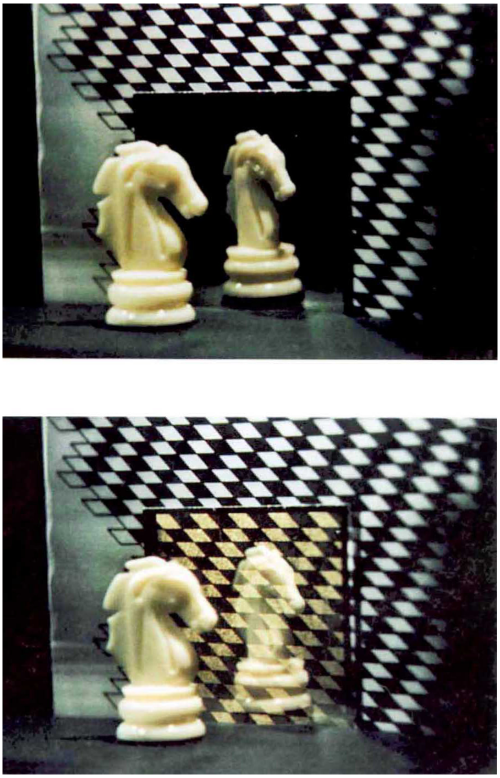

Figure 1.2: *The switchable mirror discovered by Huiberts et al. The pictures illustrate how the yttrium film is reflecting in the metallic state (top) and transparent (bottom) in the hydrogenated state. From ref. [14].*

References

[1] H. D. Thoreau. *Walden; or, Life in the Woods*. Ticknor and Fields, Boston, 1854.

[2] Monique Grooten, editor. *Living planet report*. WWF, 2012.

[3] D. Driver. Making a material difference in energy. *Energ. Policy*, 36:4302–4309, 2008.

[4] A. Rockett, Y. W. Chung, H. Blaschek, S. Butterfield, R. R. Chance, C. Ferekides, M. Robinson, S. W. Snyder, and M. Thackeray. Transformative research issues and opportunities in alternative energy generation and storage. *Curr. Opin. Solid St. M.*, 15:8–15, 2011.

[5] L. M. Peter. Towards sustainable photovoltaics: the search for new materials. *Phil. Trans. R. Soc. A*, 369:1840–1856, 2011.

[6] N. Dalili, A. Edrisy, and R. Carriveau. A review of surface engineering issues critical to wind turbine performance. *Renew. Sust. Energ. Rev.*, 13:428–438, 2009.

[7] P. P. Edwards, V. L. Kuznetsov, W. I. F. David, and N. P. Brandon. Hydrogen and fuel cells: Towards a sustainable energy future. *Energ. Policy*, 36:4356–4362, 2008.

[8] A. Züttel. Hydrogen storage methods. *Naturwissenschaften*, 91:157–172, 2004.

[9] G. Zorpette. Let there be light [gallium nitride LED]. *Spectrum, IEEE*, 39:70–74, 2002.

[10] Y. Narukawa, M. Ichikawa, D. Sanga, M. Sano, and T. Mukai. White light emitting diodes with super-high luminous efficacy. *J. Phys. D: Appl. Phys.*, 43:354001, 2010.

[11] J. Yang and T. Caillat. Thermoelectric materials for space and automotive power generation. *MRS Bulletin*, 31:224, 2006.

[12] The ATLAS Collaboration. Observation of a New Particle in the Search for the Standard Model Higgs Boson with the ATLAS Detector at the LHC. *Phys. Lett. B*, 716:1–29, 2012.

[13] The CMS Collaboration. Observation of a new boson at a mass of 125 GeV with the CMS experiment at the LHC. *Phys. Lett. B*, 716:30–61, 2012.

[14] J. N. Huiberts, R. Griessen, J. H. Rector, R. J. Wijngaarden, J. P. Dekker, D. G. de Groot, and N. J. Koeman. Yttrium and lanthanum hydride films with switchable optical properties. *Nature*, 380:231–234, 1996.

[15] P. van der Sluis, M. Ouwerkerk, and P. A. Duine. Optical switches based on magnesium lanthanide alloy hydrides. *Appl. Phys. Lett.*, 70(25):3356–3358, 1997.

[16] T. J. Richardson, J. L. Slack, R. D. Armitage, R. Kostecki, B. Farangis, and M. D. Rubin. Switchable mirrors based on nickel-magnesium films. *Appl. Phys. Lett.*, 78(20):3047–3049, 2001.

[17] R. Griessen, I. A. M. E. Giebels, and B. Dam. Optical properties of metal-hydrides: switchable mirrors. *From http://www.nat.vu.nl/ griessen/Switchable mirrors.htm*, 2004.

[18] W. Lohstroh, R. J. Westerwaal, B. Noheda, S. Enache, I. A. M. E. Giebels, B. Dam, and R. Griessen. Self-organized layered hydrogenation in black Mg_2NiH_x switchable mirrors. *Phys. Rev. Lett.*, 93(19):197404, 2004.

[19] I. A. M. E. Giebels, J. Isidorsson, and R. Griessen. Highly absorbing black Mg and rare-earth-Mg switchable mirrors. *Phys. Rev. B*, 69:205111, 2004.

[20] D. M. Borsa, A. Baldi, M. Pasturel, H. Schreuders, B. Dam, R. Griessen, P. Vermeulen, and P. H. L. Notten. Mg-Ti-H thin films for smart solar collectors. *Appl. Phys. Lett.*, 88:241910, 2006.

[21] T. Mitchell, S. Diplas, P. Tsakiropoulos, J. F. Watts, and J. A. D. Matthew. Study of alloying behaviour in metastable Mg-Ti solid solutions using Auger parameter measurements and charge-transfer calculations. *Philos. Mag. A*, 82(4):841–855, 2002.

[22] R. A. H. Niessen and P. H. L. Notten. Electrochemical hydrogen storage characteristics of thin film Mg (X, X = Sc, Ti, V, Cr) compounds. *Solid-State Lett.*, 8:A534–A538, 2005.

[23] P. Vermeulen, R. A. H. Niessen, and P. H. L. Notten. Hydrogen storage in metastable Mg_yTi_{1-y} thin films. *Electrochem. Commun*, 8:27–32, 2006.

[24] M. Gonzalez-Silveira, R. Gremaud, A. Baldi, H. Schreuders, B. Dam, and R. Griessen. Effect of H-induced microcstructural changes on pressure-optical transmission isotherms for Mg-V thin films. *Int. J. Hydrogen Energy*, 35:6959–6970, 2010.

[25] M. Di Vece, S. J. M. Zevenhuizen, and J. J. Kelly. Optical switching properties from isotherms of Gd and GdMg hydride mirrors. *Appl. Phys. Lett.*, 81:1213, 2002.

[26] D. G. Nagengast, A. T. M. van Gogh, E. S. Kooij, B. Dam, and R. Griessen. Contrast enhancement of rare-earth switchable mirrors through microscopic shutter effect. *Appl. Phys. Lett.*, 75:2050–2052, 1999.

[27] A. Anders, J. L. Slack, and T. J. Richardson. Electrochromically switched, gas-reservoir metal hydride devices with application to energy-efficient windows. *Thin Solid Films*, 517:1021–1026, 2008.

[28] M. Pasturel, M. Slaman, D. M. Borsa, H. Schreuders, B. Dam, and R. Griessen. Stabilized switchable ”black state” in Mg_2NiH_4/Ti/Pd thin films for optical hydrogen sensing. *Appl. Phys. Lett.*, 89:021913, 2006.

[29] S. Zh. Karazhanov, A. G. Ulyashin, P. Vajeeston, and P. Ravindran. Hydrides as materials for semiconductor electronics. *Philos. Mag.*, 88(16):2461–2476, 2008.

[30] R. Gremaud, C. P. Broedersz, D. M. Borsa, A. Borgschultte, P. Mauron, H. Schreuders, J. H. Rector, B. Dam, and R. Griessen. Hydrogenography: An optical combinatorial method to find new light-weight hydrogen-storage materials. *Adv. Mater.*, 19:2813–2817, 2007.

Chapter 2

Methodology

In this work two main methods were used in parallel, namely X-ray photoelectron spectroscopy (XPS) and density functional theory (DFT) calculations. The dual approach made it possible to draw inspiration from results obtained by one method into the data accumulation and interpretation of the other. This chapter gives a brief description of each method, as well as an overview of specific details relevant for the research presented in the appended papers. Ref. [1] and [2] have been used as a basis for the general XPS and DFT descriptions, supplemented by other resources as stated in the text.

2.1 X-ray photoelectron spectroscopy

X-ray Photoelectron Spectroscopy (XPS) is a technique for studying composition, chemical state and electronic structure of the outermost few nanometers of a material. The principle is ”X-rays in - electrons out”, see figure 2.1. The material is irradiated with X-rays and from measuring the kinetic energy (E_{k}) of the emitted photoelectrons their binding energy (E_{b}) relative to the Fermi level can be calculated. All elements except H and He can be detected directly. The technique is very surface sensitive, normally with an analysis depth of about 5-10 nm. XPS measurements are performed in ultra high vacuum (UHV), which protects the sample surface from contamination during measurement and allows easy detection of emitted electrons.

Figure 2.2 shows an example of a survey spectrum for a Mg-Ti sample. Sharp peaks are formed at the binding energies of emitted photoelectrons and the combination of peaks serves as a finger print of the elements present in the sample. Each peak is named after their orbital of origin, e.g.,

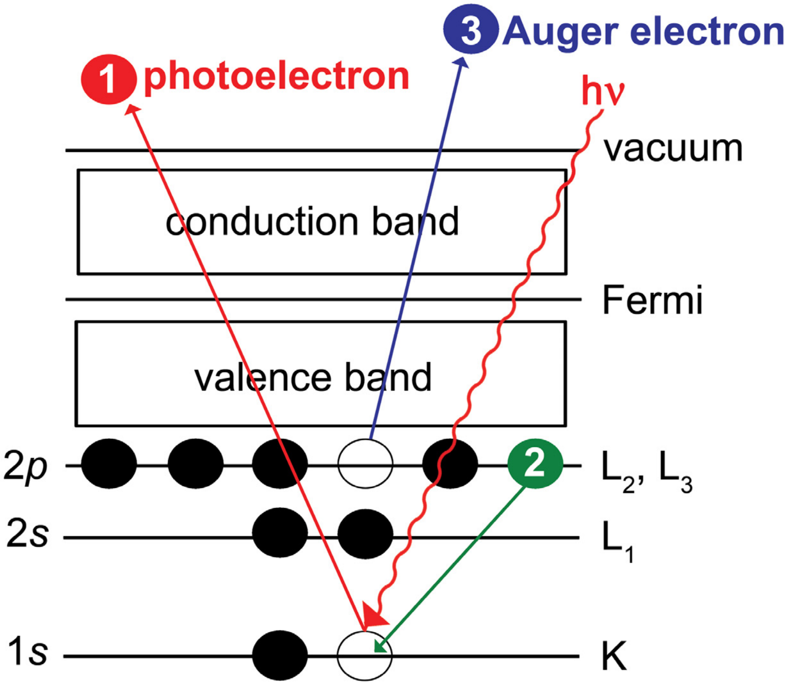
① photoelectron
③ Auger electron
hν
vacuum
conduction band
Fermi
valence band
2p
2s
1s
②
L_2, L_3
L_1
K

Figure 2.1: *The principle of XPS is based on the photoelectron process, where X-rays with energy* $h\nu$ *knock out photoelectrons (1) with binding energy* $\leq h\nu$. *Also detected are the Auger electrons (3), which are emitted due to the energy being released when the initial photoelectron hole is filled (2).*

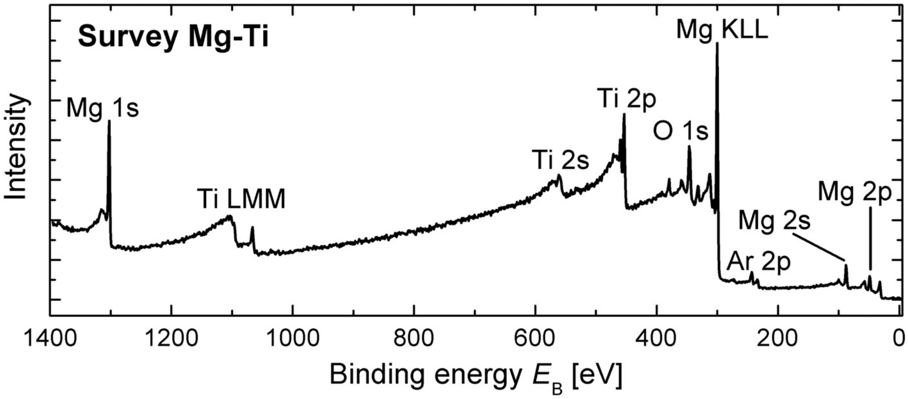

Figure 2.2: *An example of XPS survey spectrum for a Mg-Ti sample.*

Mg 2p, Mg 2s, Ti 2p in figure 2.2. While the position of the peaks can be used to identify the elements, the relative heights or areas of the peaks can be used to obtain quantitative information about the composition, with an accuracy down to 0.1 at.% [3]. In addition to the photoemission peaks an XPS spectrum may also contain additional features called Auger peaks. When an electron is emitted as a photoelectron the atom is left in an excited state with a hole in the emitting orbital. When this hole is filled by a second electron from a higher orbital the energy difference between the orbitals must be released and can result in emittance of a third electron from even further out; the so-called Auger-electron. While the E_k of the photoelectron will depend on the energy of the incoming X-ray beam, the Auger-process only depends on internal transitions and will be detected at the same E_k regardless of the X-ray source at hand (given the energy is high enough to create the initial photoelectron). The Auger peaks are named after the orbitals of the three electrons involved in the process, e.g., Mg *KLL* and Ti *LMM* in figure 2.2.

2.1.1 The binding energy and chemical shifts

The binding energy (E_b), which is the energy needed to move an electron from its orbital to the Fermi level, can be expressed as follows:

$$\begin{aligned} E_\mathrm{b} &= h\nu - E_\mathrm{k} - \phi_\mathrm{sample} - (\phi_\mathrm{spec} - \phi_\mathrm{sample}) \\ &= h\nu - E_\mathrm{k} - \phi_\mathrm{spec}, \end{aligned} \tag{2.1}$$

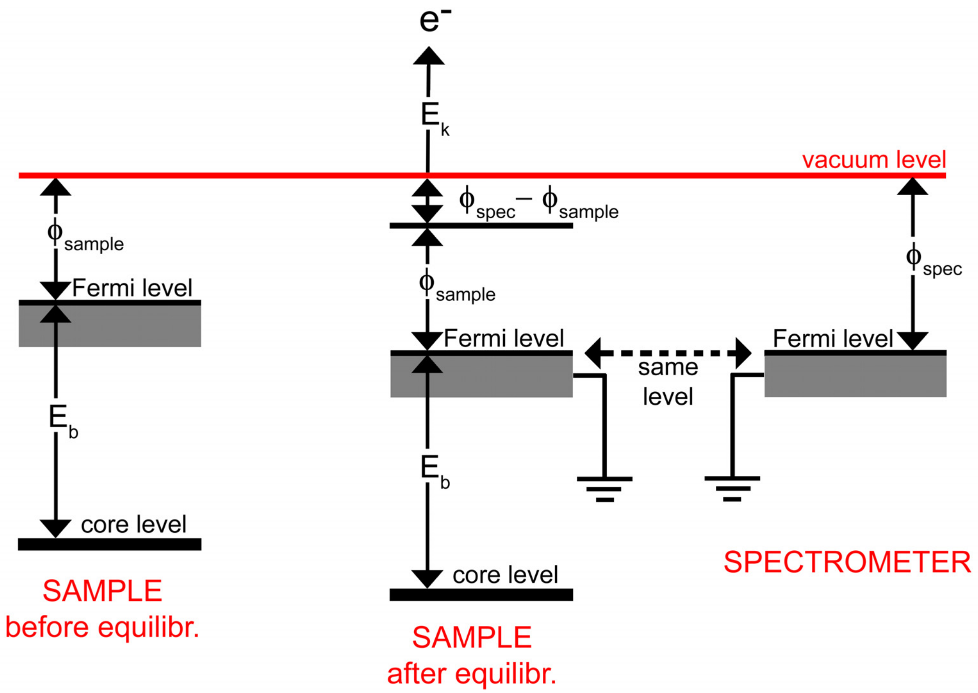
e⁻
Ek
vacuum level
ϕsample
ϕspec − ϕsample
ϕsample
ϕspec
Fermi level
Fermi level
Fermi level
same
level
Eb
Eb
core level
core level
SAMPLE
before equilibr.
SAMPLE
after equilibr.
SPECTROMETER

Figure 2.3: *Binding energy (E_b) referencing in the XPS instrument, in the case of conducting samples. The figure illustrates how it is the work function of the spectrometer (ϕ_{spec}) which affects the measured kinetic energy (E_k) of the photoelectron (e^-), rather than the work function of the sample (ϕ_{sample}) itself. Given that the sample is conducting and in electrical contact the Fermi levels of the sample and the instrument line up. The work functions, however, differ. The sample is shown before and after equilibration of the Fermi levels.*

where $h\nu$ is the energy of the X-ray beam and ϕ_{spec} and ϕ_{sample} are the work functions of the instrument and the sample, see figure 2.3. A work function is the energy required to remove the electron from the sample surface, i.e., from the Fermi level to the vacuum level. So how does the binding energy relate to the orbital energy ε as we know it from quantum mechanics? According to Koopman's theorem it is very simple, in a "frozen orbital" approximation the binding energy is just the orbital energy one would obtain from Hartree-Fock calculations. Fortunately for us, however, the orbitals in an atom are not really frozen. If they were it would make XPS much less interesting, as explained below. In reality the core hole produced in the photoemission process creates a change in the potential of the atom which then causes the remaining electrons to readjust to minimize the energy. This is called *relaxation* (R) and can be categorized into intra- and extra-atomic contributions. The intra-atomic contribution arises from the rearrangements of the electrons within the atom, i.e., the outer electrons will be more tightly bound. The extra-atomic response comes from the neighbouring atoms, whose electrons might also feel the change in potential and take part in the screening, by charge transfer or polarization. Thus we get the expression:

$$E_{\text{b}} = -\varepsilon - R \tag{2.2}$$

The effect of the R part is to lower the E_{b} with respect to ε, almost like the photoelectrons are given a small extra push on the way out. The relaxation will be different in different chemical states and environments, giving rise to *chemical shifts* in the binding energies of an element. It is the detection of these shifts that makes the XPS technique so incredibly sensitive to changes in chemical environment. The chemical shift reflects changes in electronic structure and bonding and with XPS one can pick up on these changes, for instance oxidation states, alloy formations etc. Figure 2.4 shows the chemical shift between MgO and $Mg(OH)_2$ in the O 1s peak. However, as the shifts may sometimes be small, reliable energy referencing becomes an issue. Measurements from different instruments and setups may not always be safely compared and even in a hypothetically perfect instrument the energy scale may be obscured due to sample charging. This can be tackled by using known features for calibration, e.g., the 1s peak from adventitious carbon. Another way to reduce the uncertainty related to referencing is to use Auger-parameters (APs), which will be discussed in a separate section.

An important thing to note is that the relaxation of the system upon photoemission implies that XPS does not give direct information of the atom in its *initial-state*, the ground state. Instead, what we measure is in fact the *final-state*, with one electron missing. However, the final-state is influenced by the initial-state, making XPS a valuable tool for sample analysis.

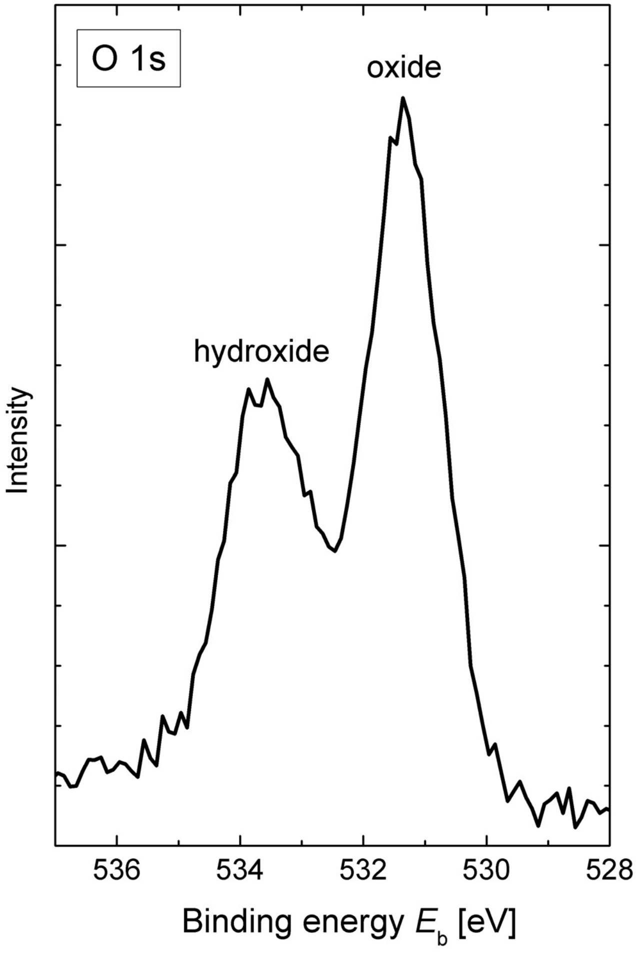

Figure 2.4: *An example of XPS high resolution spectrum, illustrating the chemical shift in O 1s between MgO and* $Mg(OH)_2$ *in an Mg-Ti sample.*

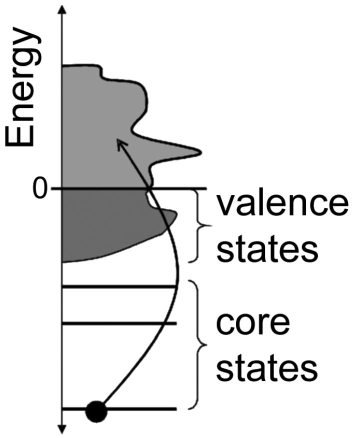

Figure 2.5: *Schematic illustration of valence and core states in a metal.*
Figure from http://users.auth.gr/users/0/6/050360/public_html/nexafs_in.htm.

2.1.2 Additional features in XPS spectra

In this section some of the additional features that may be present in an XPS spectrum are described, mainly based on Ref. [4]:

The valence electrons have low binding energy, in the region from 0 to about 20 eV. This part of the XPS spectrum appears visually different from the core level peaks as they consist of many closely spaced levels, as illustrated in figure 2.5. Also, the emission cross-sections for valence electrons are much lower than for core electrons and when put together this leaves a lot to be desired in terms of resolution.[1] Nevertheless, valence spectra may still play an active role in sample analysis, for instance for polymers [5]. The close relation between the density of states and the XPS valence spectrum also makes such data suited for comparison with theoretical calculations, for instance from DFT [6]. Figure 2.6 shows an example of an XPS valence spectrum.

Spin-orbit coupling often gives rise to energy splitting of photoelectron peaks in XPS spectra. The interaction between the electron spins s, which has two states (up or down) and the orbital angular momentum l, causes a split into different energy states. The Ti 2p in figure 2.7 is an example of a split photoelectron peak. The intensity ratio of the peaks can be calculated quite easily from the total angular momenta (j): $I \propto \frac{(2j_{+}+1)}{(2j_{-}+1)}$.

---

[1] If valence spectra are the *primary* interest of an investigation ultra-violet photoelectron spectroscopy (UPS) would be a better choice of technique, offering better energy resolution than XPS.

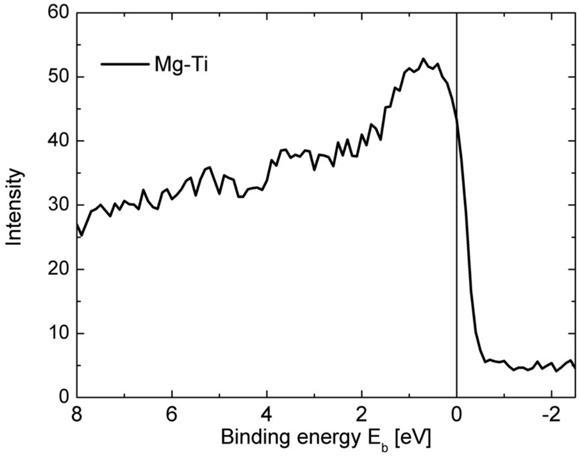

Figure 2.6: *XPS valence spectrum from a Mg-Ti sample with 20 at.% Ti.*

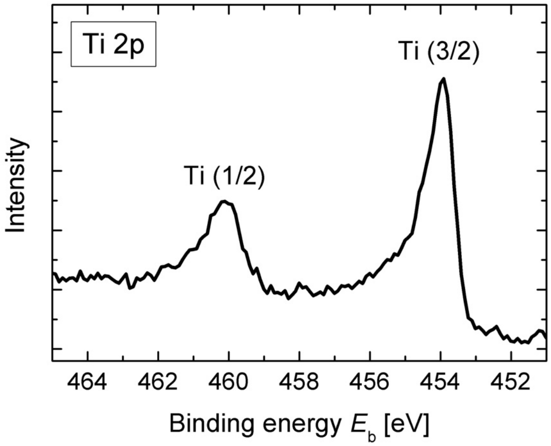

Figure 2.7: *The Ti 2p spectrum from a Mg-Ti sample with 20 at.% Ti, showing splitting of the photoelectron peak and asymmetric peak shape.*

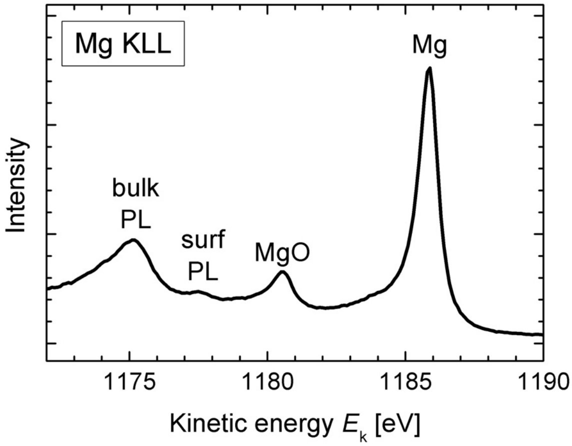

Figure 2.8: *The Mg KLL spectrum from a Mg-Ti sample with 20 at.% Ti, showing the presence of surface and bulk plasmon energy loss, surf and bulk PL, respectively.*

Shake-up satellites can sometimes be seen on the high E_b side of photoelectron peaks as a result of the relaxation process of the valence electrons. As the valence electrons adjusts to the loss of a core electron, excitation to a higher unfilled level may occur. For certain transition metals with unpaired electrons in $3d$ shells or $4f$ shells in rare earth compounds, very strong satellites are found. Satellites are final state features that can be useful in chemical state investigations, as the same element may display different features in different environments. In the case of metals shake-up-type events usually give rise to a continuous tail rather than distinct features on the high E_b side. This is due to the many one-electron states available just above the Fermi level and means that metallic peaks must be fitted with a certain asymmetry. The Ti 2p peaks in figure 2.7 are examples of asymmetric metallic peaks.

Plasmon loss features arise from collective oscillations of the conduction electrons. The frequency of oscillation (ω_p) is characteristic of the material. When an electron gives away energy corresponding to this frequency a series of evenly spaced plasmon loss peaks can be seen on the higher E_b side of the photoelectron peak. In the free electron model the energy can be expressed as [7]:

$$E_p = \hbar\omega_p = \hbar\sqrt{\frac{Ne^2}{Vm_0\epsilon_0}}, \tag{2.3}$$

where N is the number of valence electrons in the unit cell, e is the electron charge, V is the volume of the unit cell, m_0 is the free electron mass and ϵ_0 is the permittivity of free space. Thus changes in plasmon energy reflect changes in the material, like variations in conductivity or valence electron density. Plasmon loss peaks can be separated into two distinct types depending on their origin, either from *bulk* or *surface* plasmons, as shown in figure 2.8. The plasmon energies from XPS can be compared to plasmon energies from other techniques, for instance electron energy loss (EELS) data obtained by transmission electron microscopy (TEM).

In addition to the features mentioned above XPS spectra can be obscured by external structure arising from the use of non-monochromated X-rays. These are called *X-ray satellites* and *ghosts* and are low intensity peaks in the XPS spectrum which arise from less probable transitions in the X-ray producing anode material and impurity elements within the X-ray source, respectively.

2.1.3 Quantification

To obtain quantitative information from XPS spectra the peak intensities or areas must be transformed into atomic concentrations. Several factors affect the peak intensities/areas, both sample- and spectrometer-specific, as explained in Ref. [1]: Sample-specific factors are related to

- the cross section for photoemission, which depends on the element, the orbital of ejection and the excitation energy
- the escape depth or attenuation length of the emitted electron, which depends on the E_k of the electron and the nature of the sample

The latter point is due to the fact that photoelectrons have a limited mean free path in a specific sample. An electron with higher E_k will be able to escape from deeper in the sample than an electron with lower E_k, thus effectively the analysis volume will differ for different peaks. The spectrometer-specific factors are related to

- the photon flux J
- the transmission function of the spectrometer, which is the proportion of the electrons transmitted through the spectrometer as a function of their kinetic energy
- the efficiency of the detector, i.e., the proportion of the electrons striking the detector which are detected

- the different effect of stray magnetic fields on high- and low-energy electrons

A simplified form of the intensity (I) is given by:

$$I = J\rho\sigma K\lambda, \tag{2.4}$$

where J is the X-ray photon flux, ρ is the concentration of the element, σ is the emission cross section, K is a term that covers the instrumental factors and λ is the electron attenuation length. The last three terms are usually incorporated into a parameter F called the relative sensitivity factor (RSF). For constant J the atomic percentage C of element i in a sample can be expressed as a fraction of the total sum of all normalized intensities:

$$C_i = \left(\frac{\frac{I_i}{F_i}}{\sum_j \frac{I_j}{F_j}} \right) \cdot 100 \text{ [at.\%]} \tag{2.5}$$

The RSF of a certain orbital in a certain element irradiated by a certain source can be either theoretically or empirically determined. The RSF values based on cross sections theoretically calculated by Scofield[8] are widely used, as are spectrometer specific values provided by the instrument manufacturers. In the above expressions a homogenous sample is assumed. Although this is seldom the case, the approach will still be useful in comparison of similar samples.

2.1.4 Auger parameters

As mentioned earlier chemical shifts are often small and thus vulnerable to energy referencing errors. A way to get around this problem is to employ the concept of the Auger parameter (AP) [9]. The final-state AP α is defined as:

$$\alpha = E_{\mathrm{b}}(\text{photoelectron}) + E_{\mathrm{k}}(\text{Auger electron}) \tag{2.6}$$

α is essentially the distance between a photoelectron peak and a related Auger-peak and thus a relative quantity not affected by energy referencing problems. By using AP's rather than individual peak positions one can obtain reliable comparisons of different samples, regardless of the instruments or setups used. It can be shown that the change in AP from the element in its pure state to an element in a compound is given by [10]:

$$\Delta\alpha = 2\Delta R \tag{2.7}$$

Thus changes in AP can give information about the final-state relaxation energy R. This was developed even further, into a detailed expression which established the AP as a probe of charge distribution [10, 11]:

$$\Delta\alpha = \Delta\left(\sum_i q_i \left[\frac{\mathrm{d}k_i}{\mathrm{d}N} + \left(k_i - 2\frac{\mathrm{d}k_i}{\mathrm{d}N}\right)\frac{\mathrm{d}q_i}{\mathrm{d}N}\right]\right) + \Delta\left(\frac{\mathrm{d}U}{\mathrm{d}N}\right) \tag{2.8}$$

where q is the valence charge, k is the change in the core potential when a valence electron is removed, N is the occupation number of the core orbitals and U is the potential due to the surroundings. The sum is taken over all valence orbitals. The first term represents the relaxation contribution from shrinkage of the occupied valence orbitals when a core hole is produced. The second term represents the contribution from transfer of screening charge from the surroundings to the core ionized atom. The last term represents the effect of polarization of the surroundings by the core hole. In conductors the last term is zero, and when comparing two metals the second term will cancel out owing to perfect screening in metallic state. Thus for metals $\Delta\alpha$ can be used to calculate charge transfer, e.g., between elements in an alloy. For non-conducting samples this becomes more complicated.

2.1.5 Instrumentation

The XPS technique is very surface sensitive, as the photoelectrons have a limited mean free path. Normally the analysis depth is 5-10 nm, and the depth resolution can be increased even further by angle-resolved XPS. Depth profiles over several hundreds of nm can be obtained by controlled Ar^+ sputtering. To protect the surface from contamination during measurements all commercial instruments operate in ultra-high vacuum (UHV), i.e., in the range 10^{-8} to 10^{-10} mbar [1]. Still, this vacuum is not perfect, and as will be shown in the present work, sensitive samples might still be oxidized inside the analysis chamber during measurement. The vacuum also prevents the photoelectrons from being scattered by gas molecules on their way from the sample to detection. Samples have to be vacuum compatible. Samples that are not sufficiently conducting to transport new electrons to the analysis area may build up electrostatic charge that will move the peaks to higher E_k. This can be remedied by flooding the sample with low energy electrons to obtain charge neutralization.

Essentially, in all XPS measurements there is a tradeoff between the energy resolution, which can be adjusted as explained below, and the acquisition time. Only a given number of photoelectrons are emitted from the sample and increasing the energy resolution will invariably decrease the signal-to-noise ratio. Modern instruments are designed to make the most out of every photoelectron, containing a myriad of specially designed optimizing features. Principally, however, the three most important parts of an XPS instrument are still the X-ray source, the analyzer and the detector. A brief, non-comprehensive description of these parts are given below, mainly based on Ref. [1]:

In XPS X-rays are produced when high energy electrons, usually from an electrically heated tungsten filament, hit a metal anode. The most common anode materials are aluminium (Al $K\alpha$ line, $h\nu = 1486.6$ eV) and magnesium (Mg $K\alpha$ line, $h\nu = 1253.6$ eV). Most of the work presented in this thesis was performed on an Kratos AXIS Ultra DLD instrument, which has the choice of monochromated aluminium or silver (Ag $L\alpha$ line, $h\nu = 2984.4$ eV) sources as well as a non-chromated Al and Mg twin anode. In paper VI high-energy radiation from chromium (Cr $K\beta$ line, $h\nu = 5946.7$ eV) was used. Important aspects in choosing the X-ray source, apart from the energy being high enough to excite electrons from the elements and orbitals of interest, is the X-ray line width. Using monochromated X-rays the full width at half maximum (FWHM) can be greatly reduced, e.g., from 0.9 eV to about 0.25 eV for Al $K\alpha$. Monochromation is achieved using diffraction in a crystal lattice, usually a quartz crystal. As well as improving spectral resolution the monochromation also cleans up the spectrum in the sense that certain secondary features, like X-ray satellite peaks and ghosts, are avoided.

The analyzer generally used for XPS is called a hemispherical sector analyzer (HSA) and consists of two concentric hemispherical electrodes with a potential difference across. When the electrons enter the gap between the two hemispheres their paths are affected by the potential difference and only electrons with the right energy will be able to make it through to the other side, as illustrated in figure 2.9. To record a full spectrum the potential of the analyzer is varied in steps. The step size, together with the pass energy of the analyzer, is set by the user in order to control the energy resolution of the spectrum. In a real spectrometer numerous lenses exist in between the sample and the analyzer, to collect and focus the emitted electrons. The kinetic energy of the electrons also needs to be retarded before entering the analyzer, in order to achieve sufficiently high energy resolution.

When it comes to detectors, there are two commonly used systems [12]: channel electron multipliers (channeltrons) and channel plates, which serve to multiply the electrons that are to be counted. The channeltron is a metal-coated glass tube with a $\sim 2-4$ kV potential difference in the length direction. When the photoelectron hits the walls of the tube secondary electrons are emitted, which will again hit the walls sequentially to produce even more electrons. For each

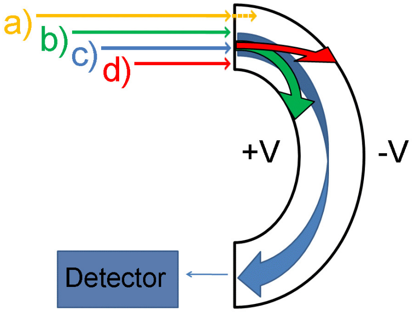

Figure 2.9: *Schematic representation of hemispherical sector analyzer, illustrating how only electrons with the "correct" energy are able to reach the detector. a) represents neutral particles, b)represents low energy electrons, c) represents the "correct" energy electrons and d) represents the high energy electrons. Figure adapted from http://en.wikipedia.org/wiki/Low-energy_ion_scattering.*

photoelectron entering the channeltron about 10^8 electrons are produced and picked up by the end collector. Usually an array of channeltrons is used to increase the sensitivity. Channel plates are discs having an array of small holes, where each hole essentially works as a channeltron. Channel plates can be used to detect signal in two dimensions as well.

2.1.6 Experimental details

The samples investigated in this work were made by magnetron sputtering by H. Schreuders in the group of Prof. B. Dam at the Technical University in Delft, the Netherlands. $Mg_{80}Ti_{20}$ (Mg-Ti) and pure Mg films covered with a thin protective layer of Pd were deposited in a UHV system (base pressure = 10^{-6} Pa) by DC/RF magnetron sputtering. The former was made by co-sputtering of Mg (99.95%) and Ti (99.999%) targets in 0.3 Pa of Ar, on single-crystal Si(100) substrates. The substrate was kept at room temperature. In order to obtain homogenous films the substrate was continuously rotated during sputtering. The typical deposition rate was 2.2 Å/s at 150 Watt RF for Mg and 0.42 Å/s at 131 Watt DC for Ti. A Pd (99.98%) caplayer was sputtered with a rate of 0.58 Å/s at 25 Watt DC to prevent oxidation. The pure Mg films were deposited at similar conditions. The investigated samples were produced in two batches. In batch 1 the investigated film was 100 nm thick with a 5 nm Pd layer on top and in batch 2 the film was 200 nm thick with a 1.5 nm Pd layer. The first batch was hydrogenated *ex situ* in 10 bar H_2 at 80 °C.

The second batch was hydrogenated at room temperature *in situ* directly after sputtering with 100 % hydrogen at 1 bar for about a day. The thin Pd layer of 1.5 nm is just enough to load the sample, while unloading is prevented. For paper I, MgH_2 thin films were deposited by RF magnetron reactive sputtering of an Mg (99.95 %) target in a mixture of Ar and H_2. The sputter pressure was 0.5 Pa at a flow rate of 15 sccm Ar and 30 sccm H_2. The typical deposition rate was 0.9 Å/s at 80 W RF. The sample thickness was approximately 50 nm.

For paper I reactively sputtered MgH_2 samples were investigated by XPS using a Thermo Scientific Theta Probe with a monochromatic Al Kα source (hν = 1486.6 eV) operated at 15 kV and 6.7 mA. High-resolution spectra were acquired with pass energy 20 eV and step size 0.1 eV/s. Measurements at different sample depths were obtained by sputtering an area of 3 x 3 mm with a 2 kV Ar^+ ion beam delivering 1 μA of current.

For paper V, which contains the main part of the XPS work, the Mg and Mg-Ti samples with and without H were investigated by XPS using a KRATOS AXIS ULTRA^{DLD} instrument with monochromatic Al Kα radiation ($h\nu = 1486.6$ eV) operated at 15 kV and 15 mA. The Pd layer was removed by sputtering an area typically about 2 mm x 2 mm with an Ar^+ ion beam of 0.5 or 2 kV delivering 100 μA of current. To minimize cratering effects and avoid detection of Pd the measurements were done using a "small spot" aperture with a diameter of 110 μm. High resolution spectra were acquired with pass energy 20 eV and dwell time 200 ms. Two different series of experiments were performed. In the *over-night exposure* (ON) experiments the measured sample was left in position in the XPS analysis chamber for about 24 hrs before the same measurement was repeated. Magnesium is highly reactive to oxygen, which means that it will oxidize even in UHV. Thus the results from the ON experiment show the changes in spectra upon gentle oxidation, comprising data from pure Mg, pure Mg with H and Mg-Ti with H. A comparative *depth profile* (DP) experiment was performed for Mg-Ti with and without H. For each sample measurements where done at intervals of 5 minutes Ar^+ sputtering at 0.5 kV, starting with 5 minutes and ending with 30 minutes total sputtering time. The sputtering time was not converted to sample depth as the aspect ratio of the craters were too small to be measured by available methods, e.g., stylus profilometry, atomic force microscopy. Details of the measurements are listed in table 2.1. The Mg 2p, Mg 1s, Ti 2p and O 1s photoelectron peaks and the Mg *KLL* Auger peak were acquired.

In paper VI high-energy XPS was performed at the former National Centre for Electron Spectroscopy and Surface Analysis (NCESS) at Daresbury Laboratory using a Scienta ESCA-300 spectrometer with a dual monochromatic X-ray source [13]. The high-energy Cr Kβ (5946.7 eV) source was used in order to probe the deeper core levels of Ti. The increased energy compared to Al Kα also allows for deeper analysis of the sample than what is the case for conventional Al Kα XPS. In order to remove the protective Pd layer the samples were Ar^{+} sputtered prior to measurement at 4 kV and 150 μA. The metallic sample was sputtered for 55 minutes, while the hydrogenated sample was measured twice, after 45 and 65 minutes sputtering. Survey spectra and rapid spectra of the Mg *KLL* peak were recorded at a pass energy of 500 eV and a step size of 2 eVs^{-1}, while high resolution spectra were recorded at a pass energy 300 eV and a step size 0.1 eVs^{-1}. The duration of a rapid Mg *KLL* scan was about a minute, while a corresponding high resolution spectrum of the Mg *KLL* peak would take 105 minutes to acquire. To monitor the development of surface oxidation during measurement the high resolution data were taken in several subsequent scans, which were added in the end to provide adequate signal-to-noise ratio.

In all cases data processing was done using CasaXPS [14]. All spectra were fitted with a standard Shirley background [15] and in quantifications Scofield cross-sections were used for the relative sensitivity factors [8].

Table 2.1: *List of measurements in paper V, labeled by measurement numbers (M no.) The experiments are categorized as initial, depth profile (DP) or over-night exposure (ON). The compositions refer to pure Mg (Mg) and* $Mg_{80}Ti_{20}$ *(Mg-Ti) with and without H. Information about sample batch number and* Ar^+ *sputtering parameters are also given. See text for details.*

M no.	**Experiment**	**Composition**	**Batch no.**	**Ar^+ sputtering**	
				volt. [kV]	**time [min]**
M1	initial	Mg	1	2	3.5
M2	initial	Mg-Ti	1	2	3.5
M3	DP	Mg-Ti	2	0.5	5
M4	DP	Mg-Ti	2	0.5	10
M5	DP	Mg-Ti	2	0.5	15
M6	DP	Mg-Ti	2	0.5	20
M7	DP	Mg-Ti	2	0.5	25
M8	DP	Mg-Ti	2	0.5	30
M9	DP	Mg-Ti-H	2	0.5	5
M10	DP	Mg-Ti-H	2	0.5	10
M11	DP	Mg-Ti-H	2	0.5	15
M12	DP	Mg-Ti-H	2	0.5	20
M13	DP	Mg-Ti-H	2	0.5	25
M14	DP	Mg-Ti-H	2	0.5	30
M15	ON	Mg-Ti-H	1	2	10
M16	ON	Mg-Ti-H	1	2	*
M17	ON	Mg-Ti-H	1	2	**
M18	ON	Mg-H	1	2	5
M19	ON	Mg-H	1	2	**
M20	ON	Mg	2	2	40
M21	ON	Mg	2	2	**

* Same as above, measured $\sim$ 2 hrs later.

** Same as above, next day measurement.

2.2 Density functional theory calculations

'The general theory of quantum mechanics is now almost complete. The underlying physical laws necessary for the mathematical theory of a large part of physics and the whole of chemistry are thus completely known, and the difficulty is only that the exact application of these laws leads to equations much too complicated to be soluble.'

This quote by P.A.M. Dirac in 1929 points to the very challenge of making theoretical predictions in modern materials science. In *principle* we can calculate all we need from the Shrödinger equation, but as soon as we move from the simplest cases, like the hydrogen molecule, into materials consisting of atoms in the order of 10^{23} per cm^3, the computational cost exceeds all earthly limits. In the following sections one of the theories developed to circumvent this obstacle is referred, namely density functional theory (DFT). The general DFT section is based on ref. [2].

2.2.1 Solving the Schrödinger equation

A simple form of the time-independent Schrödinger equation is

$$\hat{H}\Psi = E\Psi, \tag{2.9}$$

where $\hat{H}$ is the *Hamilton operator* (Hamiltonian) which acts on a wave function Ψ called the *eigenstate* to produce an *eigenvalue*, the energy E, which is the real, observable quantity of the system. In the case of materials science the hamiltonian we are interested in must describe the interactions of multiple electrons with multiple ions and themselves. If we consider the ions to be stationary from the electrons point of view (the Born-Oppenheimer approximation), it can be expressed as

$$H = -\frac{\hbar^2}{2m}\sum_{i=1}^{N}\nabla_i^2 + \sum_{i=1}^{N}\sum_{I=1}^{m} V_{el-ion}(\mathbf{r}_i, \mathbf{R}_I) + \frac{1}{2}\sum_{i}^{N}\sum_{j\neq i}^{m}\frac{e^2}{\mid \mathbf{r}_i - \mathbf{r}_j \mid} \tag{2.10}$$

The first term is the sum of the kinetic energy of all the N electrons. The second term is the sum of each of the N electrons' interaction with each of the m ions, the external potential. The last term is the sum of all the electrons' interaction with each of the other electrons, the interaction potential.

In a system of N electrons in three dimensions the wave function is a function of $3N$ variables, $\Psi(\mathbf{r}_1, ..., \mathbf{r}_N)$, which means that solving the Schrödinger equation becomes solving a differential equation in $3N$ unknowns. Clearly this has to be simplified to be of any practical use. Firstly, the wave function can be approximated to consist of individual one electron wave functions, i.e., $\Psi = \psi_1(\mathbf{r})\psi_2(\mathbf{r}), ..., \psi_N(\mathbf{r})$. This is called the Hartree product. However, as all the electrons interact with each other, solving these one electron equations can not be done individually, i.e., it is a many-body problem. After all, the interactions of electrons with each other are what makes up a material and ignoring this would make our calculations pretty useless. To simplify further we could take a closer look at the physical meaning of the wave function Ψ_i. In spite being in itself a rather abstract concept, its complex conjugate leads to a quantity far more tangible: The probability of finding the N electrons at particular points in space. In terms of one electron wave functions we can then define the *electron density* $n(\mathbf{r})$:

$$n(\mathbf{r}) = 2\sum_i \psi_i^*(\mathbf{r})\psi_i(\mathbf{r}) \tag{2.11}$$

The factor 2 comes from the Pauli exclusion principle which allows two electrons to be at the same place, provided they do not have the same spin. So where is the simplification in this? Well, if we make use of $n(\mathbf{r})$ in the last term of eq. 2.10, we only have to calculate the interaction between each single electron and the total electron density, rather than all the remaining electrons separately. The interaction potential can now be expressed by the *Hartree potential*, V_H:

$$V_H = e^2 \int \frac{n(\mathbf{r}')}{|\mathbf{r} - \mathbf{r}'|} d^3r' \tag{2.12}$$

The obvious flaw in this approximation is the single electron's interaction with itself, through the total electron density.

Density functional theory (DFT) is an approach to solving the Schrödinger equation which emerged from two mathematical theorems proved by Hohenberg and Kohn in the 1960s. The first one states that "*the ground-state energy from the Schrödinger's equation is a unique functional*[2] *of the electron density.*" In other words; the ground-state energy, the wave function, and all other properties are uniquely determined by the ground-state electron density. This means that potentially the Schrödinger equation can be solved for the electron density of 3 spatial variables, instead of the wave function of $3N$ variables. That is, if only we knew the functional $E[n(\mathbf{r})]$. The second Hohenberg-Kohn theorem reveals the contours of a practical method:"*The electron*

---

[2] A *functional* is a function of a function.

density that minimizes the energy of the overall functional is the true electron density corresponding to the full solution of the Schrödinger equation." Again, if only we knew the functional $E[n(\mathbf{r})]$, we could vary the electron density until the minimum energy was reached.

An important consequence of the Hohenberg-Kohn theorems is that in solving the Schrödinger equation we no longer have to concern us with what is the "true" wave function or interaction potential, instead we can look for a simpler way to produce the same $n(\mathbf{r})$. This lead to the Kohn-Sham (KS) equations, which map the properties of a many-body system onto a system of non-interacting electrons under a different potential. In other words, the electron density is the same, while the potential is whatever potential that will produce this electron density for non-interacting electrons, *an effective potential.* Thus the many-body problem is reduced to a set of equations involving only one electron each:

$$\left[-\frac{\hbar^2}{2m}\nabla^2 + V(\mathbf{r}) + V_H(\mathbf{r}) + V_{XC}(\mathbf{r})\right]\psi_i(\mathbf{r}) = \varepsilon_i\psi_i(\mathbf{r}), \tag{2.13}$$

where the first two terms are the same as in eq. 2.10; the kinetic energy of the electrons and their interactions with the atomic nuclei. V_H is the Hartree potential as before, while V_{XC} contains all the tricky bits that are left to sort out, like electron exchange and correlation and corrections for the self-interaction in V_H. It is this exchange-correlation functional that poses the challenge in KS-DFT, as will be discussed below.

First we will just assume adequate approximations for V_{XC} to exist and move on to the principle of DFT based algorithms, as illustrated in figure 2.10. Our objective is to find the electron density $n(\mathbf{r})$ that defines the ground-state energy of a system, by solving the KS-equations. To do this, however, we need to use $n(\mathbf{r})$ in the Hartree potential, i.e., before we can start to find the true $n(\mathbf{r})$ we have to come up with an initial trial $n(\mathbf{r})$ from educated guessing. This is step 1. Step 2 is to solve the KS-equations to find the single-particle wave functions $\psi_i(\mathbf{r})$ and step 3 is to use these wave functions to calculate the electron density from eq. 2.11. Finally, if the output density equals the input density the job is done. If not the initial density has to be updated in some way before the process is repeated. This has to continue until the energy reaches an acceptable convergence.

In order to utilize the results of Hohenberger, Kohn, and Sham, we need to define the exchange-correlation potential V_{XC}, which is a functional derivative of the exchange-correlation energy $E_{XC}[n(\mathbf{r})]$:

$$V_{XC} = \frac{\delta E_{XC}(\mathbf{r})}{\delta n(\mathbf{r})} \tag{2.14}$$

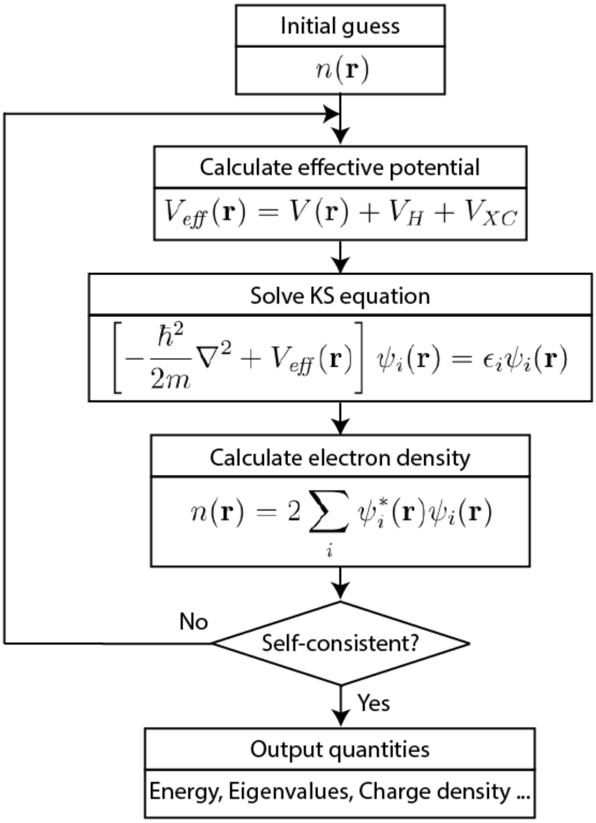
Initial guess
$n(\mathbf{r})$
Calculate effective potential
$V_{\mathit{eff}}(\mathbf{r}) = V(\mathbf{r}) + V_H + V_{XC}$
Solve KS equation
$\left[-\frac{\hbar^2}{2m}\nabla^2 + V_{\mathit{eff}}(\mathbf{r})\right]\psi_i(\mathbf{r}) = \epsilon_i\psi_i(\mathbf{r})$
Calculate electron density
$n(\mathbf{r}) = 2\sum_i \psi_i^*(\mathbf{r})\psi_i(\mathbf{r})$
Self-consistent?
No
Yes
Output quantities
Energy, Eigenvalues, Charge density ...

Figure 2.10: *Simple flow chart of a typical Kohn-Sham based density functional calculation.*

The main contribution to the exchange-correlation energy originates from the effect of *Fermi holes* and *Coulomb holes*. The latter is due to the electrostatic repulsion (Coulomb correlation) between electrons, which creates a region between each electron in which no other electrons are found. This creates a ”hole” in the electron density. A similar hole in the density arises from the Pauli exclusion principle (via exchange), which states that electrons with the same spin can not occupy the same space. A good model for the exchange-correlation energy must also correct for the electron self-interaction in the Hartree potential and the fact that the kinetic energy of the non-interacting electrons in the KS-equations may differ from the real case of interacting electrons [16].

Even though we know that E_{XC} must exist, the exact form is yet to be uncovered. This leaves us to make approximations. The *local density approximation* (LDA) utilizes the fact that in a uniform electron gas the exact exchange energy is known. Thus LDA is a rather crude approach where a local homogeneous gas is defined in each point, with the electron density found in that particular point. The *generalized gradient approximation* (GGA) on the other hand, introduces a more general form of the exchange-correlation energy. GGA includes both a function (f) of the electron density and *the gradient* of this function. By including the gradient one obtains a better description of the transition from one local point to another. Many different versions of f exist, providing a myriad of distinct GGA functionals. Perhaps most commonly used for solids are the Perdew-Wang (PW91) and Perdew-Burke-Ernzehnhof (PBE) functionals. The GGA approximation remedies the short-comings of LDA to a large extent [17]. However, GGA too has its limitations, for instance in correct prediction of band gaps. More sophisticated techniques do exist, but this is beyond the scope of this particular thesis.

The last fundamental ingredient needed to perform DFT calculations is the wave functions, which have to be expressed by a limited number of basis functions. The higher the number the higher the accuracy, but unfortunately the computation time will increase accordingly. The main difficulty in choosing a basis set is the very different behaviour near an atom and in the interstitial regions. In the region close to an atom the wave functions and potential are almost spherical in symmetry and vary strongly with radial distance, while in the voids between atoms the wave functions and potential are quite smooth. In general three different types of basis sets are used [18, 19]: Linear combination of atomic orbitals (LCAO), linear augmented plane waves(LAPW), and projected augmented waves (PAW), which utilizes plane waves in combination with pseudo-potentials (PP). In the first method the wave function is made up of a linear combination of orbitals of isolated atoms. Intuitively this corresponds well with the chemical picture and atoms and molecules are described well. For materials with delocalized states, however, it is not a good choice. In such cases one tend to turn to plane waves, which make use of the periodicity of crystal structures. The LAPW method divides space into two types of regions: spheres centered around the atoms are described by spherical waves while the space around them, the interstitial region, is described by plane waves. The two different descriptions have to meet at the boundaries between the two regions and the radius of the atomic spheres has to be specified. In the PP method a pseudo potential is constructed to describe the core area of each atom in a manner that is more easily represented by plane waves. Only the valence electrons are treated explicitly and all information about charge density and wave functions near the nucleus is lost. In the PAW method the ideas of augmented plane waves and pseudo potentials are brought together. The key ingredient is a transformation that maps the true wave functions onto numerically well behaved pseudo wave functions. The pseudo wave functions are expanded into a basis set that is convenient for calculations and after solving the Schrödinger equation the physical properties of the system can be evaluated simply by transforming the pseudo wave functions back to the true wave functions. Unlike the PP method PAW is an all electrons method in most practical respects, but not in the sense that all electrons of the system are taken into account self-consistently [20].

2.2.2 Atoms in crystals: Bader analysis and local DOS

The electron density obtained from a DFT calculation is continuous, describing the crystal as a whole. Thus dividing this crystal into regions representing atoms is not trivial from an electron density point of view. In this work individual atoms were studied using two different approaches, local density of states (LDOS) calculations and so-called Bader analysis. In the former method the l-projected DOS is calculated based on the description of each atom already given through the atomic input potentials.[3] The LDOS is not normalized. In figure 2.11 a) the total DOS for a model with 18.75 at. % Ti is compared to different combinations of the separate LDOS for Mg and Ti.[4] Simply adding the latter two largely reproduces the shape of the total DOS, but the intensity is too low. Trying to scale the LDOS according to the composition of the calculated model gave an intensity that was either much too high, or much too low when divided by the total number of atoms. The same tendency can be seen when trying to add the s-, p- and d-projected DOS. Thus it is clear that the LDOS approach has difficulties in accounting for the full electron charge density, and in our case some of the charge was simply lost.

---

[3] In paper II there was some confusion regarding Wigner Seitz radii defining the atomic volumes. It seems now that the these radii were in fact not used in the performed LDOS calculations.

[4] The element specific LDOS is just the sum of the l-projected DOS for each atom of that species.

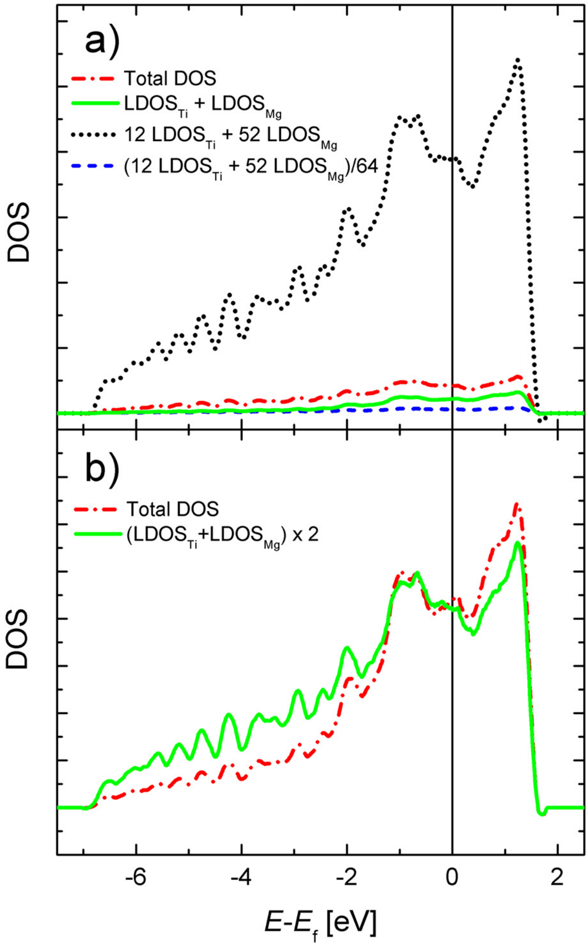

Figure 2.11: *Total DOS for a model with 18.75 at. % Ti compared to different combinations of the separate LDOS for Mg and Ti(a). In (b) the summed LDOS has been scaled in order to compare the qualitative shape of the graph to the total DOS. The spectra have been smoothed using a Savitzky-Golay method included in the Origin software [21].*

Bader analysis offers a more intuitive way of dividing the space of a crystal into atoms. It is based on the realization by R. Bader *”that the topology of the electron density (...) provided a unique and ”natural” partitioning of the space of a molecule or a crystal into mononuclear regions”*. (Quote from ref. [22].) Through his work it was established that two atoms that looks the same in real space possess the same energy, and his definition of the atom meets the requirement that when summing over all atoms the total energy is yielded. Essentially, the atoms are confined in volumes which surfaces are drawn perpendicular to minima in the charge density, so-called zero flux surfaces. This way the problem of ”lost” charge observed for the LDOS method can be minimized and one is left with a picture of individual atoms that is pleasantly tangible. The computational challenge becomes to define the dividing surfaces; finding the charge density minima. Finding the critical points in the electron density and describing the dividing surfaces can be computationally expensive. In the present work a program developed by Arnaldsson *et al.* was used [23]. It is based on a fast and robust algorithm which assigns each electron density point on a regular (x, y, z) grid to appropriate atomic regions by following a steepest ascent path on the grid [24]. This way an explicit definition of the zero flux surfaces can be avoided. In our work the sum of electron charge contained in the Bader volumes added up nicely to the total electron charge of the system, in contrast to what was seen for the LDOS approach. In paper II, where both integrated LDOS and Bader analysis were used to investigate the charge distribution between Mg and Ti, contradictory results were obtained. The Bader results were judged most reliable, and thus the Bader method was employed further in paper IV and V.

2.2.3 DOS vs. XPS valence spectra

In principle the valence spectra obtained by XPS correspond to the DOS below the Fermi level, and in many instances DOS obtained from DFT can aid the interpretation of data obtained by XPS [6, 25]. However, in order to compare the calculated DOS to experimental spectra a couple of adjustments have to be made. Firstly, the experimental broadening must be taken into account. In general this is not a straight forward task. However, for the level of accuracy obtained in the XPS valence spectra in this work, a simple estimation of the broadening was judged to be sufficient. A second factor to consider is the different photoionization cross sections of the different atoms and orbitals. In this work the photoionization cross sections calculated by Yeh and Lindau [26] were used to scale the DOS. In order to achieve this the l-projected LDOS for each element had to be used. However, as described in the previous section, the LDOS contributions do not add up to the total DOS, making the result somewhat uncertain. In our particular case the interesting part of the DOS was the region just below the Fermi level, in which our two models showed distinctly different behaviour. From figure 2.11 b) it is clear that summing the LDOS contributions adequately reproduces the shape of the total DOS in this region. Thus it was decided to adjust the LDOS contributions for the photoionization cross sections and retrieve the total DOS directly by summing the adjusted LDOS. Figure 2.12 shows an example of how the relative intensities of the different orbitals shift upon correction for the photoionization cross sections.

2.2.4 Computational details

The aim of the project was to investigate the structure of Mg-Ti thin films. Experimentally one had found evidence for a certain short range chemical order [27, 28], and we wanted to see whether this could be supported by DFT calculations. Two models were constructed: In the *quasi-random* (QR) model the Ti atoms were distributed randomly in the Mg supercell, while in the *nano-cluster* (NC) model the Ti atoms were brought together in small clusters. Figure 2.13 shows examples of NC and QR models of two different supercell sizes. The size of the supercell was chosen to balance the trade-off between computational cost and the need both for solid solution randomness and for flexibility in composition and cluster size. The size of the supercell and clusters will be discussed in more detail towards the end of this section. The randomness was described in terms of the short range chemical order parameter (s), which was quantified as follows [29]:

$$s = 1 - \frac{N - N_{\text{Ti-Ti}}}{N(1-y)} \tag{2.15}$$

where $(1 - y)$ is the atomic fraction of Mg. $N_{\text{Ti-Ti}}$ is the average number of Ti atoms in the first coordination sphere around a Ti atom, and N is the total number of atoms in the first coordination sphere.

DFT calculations were performed using the Vienna ab-initio simulation package (VASP) [30, 31]. The Kohn-Sham equations were solved using a basis of projector augmented wave functions [19] with a plane-wave energy cut-off of 350 eV. The Perdew-Burke-Ernzerhof 96 (PBE) generalized gradient approximation was used for the electron exchange correlation functional [32]. The criterion for electronic convergence was a change of the total energy less than 10^{-5} eV. The smearing width was 0.2 eV. The energy cut-off and number of k-points was tested: The total energy was converged down to < 0.00001 eV and < 0.003 eV for the energy cut-off and k-points, respectively.

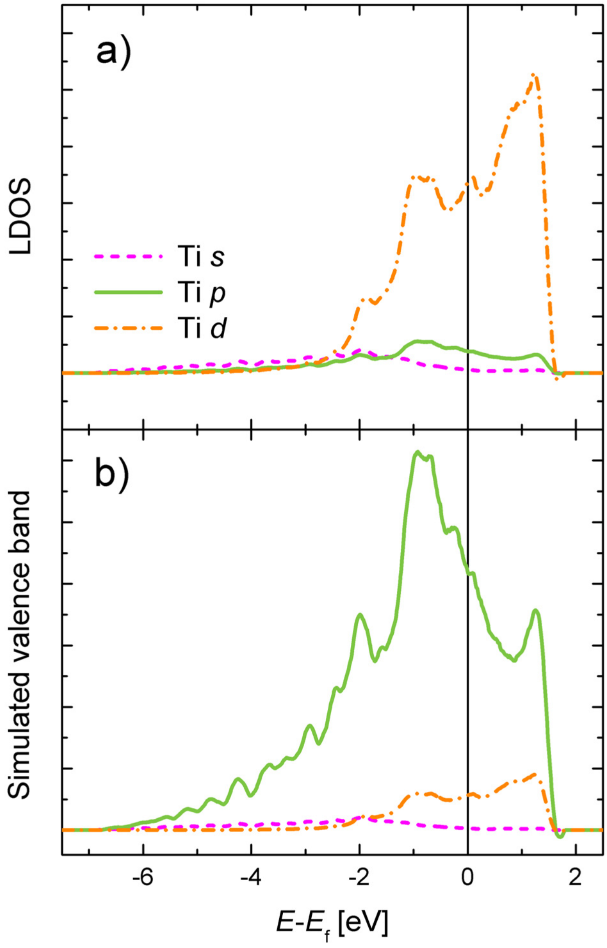

Figure 2.12: *s, p and d-projected DOS (LDOS) for a Mg-Ti model with 18.75 at.% Ti (a). In (b) the LDOS has been corrected for photoionization cross sections in order to obtain a simulated valence band structure. The spectra have been smoothed using a Savitzky-Golay method included in the Origin software [21].*

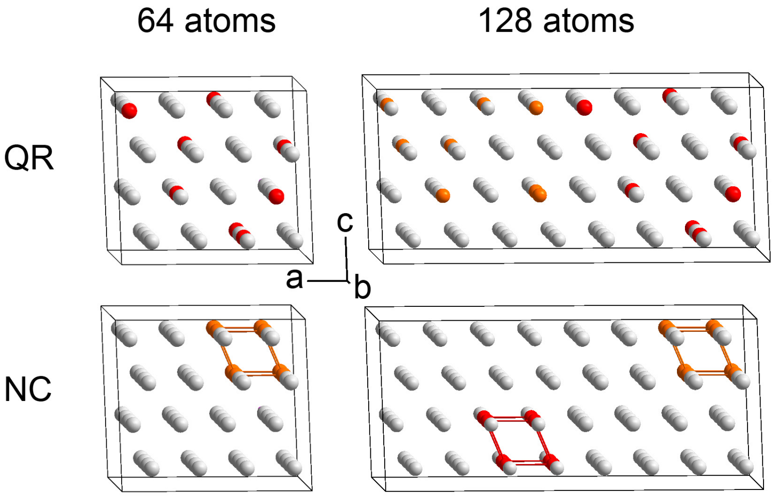

Figure 2.13: *Examples of NC and QR models of Mg-Ti for the composition with 12.5 at.% Ti, with 64 and 128 atoms in the supercell. White atoms represent Mg and colored atoms represent Ti.*

Structural optimizations were performed, with volume, lattice parameters and atom positions allowed to change simultaneously. The break condition for the relaxation loop was set to forces < -0.05 eV/Å. The mixing enthalpy of the alloys was calculated as follows:

$$\Delta H_f = E_{\mathrm{Mg}_{100-y}\mathrm{Ti}_y} - (100-y)E_{\mathrm{Mg}} - yE_{\mathrm{Ti}} \tag{2.16}$$

where $E_{\mathrm{Mg}_{100-y}\mathrm{Ti}_y}$, E_{Mg} and E_{Ti} are the calculated energies of alloy, pure Mg and pure Ti respectively. The mixing enthalpy *per Ti atom* or *per* H_2 was used for comparisons between the different compositions. The hydrogenation energy E_{H} was defined as $E_{\mathrm{H}} = E_{\text{Mg-Ti-H}} - (E_{\text{Mg-Ti}} + \frac{x}{2}E_{\mathrm{H}_2})$, where $E_{Mg-Ti-H}$ is either fcc hydride structure or hcp metal structure with H and E_{Mg-Ti} is the hcp metal structure without H.

In paper II calculations were done for $\mathrm{Mg}_{100-y}\mathrm{Ti}_y$ with compositions $1.56 \leq y \leq 98.44$. In this paper we wanted to see whether segregation of Ti on a scale below the XRD detectable limit could be energetically favourable. Parallel calculations were performed for Ti distributed both quasi-randomly and arranged in nano-clusters. The standard hexagonal structure of Mg was used as a starting point. We started with a super cell consisting of 64 atoms in total, equal to 4x4x2 Mg unit cells. In the QR calculations the Ti atoms were manually distributed in the 64 atom cell in a random manner. The number of Ti atoms in the first coordination sphere of Ti $N_{\text{Ti-Ti}}$ ranged from 0 for $y = 1.56$ to < 2 for $y = 25$. To construct the Ti nano-clusters in the NC model planes of four Ti atoms were stacked together in the a direction for compositions $y = 6.25$, 12.5 and 18.75. For the composition with $y = 25$ the super cell was increased to 96 atoms in order to facilitate the nano-cluster, which was given a more quadratic shape. The compositions with $y > 50$ were mirrored versions of the corresponding compositions with $y < 50$. The initial NC models were labeled *original*. Through the course of the work several alternative configurations were constructed to test the effect of cluster size by varying the chemical short-range parameter, s. Table 2.2 lists all the NC models calculated in paper II. A 5x5x7 Gamma sampling of k-points was used to model the Brillouin zone for the cell containing 64 atoms, a 5x5x5 sampling was used for the cell containing 96 atoms and a 3x3x5 sampling was used for the even larger cells. The mixing enthalpy and its relation to the short range order were investigated, as well as relaxed cell parameters and the density of states. In addition both local DOS projections and Bader analysis were employed to analyze the interactions between Mg and Ti. Finally the charge density for the 12.5 at.$\%$ Ti composition was compared to the hypothetical charge density of the *so-called* procrystal. The charge density of the procrystal is made up of non-interacting atoms placed in the crystal structure of comparison, thus the charge difference between the calculated model and the procrystal may give a clearer picture of the electron interactions between Mg and Ti in a particular crystal structure.

In paper III the DOS calculated for the QR and NC models from paper II were investigated further. Using local DOS calculations the contributions from Mg and Ti to the total DOS were separated to further investigate the preference for Ti nano-cluster formation. The distinct qualitative difference between the DOS for the QR and NC models inspired a comparison to the XPS valence spectrum of a real Mg-Ti sample. In order to do this the calculated DOS was scaled using photoionization cross sections from Yeh and Lindau [26].

In paper IV hydrogen was introduced into the metallic (hcp) model with composition $y = 18.75$. This composition was chosen from paper II because it was closest to the $y = 20$ sample that was investigated experimentally. H has the choice of occupying octahedral (oct) or tetrahedral (tet) sites in the structure, as illustrated in figure 2.14. As a first step calculations were performed for a single H atom at different positions in both the NC and the QR model to get an overview of the effect. It was found that placing H on sites with both Mg and Ti nearest neighbors, lead to a further stabilization of the system. The effect was strongest for occupation of octahedral sites in the NC model. The occurrence of each octahedral site with $\text{nn}_{\text{Ti}} = 6, 3, 2, 1$ and 0 in the unit cell is $2, 10, 8, 14$ and 30, respectively. The second step was to gradually increase the H

Table 2.2: *Average number of Ti atoms on nearest neighbor sites around Ti ($N_{\text{Ti-Ti}}$) and chemical short-range parameter (s), with corresponding values calculated for the mixing enthalpy per Ti atom, for all NC models. The unit cell names give the number of Mg and Ti atoms. Original models in* ***bold****.*

Composition	**Unit cell**	$N_{\textbf{Ti-Ti}}$	s	**Mixing enthalpy per Ti [meV/Ti]**
$Mg_{93.75}Ti_{6.25}$	**Mg60Ti4**	2.500	0.16	349
	Mg60Ti4	3.000	0.20	273
$Mg_{87.50}Ti_{12.50}$	**Mg56Ti8**	4.500	0.29	214
	Mg56Ti8-(2parts)	3.000	0.14	345
	Mg189Ti27	6.666	0.49	190
	Mg252Ti36 (2parts)	5.666	0.40	246
	Mg252Ti36	7.030	0.53	184
$Mg_{81.25}Ti_{18.75}$	**Mg52Ti12**	5.167	0.30	225
$Mg_{75.00}Ti_{25.00}$	**Mg72Ti24**	6.708	0.41	187
	Mg72Ti24	5.917	0.32	194
$Mg_{12.50}Ti_{87.50}$	**Mg8Ti56**	4.500*	0.29*	330

* $N_{\text{Mg-Mg}}$

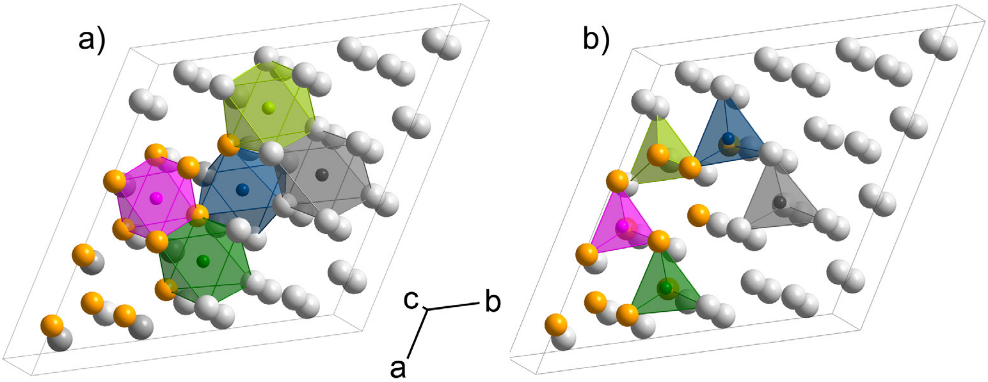

Figure 2.14: *The different sites for interstitial H in the NC model with 18.75 at % Ti: octahedral (a) and tetrahedral (b). Mg atoms are shown in white while Ti atoms are shown in orange. The sites fully coordinated by Ti are illustrated in pink and the sites with $nn = 3, 2, 1$ and 0 are illustrated in green, blue, lime and grey, respectively.*

content, starting with the most stable sites on the interface between the Ti nano-clusters and the Mg matrix, i.e., the sites with $\mathrm{nn_{Ti}} = 3$. Then the rest of the sites were filled in decreasing $\mathrm{nn_{Ti}}$ order. For certain H contents alternative filling orders were tested. Table 2.3 gives an overview of all the calculated compositions in the filling sequence. Test calculations were also done for the hydride phase for comparison. For the hydride phase a 2x2x3 TiH_2-type (fcc) unit cell (48 atoms) was used, with the experimental lattice parameters of Vermeulen *et al.* [33] as a starting point. Bader analysis of the hydrogenated models was included in paper V to support experimental findings.

Accepting the limitations of the DFT-method the most crucial influence on the viability of the result becomes the choice of input model. The inherent periodicity of our calculations means that our model can never match the true randomness of a real solid solution. The question becomes whether our model is *good enough*. In our work we decided on a supercell consisting of 64 atoms, which would provide a reasonable flexibility in terms of atomic composition as well as allowing the formation of Ti nano-clusters. For the QR models in paper II this choice was never really questioned, other than observing that the manual distribution of Ti atoms resulted in slightly less Ti-Ti interactions ($s < 0$) than would be the case in a truly random distribution ($s = 0$). For the NC model, on the other hand, it became necessary to perform calculations for a variety of supercell sizes and nano-cluster shapes. As can be seen in table 2.2, and paper II (figure 3) the mixing enthalpy was found to increase with the short range order, up to a point where the energy gain upon increased cluster size started to diminish. Most importantly the size and short range order of the calculated nano-clusters correspond well to the experimentally derived models by Baldi *et al* [28]. Thus it seems our model was adequate in terms of cluster size. The effect of long range ordering has been tested in a systematical manner for the 12.5 at. $\%$ Ti composition. The models are listed in table 2.4. For the NC model, which has a constant s value, the mixing enthalpy per Ti atom is practically unaffected by the decrease of long range ordering. For the QR model, for which a constant s value was harder to construct, the mixing enthalpy per Ti atom fluctuates somewhat. However, it seems evident that the strongest influence comes from the local rather than the long rang ordering, i.e., the effect of clustering outweighs any possible effect of randomness. In conclusion, the supercell sizes investigated in the present project seem to be an adequate representation of reality, both in terms of nano-cluster size and long range ordering.

Table 2.3: *Hydrogen configurations in calculated models from paper IV. The metallic (hcp) matrix consisted of 52 Mg atoms with 12 Ti atoms arranged in a nano-cluster. The octahedral voids in the structure are labeled after the number of Ti atoms (nn_{Ti}) in the first coordination sphere. Hydrogen was introduced as listed below.*

	nn_{Ti} (octahedral voids)				
H atoms	**6**	**3**	**2**	**1**	**0**
1		1			
2		2			
2	2				
3		3			
4		4			
5		5			
6		6			
6	2	4			
7		7			
8		8			
9		9			
10		10			
12		10	2		
12	2	10			
14		10	4		
16		10	6		
18		10	8		
18	2	10	6		
20		10	8	2	
20	2	10	8		
32		10	8	14	
32	2	10	8	12	
34	2	10	8	14	
64 (all sites)	**2**	**10**	**8**	**14**	**30**

Table 2.4: *Different supercell sizes for the composition with 12.5 at. % Ti, both quasi-random (QR) and nano-cluster (NC) models. For definition of short range order see text.*

Total no. of atoms	Supercell composition	Model	No. of Ti clusters	Short range order s	Mixing enthalpy per Ti [eV/Ti]
32	Mg28Ti4	QR	-	-0.14	0.74383
32	Mg28Ti4	QR	-	-0.05	0.70881
64	Mg56Ti8	QR	-	-0.10	0.77893
128	Mg112Ti16	QR	-	-0.06	0.69587
256	Mg224Ti32	QR	-	-0.06	0.69691
64	Mg56Ti8	NC	1	0.29	0.21361
128	Mg112Ti16	NC	2	0.29	0.22232
256	Mg224Ti32	NC	4	0.29	0.22125

References

[1] Watts, J. F. & Wolstenholme, J. *An introduction to surface analysis by XPS and AES* (John Wiley & Sons, 2003).

[2] Sholl, D. S. & Steckel, J. A. *Density functional theory: a practical introduction* (Wiley, 2009).

[3] Briggs, D. *Surface analysis by Auger and X-ray photoelectron spectroscopy*, chap. XPS: Basic principles, spectral features and qualitative analysis, 44 (IM Publications and SurfaceSpectra Limited, 2003).

[4] Briggs, D. & Rivière, J. C. *Practical surface analysis - Auger and x-ray photoelectron spectroscopy*, vol. 1, chap. 3: Spectral interpretation, 85–141 (John Wiley & Sons, 1990), 2nd edn.

[5] Delhalle, J. & Deleuze, M. Insights into the molecular structure and chemical bonding of regular oligomers and polymers from their XPS valence spectra. *J. Mol. Struct.* **261**, 187–202 (1992).

[6] Sunding, M. F. *et al.* XPS characterisation of *in situ* treated lanthanum oxide and hydroxide using tailored charge referencing and peak fitting procedures. *J. Electron. Spectrosc. Relat. Phenom.* **184**, 399–409 (2011).

[7] Egerton, R. F. *Electron Energy-Loss Spectroscopy in the Electron Microscope* (Springer, 2011), 3rd edn.

[8] Scofield, J. H. Hartree-Slater subshell photoionization cross-sections at 1254 and 1487 eV. *J. Electron Spectrosc. Relat. Phenom.* **8**, 129–137 (1976).

[9] Wagner, D. C. Auger lines in X-ray photoelectron spectrometry. *Anal. Chem.* **66**, 967–973 (1972).

[10] Thomas, T. D. Extra-atomic relaxation energies and the Auger parameter. *J. Electron. Spectrosc. Relat. Phenom.* **20**, 117–125 (1980).

[11] Thomas, T. D. & Weightman, P. Valence electronic structure of AuZn and AuMg alloys derived from a new way of analyzing Auger-parameter shifts. *Phys. Rev. B* **33**, 5406–5413 (1986).

[12] Drummond, I. W. *Surface analysis by Auger and X-ray photoelectron spectroscopy*, chap. XPS: Instrumentation and performance, 136 (IM Publications and SurfaceSpectra Limited, 2003).

[13] Diplas, S., Shao, G., Tsakiropoulos, P., Watts, J. F. & Matthew, J. A. D. Calculations of charge transfer in Mg- and Al-transition metal alloys using the Auger parameter. *Surf. Interface Anal.* **29**, 65–72 (2000).

[14] http://www.casaxps.com. (2012).

[15] Shirley, D. A. High-Resolution X-Ray Photoemission Spectrum of the Valence Bands of Gold. *Phys. Rev. b* **5**, 4709–4714 (1972).

[16] Koch, W. & Holthausen, M. C. *A chemist's guide to density functional theory* (Wiley, 2001).

[17] Perdew, J. P. *et al.* Atoms, molecules, solids, and surfaces: Applications of the generalized gradient approximation for exchange and correlation. *Phys. Rev. B* **46** (1992).

[18] Blöchl, P. E. Projector augmented-wave method. *Phys. Rev. B* **50**, 17953–17979 (1994).

[19] Kresse, G. & Joubert, D. From ultrasoft pseudopotentials to the projector augmented-wave method. *Phys. Rev. B* **59**, 1758–1775 (1999).

[20] Marsman, M. & Kresse, G. Relaxed core projector-augmented-wave method. *J. Chem. Phys.* **125**, 104101 (2006).

[21] http://www.OriginLab.com.

[22] Bader, R. W. Some notes on the career in science of Richard F. W. Bader of McMaster University. http://www.chemistry.mcmaster.ca/bader/bio/highschool.htm (2012).

[23] http://theory.cm.utexas.edu/bader/.

[24] Henkelman, G., Arnaldsson, A. & Jónsson, H. A fast and robust algorithm for Bader decomposition of charge density. *Comput. Mater. Sci.* **36**, 254–360 (2006).

[25] Panaccione, G. *et al.* High-energy photoemission in silver: resolving d and sp contributions in valence spectra. *J. Phys.: Condens. Matter* **17**, 2671–2679 (2005).

[26] Yeh, J. J. & Lindau, I. Atomic subshell photoionization cross sections and asymmetry parameters: $1 \lesssim Z \lesssim 103$. *At. Data Nucl. Data Tables* **32**, 1–155 (1985).

[27] Gremaud, R., Baldi, A., Gonzalez-Silveira, M., Dam, B. & Griessen, R. Chemical short-range order and lattice deformations in $Mg_yTi_{1-y}H_x$ thin films probed by hydrogenography. *Phys. Rev. B* **77**, 144204 (2008).

[28] Baldi, A. *et al.* Nanoscale composition modulations in $Mg_yTi_{1-y}H_x$ thin film alloys for hydrogen storage. *Int. J. Hydrogen Energy* **34**, 1450–1457 (2009).

[29] Warren, B. E., Averbach, B. L. & Roberts, B. W. Atomic size effect in the X-ray scattering by alloys. *J. Appl. Phys.* **22**, 1493–1496 (1951).

[30] Kresse, G. & Furthmüller, J. Efficient iterative schemes for ab initio total-energy calculations using a plane-wave basis set. *Phys. Rev. B* **54**, 11169–11186 (1996).

[31] Kresse, G. & Furthmüller, J. Efficiency of ab-initio total energy calculations for metals and semiconductors using a plane-wave basis set. *Comp Mater Sci* **6**, 15–50 (1996).

[32] Perdew, J. P., Burke, K. & Ernzerhof, M. Generalized gradient approximation made simple. *Phys. Rev. Lett.* **77**, 3865–3868 (1996).

[33] Vermeulen, P., Graat, P. C. J., Wondergem, H. J. & Notten, P. H. L. Crystal structures of Mg_yTi_{100-y} thin film alloys in the as-deposited and hydrogenated state. *Int. J. Hydrogen Energy* **33**, 5646–5650 (2008).

Chapter 3

The Mg-Ti-H system

Even though magnesium and titanium do not form alloys and have negligible solubility the combination of the two has received a fair share of attention, both in the context of hydrogen storage and towards improving corrosion resistance of Mg as a structural material. This chapter gives an overview of some of the existing knowledge relevant to the current project.

3.1 Structure

The structural parameters of pure Mg and Ti are listed in table 3.1 along with their hydrides. Both Mg and Ti have hexagonal close packed (hcp) structures in the metallic state, with the size of the unit cell adjusted according to atomic radius. MgH_2 forms a tetragonal *rutile* structure, while TiH_2 forms a cubic *fluorite* structure.

As Mg-Ti samples have to be made by non-equilibrium techniques the structure of such metastable alloys is not obvious. In 2002 Mitchell *et al.* [1] investigated a series of Mg-Ti samples

Table 3.1: *Mg-Ti-H structure data*

	Space group	Hermann-Mauguin symbol	Crystal system	Structure type	Parameters a, c/[Å]	Band gap [eV]
Mg	194	$P6_3/mmc$	hexagonal		3.209, 5.210	Metallic
Ti	194	$P6_3/mmc$	hexagonal		2.951, 4.684	Metallic
MgH_2	136	$P4_2/mnm$	tetragonal	Rutile	4.517, 3.021	5.58
TiH_2	225	$Fm\bar{3}m$	cubic	Fluorite	4.535	Metallic

Table 3.2: *Experimental* $Mg_yTi_{1-y}H_x$ *structure data.*

From Mitchell *et al.* [1]						From Vermeulen *et al.* [2]					
Comp.		**Crystal**	**Lattice parameters**			**Comp.**		**Crystal**	**Lattice parameters**		
y	***x***	**system**	***a, b*/[Å]**	***c*/[Å]**	α/[°]	***y***	***x***	**system**	***a, b*/[Å]**	***c*/[Å]**	α/[°]
1	0	hcp	3.21	5.21	120	0.9	0	hcp	3.19	5.12	120
0.99	0	hcp	3.21	5.20	120	0.8	0	hcp	3.16	5.10	120
0.96	0	hcp	3.20	5.16	120	0.7	0	hcp	3.11	5.02	120
0.95	0	hcp	3.19	5.15	120	0.9	~ 2	bct	4.48	2.99	90
0.93	0	hcp	3.19	5.15	120	0.8	~ 2	fcc	4.71	4.71	88.5
0.88	0	hcp	3.16	5.10	120	0.7	~ 2	fcc	4.66	4.66	89

made by physical vapour deposition (PVD), with Ti content ranging from 0.87 to 12.4 at.% . Using X-ray diffraction (XRD) they concluded that Mg and Ti were in solid solution and that the variations in lattice parameters were influenced mainly by the atomic size factor. Vermeulen *et al.* also investigated the crystal structure of $Mg_yTi_{(1-y)}$ samples with y =90, 80 and 70. DC/RF sputtered samples were measured with and without hydrogen using *in situ* X-ray diffraction [2]. In all cases the as deposited samples had a hexagonal close packed structure similar to the structure of pure Mg and Ti. For the hydrides, a face-centered cubic symmetry was found for the $Mg_{70}Ti_{30}$ and $Mg_{80}Ti_{20}$ compounds, while the unit cell of hydrogenated $Mg_{90}Ti_{10}$ was body-centered tetragonal. The experimental lattice parameters from Mitchell *et al.* [1] and Vermeulen *et al.* [2] are given in table 3.2. The correspondence between the data is not complete, for instance does the $y = 0.88$ composition measured by Mitchell *et al.* have the same cell parameters as the $y = 0.8$ composition measured by Vermeulen *et al.*. It might seem that accurate determination of the composition is not trivial. The existence of a structural transition point for the hydride was supported by ground state density functional theory (DFT) calculations [3, 4] of ordered models of Mg-Ti. It was found that for Ti contents above 20 at.% the Mg-Ti-hydride does indeed change from the body centered tetragonal structure of pure MgH_2 into a face-centered cubic structure similar to that of TiH_2, in good agreement with the experiments. However, the reasons why such relatively small amounts of Ti would cause Mg to form a cubic hydride were not explained.

The first extensive investigation of both the structure and optical and electrical properties of magnetron sputtered $Mg_yTi_{(1-y)}$ thin films with and without hydrogen was performed by Borsa *et al.* in 2007 [5]. XRD measurements of samples with 10 and 30 at.% Ti gave only one reflection peak from the Mg-Ti layer, corresponding to a hexagonal structure in the metallic state. The hexagonal structure was confirmed also by transmission electron microscopy (TEM). As large scale phase separation seemed out of the picture and alloy formation was deemed highly unlikely

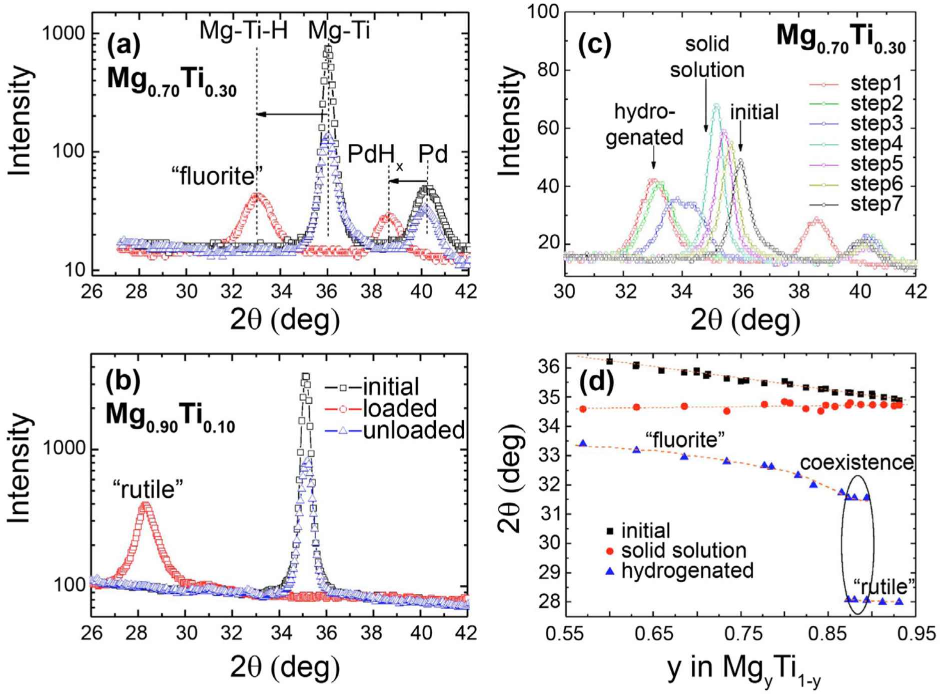

Figure 3.1: ***(a and b)*** *$\theta - 2\theta$ X-ray scans measured on 200 nm $Mg_yTi_{(1-y)}$/10 nm Pd films (y=0.70 and y=0.90) in the as-prepared (initial), fully hydrogenated at room temperature in 1 bar H_2(loaded), and fully dehydrogenated (unloaded) states.* ***(c)*** *Intermediate steps during dehydrogenation measured on a y=0.70 sample.* ***(d)*** *Composition dependence of 2θ measured on a $Mg_yTi(1-y)$ gradient thin film with $0.55 < y < 0.95$. Data corresponding to as-prepared (initial), solid solution (intermediate), and hydrogenated (final) states as defined in (c) are shown. From ref. [5].*

the conventional alternative would be solid solution. However, due to the high mixing enthalpy calculated for a random alloy of Mg and Ti [6] the authors suggested that Mg and Ti form a coherently coupled mixture with (small) separate areas of Mg and Ti. After hydrogenation the Ti poor sample with 10 at.% Ti was found to form a MgH_2-like rutile structure while the sample with 30 at.% Ti was found to form a TiH_2-like fluorite structure. The turning point between formation of a MgH_2-like and a TiH_2-like hydride phase was reported to be at a composition $0.87 < y < 0.9$. TEM indicated a structural homogeneity in the hydride phase at least on the scale above 20 nm. When hydrogen was unloaded the structure returned to the hcp metallic phase and the samples remained crystalline throughout the whole process. Remarkably Mg and

Ti did not segregate upon cycling, unlike several other Mg containing alloys, e.g., Mg-V [7], La-Mg [8], Gd-Mg [9] and Y-Mg [10]. Electrical, optical and structural data combined suggested a hydrogenation sequence where Ti related sites are filled first. As it turns out the molar volume of TiH_2 (13.3 cm^3) equals almost exactly that of pure Mg (13.98 cm^3) and it was argued that this was the cause of the reversibility of the system. Figure 3.2 illustrates the coherent structure and how the coinciding molar volumes of Mg and TiH_2 relax the structure at intermediate steps of the loading and unloading of hydrogen. The missing piece in the coherent structure picture was a fluorite MgH_2 phase, which had only been found at high pressures (4 GPa) [11].

The Bragg peak position (”scattering angle 2θ”) and the resistivity were measured in situ during hydrogenation of a sample with 30 at.% Ti, see figure 3.3. In the solid solution phase the Bragg peak position changed while the resistivity remained fairly constant. This was followed by the transformation to hydride state, where the resistivity started to increase. Surprisingly, the increase in resistivity continued even after the scattering angle had stabilized, giving reason to suspect the presence of a hydrogen absorbing amorphous phase. Estimates based on the electrical and optical measurements, however, turned out too be far too high ($\sim 45\%$) considering evidence of an amorphous phase was not seen with TEM.

Generally one finds that the total amount of H that can be stored in $Mg_yTi_{(1-y)}$ thin films is somewhat less than the stoichimetrical [H/M]$=2$ [12, 5], with the fraction decreasing with Ti content. In an *in-situ* electrochemical XRD study of (de)hydrogenation of Mg_yTi_{1-y} thin films Vermeulen *et al.* [13], found that the amount of H being retrieved from a Mg-Ti samples was about [H/M]=0.3 less than the amount initially absorbed, pointing to the presence of sites where H was very strongly bound.

Regarding the microstructure of Mg-Ti samples it had become clear that if Ti was separated from Mg it had to be in small particles of sizes below the XRD detectable range. From optical and electrical measurements Borsa *et al.* had already concluded that the hydrogenated samples would have to contain both metallic (TiH_2-like) and insulating (MgH_2-like) regions (see section 3.2) which indirectly predicted a certain local ordering of Mg and Ti [5]: For the hydrogenated sample with 30 at.% Ti the volume fraction of the insulating phase was about 75 % which pretty much accounts for all of the Mg in the sample. However, the number of complete Mg tetrahedra for H to occupy in a homogenous random model would be only $\sim \frac{1}{3}$ of this. New evidence for small scale separation was found from simulation of optical isotherms from hydrogenography by Gremaud *et al.* [14] in 2008 and was further verified by a combination of X-ray diffraction and Extended X-ray Absorbtion Fine Structure (EXAFS) spectroscopy performed by Baldi *et al.* [15] in 2009. The concept of *chemical short-range order* (CSRO) was introduced as a mean to

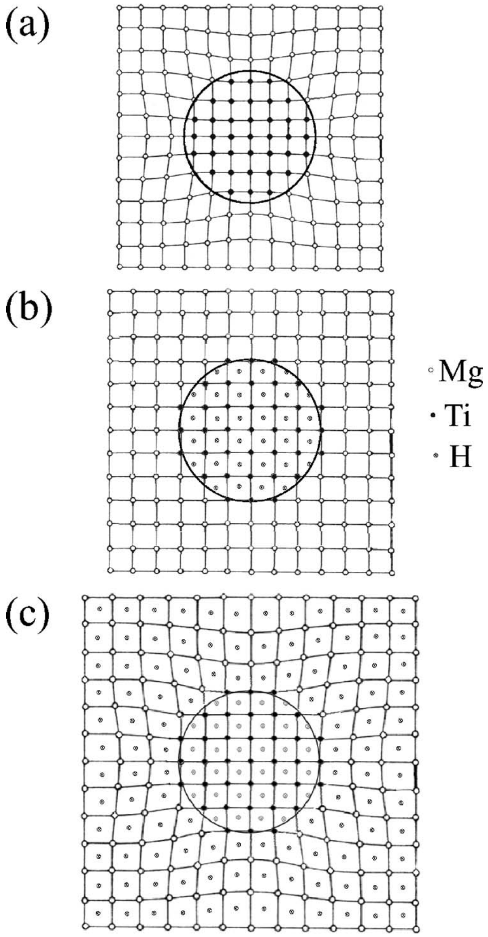

Figure 3.2: ***(a)*** *Schematic representation of a coherent crystalline grain consisting of a Mg and Ti region.* ***(b)*** *The same crystalline grain after hydrogen uptake in the Ti-related sites.* ***(c)*** *Full hydrogenation state. The accidental equality of the molar volumes of* TiH_2 *and Mg leads to an almost perfect crystal in situation (b). From ref. [5].*

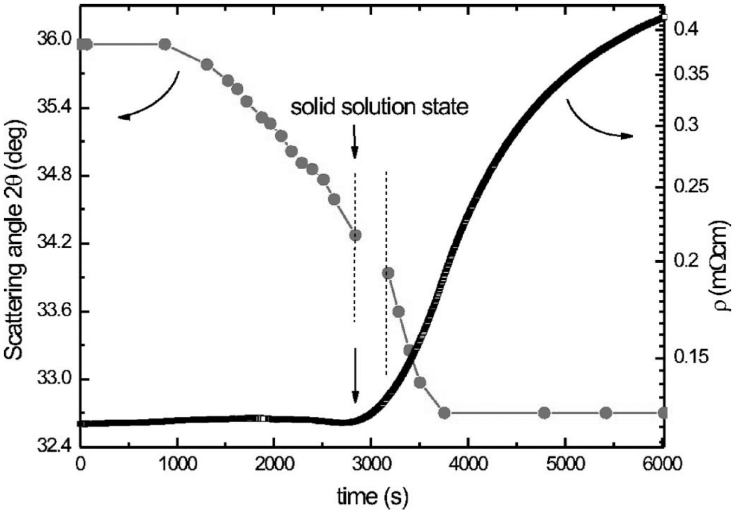

Figure 3.3: *Bragg peak position ("scattering angle* 2θ*") and electrical resistivity (*ρ*) evolution in time during hydrogenation measured simultaneously on a 200 nm* $Mg_{0.70}Ti_{0.30}$ */10 nm Pd sample. Hydrogenation was performed at room temperature in 100 mbar* H_2 *From ref. [5].*

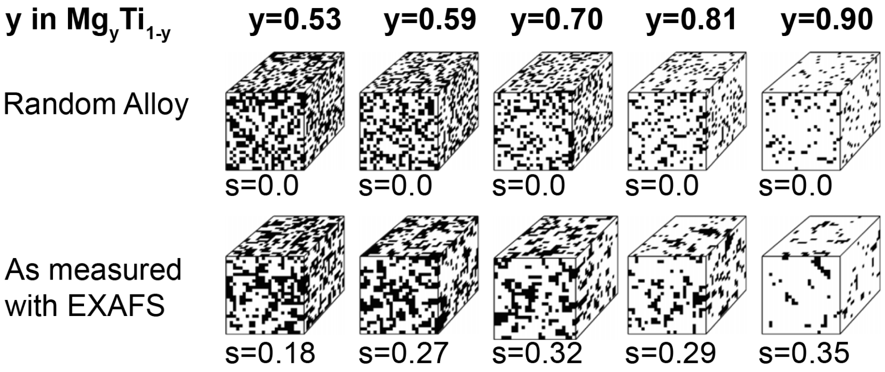

Figure 3.4: *3D-representation of Mg_yTi_{1-y} alloys with chemical short-range order parameters, s, as measured with EXAFS. For comparison the same compositions are shown for completely random distribution of Mg and Ti atoms (s=0). From ref. [15].*

describe the local structure in Mg-Ti samples. The CSRO parameter s is given by the equation [16]:

$$s = 1 - \frac{N - N_{\text{Ti-Ti}}}{Ny} \tag{3.1}$$

where $(1 - y)$ is the atomic fraction of Mg. $N_{\text{Ti-Ti}}$ is the average number of Ti atoms in the first coordination sphere around a Ti atom, and N is the total number of atoms in the first coordination sphere. In ref. [15] the CSRO parameters for $\text{Mg}_y\text{Ti}_{(1-y)}$ samples with $0.53 < y < 0.9$ were calculated from the N values obtained by EXAFS. $\text{Mg}_y\text{Ti}_{1-y}$ models with the measured s values were generated via 3D Monte Carlo simulations, assuming only nearest neighbor interactions and including periodic boundary conditions. The models are shown in figure 3.4 along with completely random models for comparison purposes, showing how Ti tend to segregate on the nano-scale.

In most of the previous DFT investigations of the Mg-Ti system minimum size supercells were used, resulting in a high degree of ordering. An exception is the work of Van Setten *et al.* [17], where special quasi-random structures which enable modeling of random alloys in a finite supercell were employed. Their supercell contained 32 atoms. The primary objective, however, was to study the optical properties of $\text{Mg}_{1-y}\text{Ti}_y\text{H}_2$, which will be discussed in the next section. During the course of the present work a DFT paper by Tao *et al.* [18] comparing ordered and segregated-type structures for $\text{Mg}_{75}\text{Ti}_{25}$ hydrides turned up. The results showed that the segregated-type fcc

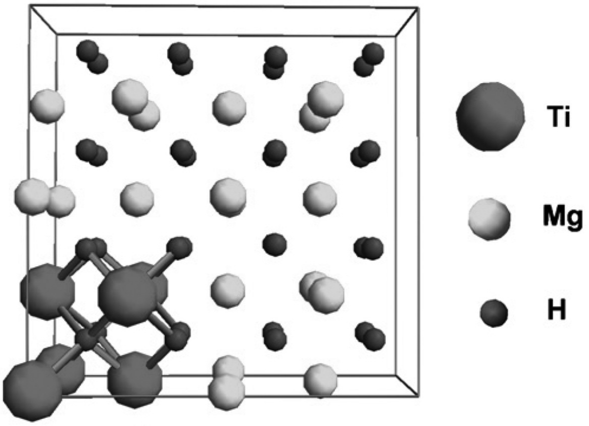

Figure 3.5: *Segregated-type structure used by Tao et al.[18] The Ti atoms fill the whole length of the unit cell in one direction, resulting in a structure with evenly spaced Ti nanowires in an Mg-matrix. Figure from ref. [18].*

hydride phase was stable (relative to the elemental states) down to very low hydrogen contents; less than H/M=0.1. This did not correspond well with our ongoing work, which is presented in paper IV. However, it soon became clear that the segregated unitcell in the work of Tao *et al.* was in fact describing a Ti nanowire, as can be seen in figure 3.5. Thus these results were judged less relevant for comparison with the real thin film samples. The influence of Al distribution in a supersaturated $Ti_{1-x}Al_xN$ alloy was investigated by Mayrhofer *et al.* [19]. It was found that the meta-stable solubility limit of AlN in cubic $Ti_{1-x}Al_xN$ could be increased by reducing the number of Al-Ti bonds, i.e., by small scale clustering. However, such studies do not appear to be widespread. Regarding immiscible elements, most DFT-investigations seem to be focused on surface alloying rather than bulk mixing, for instance in connection to catalysis [20, 21].

3.2 Electrical and optical properties

The discovery of the so-called switchable mirrors of Y-H and La-H in 1996 [22] sparked an interest in thin film hydrides, leading to the discoveries of several hydride systems with tunable electrical and optical properties [23, 24, 25, 8, 26]. Mg-Ti thin films stand out among them, as they appear black rather than transparent in the fully hydrogenated state. The electrical and optical properties of Mg_yTi_{1-y} thin films with $y = 0.9, 0.8,$ and 0.7 were extensively studied

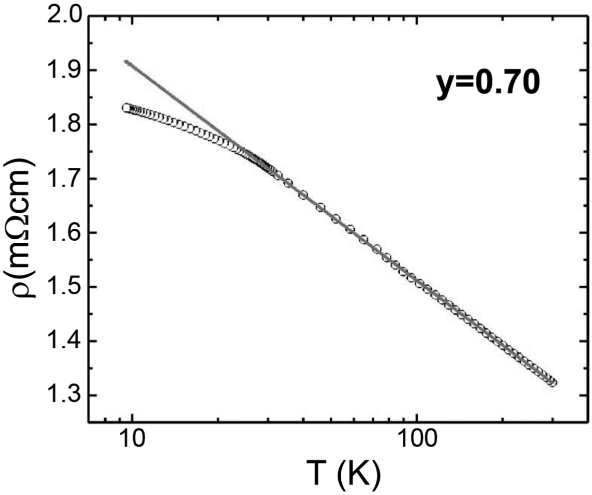

Figure 3.6: *Resistivity versus T (on a logarithmic scale) measured for a 200 nm $Mg_{0.70}Ti_{0.30}$ /1 nm Pd film in the fully hydrogenated state (in 1 bar H_2). The solid line is a guide for the eyes. From ref. [5].*

by Borsa *et al.* in 2007 [5]. It was found that while the metallic state shows zero transmission and a relatively high and featureless reflection for all compositions, the hydrogenated state has low reflection *combined* with low transmission in the case of $y = 0.8$ and 0.7. This means that in the hydrogenated state the Ti-rich samples display a highly absorbing character, a so-called black state, extending over the entire visible energy range. The absorption decreases with decreasing film thickness, offering the possibility to fine-tune the properties. By analyzing the energy dependence of the absorption coefficient α an absorption edge was found at high energies, typical for MgH_2 or another phase with a similar band gap. On the basis of this it was concluded that an insulating phase (like MgH_2) would have to be present, and this was further supported by electrical resistivity measurements, which pointed to a non-metallic behaviour. As can be seen in figure 3.6 the resistivity increased for decreasing temperature, with a logarithmic dependence in the range 35 K $< T <$ 298 K. The microscopic origin of the peculiar optical and electrical properties remained uncertain, but it was suggested that a step-wise hydrogenation process with initial formation of small conducting TiH_2 areas followed by a surrounding MgH_2-like insulating phase would be part of the explaination.

The optical properties of Mg_yTi_{1-y} with $y = 0.5, 0.75,$ and 0.875 were also investigated theoretically by DFT [17], using both simple ordered and quasi-random structures. From the results it was argued that the optical black state of Mg_yTi_{1-y} is an intrinsic property of a homogeneous bulk hydride, in contrast to the hydrogenation of Mg_2Ni where phase separation into Mg_2NiH_4 and $Mg_2NiH_{0.3}$ grains is responsible for the observed black state.

3.3 XPS parameters

XPS is a widely used technique and the wealth of reported data does sometimes represent a bit of a challenge. Reported binding energies for the same peak position can often vary by several eV, and unfortunately peak fitting parameters are rarely included in published spectra. This section describes published results that were used as comparison with XPS data in this work.

Spectra of pure Mg and Ti and their oxides have been extensively studied over several decades [27, 28, 29, 30]. Mg is easily oxidized, forming both MgO and $Mg(OH)_2$ upon air exposure. The Mg oxide and hydroxide peaks overlap in the Mg 2p spectrum, but can be easily distinguished from the metallic component. In the O 1s spectrum Mg oxide and hydroxide are well separated with about 2 eV. Ti on the other hand forms several oxides, and the overlap and asymmetries in the Ti 2p spectrum have caused some confusion in the literature. In this work we have adapted the fitting approach proposed in a reacent publication by Biesinger *et al.* [30]. Peak positions are listed in table 3.3. The full width at half maximums (FWHM) for the Ti $2p_{3/2}$ and Ti $2p_{1/2}$ peaks acquired at a pass energy 20 eV were found to be 0.69 eV and 0.83 eV, respectively, in the case of Ti metal. For TiO_2 the corresponding peaks were broader, 1 eV and 2 eV, respectively. For the metallic peak an asymmetric peak-shape La(1.1,5,7) was used, where the first two parameters define the spread on either side of a Lorentzian component. The Lorentzian curve is convoluted by a Gaussian with the width specified by the last parameter. For more details about the LA peak shape see ref. [30]. The oxide peaks were fitted with a mixed Gaussian-Lorentzian component GL(67), where the parameter gives the Lorentzian percentage. The exact peak shapes will vary somewhat from spectrometer to spectrometer.

When it comes to hydrides the first report of binding energies and Auger parameter values for MgH_2 came from Friedrichs *et al.* in 2006 [31]. They studied Mg hydride exposed to oxygen and air in a controlled manner, on samples synthesized by high energy ball milling (BM) and gas phase condensation (GPC) methods. They found that the surface was always covered by a thin amorphous oxide and hydroxide layer, thinner for the MgH_2 sample than the unhydrogenated ones. Figure 3.7 shows the development during controlled oxygen and air exposure. The MgH_2

Table 3.3: *Ti $2p_{3/2}$ literature values compiled by Biesinger et al. [30], see original paper for cited references.*

Compound	**Ti $2p_{3/2}$ [eV]**	**Std. dev. [±eV]**	**No. of cit.**	**Mult. splitt. [eV]**	**Std. dev. [±eV]**	**No. of cit.**
Ti	453.86	0.32	8	6.13	0.06	2
TiO	455.34	0.39	8	5.73	0.15	3
Ti_2O_3	457.13	0.35	8	5.60	0.36	3
TiO_2	458.66	0.22	13	5.66	0.08	4

peaks overlapped with oxide and hydroxide peaks and were not assigned individual binding energies. Peak positions are listed in table 3.4. In the state prior to the first oxidation the Auger parameters for BM-Mg and BM-MgH_2 were 1231.2 eV and 1231.8 eV respectivly, assigned to a MgO and a MgH_2 phase, respectively. After air exposure, BM-MgH_2 showed an increase in the Auger parameter to 1230.6 eV due to the formation of $Mg(OH)_x$, while the Auger parameter of BM-Mg stayed constant. BM-MgH_2 and GPC-Mg ended up having the same Auger parameter, due to presence of hydroxide, while BM-Mg showed better resistance to air oxidation. Ti hydrides seem to be somewhat more investigated by XPS [32, 33, 34, 35], and already in 1980 Lamartine *et al.* [36] found a linear relationship between the H/Ti ratio and the shift in the Ti 2p peak position. Typically one sees a 0.6 eV shift to higher E_b for the Ti $2p_{3/2}$ peak in fully hydrogenated TiH_2 compared to metallic Ti.

Mg-Ti samples without hydrogen have been studied by XPS within the framework of improving corrosion resistance of Mg by alloying with nobler metals. In 2002 vapor-deposited samples of composition between 7.6 and 30.2 at.% Ti were investigated by Mitchell *et al.* [1] using high-energy X-ray photoelectron spectroscopy with a Cr Kα source. They found that the final state Auger Parameter (AP) for vapor deposited Mg (Mg 1s + Mg *KLL*) was about 0.1 eV lower than pure Mg, decreasing weakly with increasing Ti content. For the initial state AP this trend was stronger. The final state AP for Ti (Ti 1s + Ti *KLL*) showed the opposite behaviour, with an increase of the final state AP with increasing Ti content. The AP shifts of Ti and Mg were comparable in magnitude. The AP values were used to calculate the charge transfer in the Mg-Ti system, which appeared to be directed from Mg to Ti. It seemed that Ti was better screened in Mg-Ti than in its pure state.

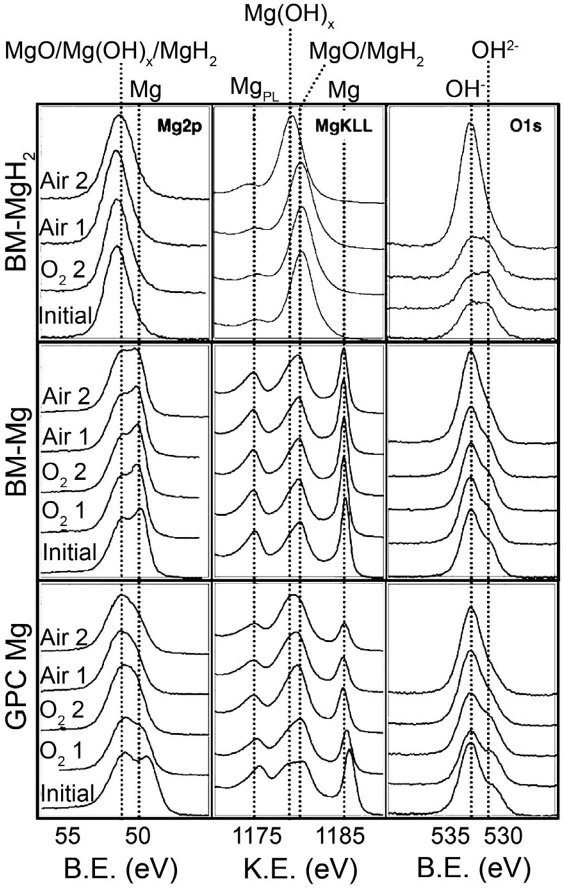

Figure 3.7: *Evolution of photoelectron (Mg2p, O1s) and Auger ($KL_{2,3}L_{2,3}$) peaks upon controlled oxygen and air exposure for the three samples under study: GPC-Mg, BM-Mg and BM-MgH$_2$. Initial, original untreated sample; O$_2$ 1 oxygen dose of about 1 Torr for 2 min; O$_2$ 2, oxygen dose of about 50 Torr for 2 min; Air 1, air exposure for 5 min and Air 2, air exposure for more than 90 min. From ref. [31]*

Table 3.4: *XPS peak positions from ref. [31].*

Peak	BE	Type	BE	Type	BE	Type
Mg 2p	50.1 eV	Metallic	51,2 eV	Oxide/Hydroxide	1185.3 eV	Metallic
Mg *KLL*	1179.2 eV	Hydroxide	1180.1 ev	Oxid		
O 1s	531.4 eV	Oxide	533.2 eV	Hydroxide		

References

[1] T. Mitchell, S. Diplas, P. Tsakiropoulos, J. F. Watts, and J. A. D. Matthew. Study of alloying behaviour in metastable Mg-Ti solid solutions using Auger parameter measurements and charge-transfer calculations. *Philos. Mag. A*, 82(4):841–855, 2002.

[2] P. Vermeulen, P. C. J. Graat, H. J. Wondergem, and P. H. L. Notten. Crystal structures of Mg_yTi_{100-y} thin film alloys in the as-deposited and hydrogenated state. *Int. J. Hydrogen Energy*, 33:5646–5650, 2008.

[3] B. R. Pauw, W. P. Kalisvaart, S. X. Tao, M. T. M. Koper, A. P. J. Jansen, and P. H. L. Notten. Cubic MgH_2 stabilized by alloying with transition metals: A density functional theory study. *Acta Mater*, 56:2948–2954, 2008.

[4] S. Er, D. Tiwari, G. A. de Wijs, and G. Brocks. Tunable Hydrogen Storage in Magnesium - Transition Metal Compounds: First-principle calculations. *Phys. Rev. B*, 79:024105, 2009.

[5] D. M. Borsa, R. Gremaud, A. Baldi, H. Schreuders, J. H. Rector, B. Kooi, P. Vermeulen, P. H. L. Notten, B. Dam, and R. Griessen. Structural, optical and electrical properties of $Mg_yTi_{1-y}H_x$ thin films. *Phys. Rev. B*, 75:205408, 2007.

[6] F. R. de Boer, R. Boom, W. C. M. Mattens, A. R. Miedema, and A. K. Niessen. *Cohesion in metals*. North-Holland, Amsterdam, 1988.

[7] M. Gonzalez-Silveira, R. Gremaud, A. Baldi, H. Schreuders, B. Dam, and R. Griessen. Effect of H-induced microcstructural changes on pressure-optical transmission isotherms for Mg-V thin films. *Int. J. Hydrogen Energy*, 35:6959–6970, 2010.

[8] I. A. M. E. Giebels, J. Isidorsson, and R. Griessen. Highly absorbing black Mg and rare-earth-Mg switchable mirrors. *Phys. Rev. B*, 69:205111, 2004.

[9] M. Di Vece, S. J. M. Zevenhuizen, and J. J. Kelly. Optical switching properties from isotherms of Gd and GdMg hydride mirrors. *Appl. Phys. Lett.*, 81:1213, 2002.

[10] D. G. Nagengast, A. T. M. van Gogh, E. S. Kooij, B. Dam, and R. Griessen. Contrast enhancement of rare-earth switchable mirrors through microscopic shutter effect. *Appl. Phys. Lett.*, 75:2050–2052, 1999.

[11] J. P. Bastide, B. Bonnetot, J. M. Letoffe, and P. Claudy. Polymorphisme de l'hydrure de magnesium sous haute pression. *Mater. Res. Bull.*, 15(12):1779–1787, 1980.

[12] P. Vermeulen, R. A. H. Niessen, and P. H. L. Notten. Hydrogen storage in metastable Mg_yTi_{1-y} thin films. *Electrochem. Commun*, 8:27–32, 2006.

[13] P. Vermeulen, H. J. Wondergem, P. C. J. Graat, D. M. Borsa, H. Schreuders, B. Dam, R. Griessen, and P. H. L. Notten. *In situ* electrochemical XRD study of (de)hydrogenation of Mg_yTi_{100-y} thin films. *J Mater Chem*, 18:3680–3687, 2008.

[14] R. Gremaud, A. Baldi, M. Gonzalez-Silveira, B. Dam, and R. Griessen. Chemical short-range order and lattice deformations in $Mg_yTi_{1-y}H_x$ thin films probed by hydrogenography. *Phys. Rev. B*, 77:144204, 2008.

[15] A. Baldi, R. Gremaud, D. M. Borsa, C. P. Baldè, A. M. J. van der Eerden, G. L. Kruijtzer, P. E. de Jongh, B. Dam, and R. Griessen. Nanoscale composition modulations in $Mg_yTi_{1-y}H_x$ thin film alloys for hydrogen storage. *Int. J. Hydrogen Energy*, 34:1450–1457, 2009.

[16] B. E. Warren, B. L. Averbach, and B. W. Roberts. Atomic size effect in the X-ray scattering by alloys. *J. Appl. Phys.*, 22(12):1493–1496, 1951.

[17] M. J. van Setten, S. Er, G. Brocks, R. A. de Groot, and G. A. de Wijs. First-principle study of the optical properties of $Mg_xTi_{1-x}H_2$. *Phys. Rev. B*, 79(125117), 2009.

[18] S. X. Tao, P. H. L. Notten, R. A. van Santen, and A. P. J. Jansen. DFT studies of hydrogen storage properties of $Mg_{0.75}Ti_{0.25}$. *J. Alloys Compd*, 509:210–216, 2011.

[19] P. H. Mayrhofer, D. Music, and J. M. Schneider. Influence of the Al distribution on the structure, elastic properties, and phase stability of supersturated $Ti_{1-x}Al_xN$. *J. Appl. Phys.*, 100:094906, 2006.

[20] K. Termentzidis and J. Hafner. CO adsorption on a Au/Ni(111) surface alloy - a DFT study. *J. Phys.: Condens. Matter*, 19:246219, 2007.

[21] X. K. Shu, P. Jiang, and J. G. Che. Surface alloying of immiscible metals induced by surface state shifts. *Surf.Sci.*, 545:199–210, 2003.

[22] J. N. Huiberts, R. Griessen, J. H. Rector, R. J. Wijngaarden, J. P. Dekker, D. G. de Groot, and N. J. Koeman. Yttrium and lanthanum hydride films with switchable optical properties. *Nature*, 380:231–234, 1996.

[23] P. van der Sluis, M. Ouwerkerk, and P. A. Duine. Optical switches based on magnesium lanthanide alloy hydrides. *Appl. Phys. Lett.*, 70(25):3356–3358, 1997.

[24] T. J. Richardson, J. L. Slack, R. D. Armitage, R. Kostecki, B. Farangis, and M. D. Rubin. Switchable mirrors based on nickel-magnesium films. *Appl. Phys. Lett.*, 78(20):3047–3049, 2001.

[25] W. Lohstroh, R. J. Westerwaal, B. Noheda, S. Enache, I. A. M. E. Giebels, B. Dam, and R. Griessen. Self-organized layered hydrogenation in black Mg_2NiH_x switchable mirrors. *Phys. Rev. Lett.*, 93(19):197404, 2004.

[26] D. M. Borsa, A. Baldi, M. Pasturel, H. Schreuders, B. Dam, R. Griessen, P. Vermeulen, and P. H. L. Notten. Mg-Ti-H thin films for smart solar collectors. *Appl. Phys. Lett.*, 88:241910, 2006.

[27] J. C. Fuggle. XPS, UPS and XAES studies of oxygen adsorption on polycrystalline Mg at 100 and 300 K. *Surf. Sci.*, 69:581–608, 1977.

[28] P. M. Th. M. Van Attekum and J. M. Trooster. vet ikke. *J. Phys. F.*, 9(x):2287, 1979.

[29] M. Santamaria, F. Di Quarto, and P. Zanna, S. Marcus. Initial surface film on magnesium metal: A characterization by X-ray photoelectron spectroscopy (XPS) and photocurrent spectroscopy (PCS). *Electrochim. Acta*, 53:1314–1324, 2007.

[30] M. C. Biesinger, L. W. M. Lau, A. R. Gerson, and R. St. C. Smart. Resolving surface chemical states in XPS analysis of first row transition metals, oxides and hydroxides: Sc, Ti, V, Cu and Zn. *Appl. Surf. Sci.*, 257:887–898, 2010.

[31] O. Friedrichs, J. C. Sánchez-López, C. López-Cartes, M. Dornheim, T. Klassen, and A. Fernández. Chemical and microstructural study of the oxygen passivation behaviour of nanocrystalline Mg and MgH_2. *Appl. Surf. Sci*, 252:2334–2345, 2006.

[32] B. Lesiak, J. Zemek, P. Jiricek, and M. Čerňanský. Elastic electron backscattering from Ti: grain size effect. *Surf. Interface Anal.*, 36:816–819, 2004.

[33] W. Lisowski, E. G. Keim, A. H. J. van der Berg, and M. A. Smithers. Structural and chemical characterisation of titanium deuteride films covered by nanoscale evaporated palladium layers. *anal. Bioanal. Chem.*, 385:700–707, 2006.

[34] X. D. Kang, P. Wang, and H. M. Cheng. Improving Hydrogen Storage Performance of $NaAlH_4$ by Novel Two-Step Milling Method. *J. Phys. Chem. C*, 111:4879–4884, 2007.

[35] L. P. Ma, X. D. Kang, H. B. Dai, Z. Z. Liang, Y. Fang, P. J. Wang, P. Wang, and H. M. Cheng. Superior catalytic effect of TiF_3 over $TiCl_3$ in improving the hydrogen sorption kinetics of MgH_2: Catalytic role of fluorine anion. *Acta Mater.*, 57:2250–2258, 2009.

[36] B. C. Lamartine, T. W. Haas, and J. S. Solomon. Characterization of TiH_x and $TiD_{0.9}$ surfaces: AES, ELS, SIMS and XPS studies. *Appl. Surf. Sci.*, 4:537–555, 1980.

Chapter 4

Overview of results

The scientific results of this Ph.D. work are presented in the six papers appended to this thesis. A brief summary of each paper is given below, followed by some overall conclusions.

Paper I

X-ray photoelectron spectroscopy study of MgH$_2$ thin films grown by reactive sputtering

In the first paper a MgH$_2$ thin film grown directly by reactive sputtering in H$_2$ gas was studied by XPS. Three samples from the same film were measured at different times after exposure to air, using Ar$^+$ sputtering to investigate the indepth compositional variations. The paper discusses the difficulties of obtaining reliable peak fitting, owing to the close overlap of the Mg peaks from MgH$_2$, MgO and Mg(OH)$_2$ and the possible effect of differential sample charging. In this particular work the issue of peak fitting was avoided by combining the data from the Mg 2p and O 1s spectra in order to quantify the data. In other words, the O 1s spectrum was used to work out the portion of MgO and Mg(OH)$_2$ in the non-metallic part of the Mg 2p spectrum. Thus the remaining peak area could be assigned to MgH$_2$. The compositional depth profiles showed a thin layer of Mg(OH)$_2$ growing on the surface of the film, and a surprisingly high amount of MgO throughout the sample. The amount of MgH$_2$ did never exceed 30 at. %, which was surprising given earlier reports of increased resistance against oxidation for similar samples. However, in this work the possible reduction of hydrides (and oxides) caused by the Ar$^+$ sputtering, which was later presented in paper V, was not considered.

Paper II

Density functional calculations of Ti nano-clusters in the meta-stable Mg-Ti system

In this work DFT calculations were done for $\mathrm{Mg}_{100-y}\mathrm{Ti}_y$ supercells of compositions $1.56 \leq y \leq 98.44$, with emphasis on the Mg rich side. Two models were compared: A nano-cluster (NC) model where Ti was arranged in small clusters within the Mg matrix and a quasi-random (QR) model where Ti was distributed randomly. Although the structural parameters did not differ much for the two models, the mixing enthalpy per Ti atom was lowered by up to $\sim$0.5 eV when Ti was arranged in nano-clusters. The mixing enthalpy is the cohesive energy of the elements in the model system relative to that in the standard states. The degree of clustering was quantified in terms of the chemical short range order parameter s and the effect of cluster size was investigated by comparing models constructed with different s values. The mixing enthalpy appeared to reach a minimum after which further growth made little difference, indicating that the phenomenon of nano-scale clustering has to be understood separately from the phase separation occurring at larger scale in an equilibrium process. Several reports of experimental structural parameters are available in the literature, with great variations among them and poor correspondence with Vegard's law. In our paper we suggested that this is due to the presence of Ti nano-clusters, and that different synthesis methods would cause variations in the size and shape of the clusters. Local density of states (DOS) calculations revealed how segregated Ti was able to form a local environment resembling pure Ti, while Bader analysis was performed to study the charge distribution between Mg and Ti. The charge transfer from Mg towards Ti was substantial, but could be minimized by the formation of Ti nano-clusters. It was found that a very limited amount of Ti nearest-neighbors is sufficient for Ti to experience an imitation of the elemental state, reducing the driving force for further nucleation.

Paper III

Combined XPS and first principle study of meta-stable Mg-Ti thin films

During the work presented in paper II it became clear that close to the Fermi level the density of states (DOS) was distinctly different for the QR and the NC model. This inspired a direct comparison with the XPS valence spectrum obtained from a thin film sample of composition $\mathrm{Mg}_{80}\mathrm{Ti}_{20}$. The experimental spectrum showed most resemblance to the DOS calculated for the NC model, further supporting the idea of Ti nano-clusters being present in real samples.

Paper IV

Hydrogen induced stabilization of meta-stable Mg-Ti

This paper was inspired by initial XPS measurements, which were later analyzed in detail and presented in paper V. A DFT study of the hydrogenation process of $Mg_{81.25}Ti_{18.75}$ was conducted by gradually introducing H to the interstitial sites in the metallic crystal structure. Substantial lowering of the mixing enthalpy of the system was found upon introducing H to octahedral sites with one or more Ti atoms as nearest neighbors. Contrary to prior assumptions in the literature, the sites at the interface between Mg and Ti were preferred over the sites inside the Ti nanoclusters. However, both the sites at the interface and inside the Ti clusters were found to be very stable, with hydrogenation energies down to -115 kJ/(mol H_2), likely to keep a certain amount of H trapped in the system even after hydrogen unloading was attempted. The hydrogen content in the DFT model was increased gradually according to the calculated relative stabilities for H on the different sites, starting with the ones at the Mg-Ti interface. It was found that with respect to the mixing enthalpy, the Mg-Ti-H system changes from meta-stable to stable for hydrogen contents above 0.07 H per metal. The results from this study helped explain why the reversibility of Mg-Ti thin films, which are initially meta-stable, can be preserved over many cycles of loading and unloading of hydrogen.

Paper V

Meta-stable Mg-Ti-H thin films investigated by X-ray photoelectron spectroscopy

In this paper the major part of the XPS work is compiled and presented. A large number of measurements were carried out on a selection of Mg and Mg-Ti samples, with and without H. The experiments were categorized in two main groups: In the *over-night exposure* (ON) experiments the measured sample was left in position in the XPS analysis chamber for about 24 hrs before the same measurement was repeated. Magnesium is highly reactive to oxygen, which means that it will oxidize even in UHV. Thus the results from the ON experiment show the changes in spectra upon gentle oxidation, comprising data from Mg, Mg with H and Mg-Ti with H. A comparative *depth profile* (DP) experiment was performed for Mg-Ti with and without H. For each sample measurements were done at intervals of 5 minutes of Ar^+ sputtering at 0.5 kV, starting with 5 minutes and ending with 30 minutes total sputtering time. The data set as a whole revealed subtle variations that made consistent peak fitting hard to obtain, highlighting the possible dangers of drawing conclusions based on a single measurement or sample. Factors complicating the picture in this particular case included possible sample charging effects due to the different electric properties of the different phases (metallic vs. semi-conducting or insulating) and the high affinity for oxygen of both Mg and Ti. The oxidation issue was later discussed further in paper VI. Also, the surface of the thin film samples was covered with a 1.5 nm or 5 nm layer of Pd, to promote hydrogen uptake and/or to protect from oxidation. This layer had to be sputtered away using Ar^+ sputtering, which resulted in reductions of both oxides, hydroxides and hydrides. The main finding in paper V, however, was a new peak (I^H) in the Mg *KLL* spectra from the Mg-Ti-H samples, located between the metallic and the oxide component. The shift in the Mg 2p-*KLL* Auger parameter for I^H indicated a decrease in the electron hole screening ability compared to metallic Mg, but not as much as for MgO or MgH_2 which are both semi-conducting or insulating. This information was compared to results from Bader analysis obtained in connection to paper III, which lead to the conclusion that the I^H peak was consistent with hydrogen being trapped on especially stable interstitial sites at the interface between Mg and the Ti nano-clusters.

Paper VI

High energy XPS study of $Mg_{80}Ti_{20}$ thin films with and without hydrogen

High energy XPS was carried out on two $Mg_{80}Ti_{20}$ thin film samples, one with and one without H. From this the 1s-*KLL* Auger parameters of both Mg and Ti could be obtained. The most interesting result, however, was a sheer bonus, discovered when taking a closer look at rapidly acquired Mg *KLL* spectra used to monitor the Ar^+ sputter removal of Pd. It turned out that immediately after Pd removal no trace of oxidation was found in the Mg *KLL* spectrum. Instead, a peak was found in the high kinetic energy (E_K) shoulder of the metallic Mg component. This peak disappeared and oxidation progressed rapidly in the time it took to acquire high resolution spectra, as if it was the phase causing the high E_K peak that was oxidized. High resolution spectra were acquired for Mg 1s, Mg *KLL*, Ti 1s and Ti *KLL* after 55 minutes Ar^+ sputtering of the Mg-Ti sample (MgTi-55) and after 45 and 65 minutes Ar^+ sputtering of the Mg-Ti-H sample (MgTiH-45 and MgTiH-65). What made it especially interesting was that the high E_K peak was found in both the MgTi-55 and the MgTiH-65 spectra, but *not* in the MgTiH-45 spectrum. The Mg-Ti-H sample did, however, seem to be layered, with a zone affected by the Pd layer extending somewhat into the film, a hydrogenated zone in the middle and a metallic zone deeper in the sample where the hydrogenation had not reached. The MgTiH-45 measurement was mainly from the hydrogenated zone, while measurement MgTiH-65 probed both the middle hydrogenated zone and the metallic zone beneath it. Previously, no significant effect of the introduction of Ti had been found in Mg spectra obtained by XPS, which was somewhat puzzling considering the magnitude of the charge transfer predicted by DFT. Bearing the results from paper IV in mind it was considered whether oxygen could play a similar role as H in shielding Ti from the charge transfer from Mg. Using DFT it was found that introducing O to octahedral sites in the crystal structure dramatically lowered the mixing enthalpy of the system. In the case of oxygen the sites inside the clusters were preferred, with the energy gain decreasing with decreasing number of Ti nearest neighbors. In this context the high E_K peak in the Mg *KLL* spectrum could be explained by the interaction with Ti, which would disappear as soon as the sites at the interface between Mg and the Ti nano-clusters were filled with hydrogen. In the hydrogenated sample prior to oxygen exposure these sites would already be filled by H, possibly explaining why the high E_K peak was not seen in the Mg *KLL* spectrum of the hydrogenated material. What happens to the hydrogenated sample upon oxygen exposure, for instance if H at the interface between Ti and Mg would be replaced by O, was not treated by DFT at this stage.

Overall conclusions

As a whole the present project has demonstrated how experimental and computational techniques can provide each other with mutual input and inspiration in a diverse attempt to improve the understanding of a material system. The process was prodded forward by the new insights or questions obtained by one technique or the other, reaching beyond the cases where the type of results acquired from both methods were directly comparable.

Above all the project has given a taste of the complexity involved when moving materials tailoring down to the nano-scale. It was shown how segregation of fewer than ten Ti atoms in a Mg matrix can have a significant effect on the stability of the system, altering the solid-solubility limits for immiscible elements. The cause of the effect had to be traced down to electron interactions, with the behavior of H and O as ”electron shields” on the Mg-Ti interface as a very tangible manifestation. Further it was shown how mixing Mg and Ti results in hydrogenation properties that differ significantly from what one would expect considering the separate behaviour of Mg and Ti. The formation of Ti nano-clusters introduced new preferred sites for H at the interface between the Ti nano-clusters and the Mg matrix. Such detailed atomistic knowledge can open up new possibilities for manipulation. As an example, if the size and/or shape of the nano-clusters could be controlled during synthesis, this could allow for fine-tuning of the optical and electrical properties of Mg-Ti-H and similar materials systems. In a wider perspective, understanding the interaction between immiscible elements are becoming more and more relevant as devices are continuously scaled down. Reliable nano-scale diffusion barriers and interconnections have to be developed, which often involves the use of immiscible elements [1, 2]. Surface alloying of immiscible alloys is also a topic in both coating technology and catalysis [3]. Thus the high affinity for both H and O at the interface between Mg and Ti may turn out to be relevant for a large number of other systems where immiscible elements are being used in the future.

References

[1] G. Ouyang, C. X. Wang, and G. W. Yang. Anomalous interfacial diffusion in immiscible metallic multilayers: a size dependent kinetic approach. *Appl. Phys. Lett.*, 86:171914, 2005.

[2] B. Girault, P. Villain, E. Le Bourhis, P. Goudeau, and P. O. Renault. X-ray diffraction analysis of the structure and residual stresses of W/Cu multilayers. *Surf. Coat. Tech.*, 201:4372–4376, 2006.

[3] X. K. Shu, P. Jiang, and J. G. Che. Surface alloying of immiscible metals induced by surface state shifts. *Surf.Sci.*, 545:199–210, 2003.

Paper I

X-ray photoelectron spectroscopy study of MgH_2 thin films grown by reactive sputtering.

I.J.T. Jensen, S. Diplas, O. M. Løvvik, J. Watts, S. Hinder, H. Schreuders and B. Dam,

Surface and interface analysis **42**, 1140-1143 (2010)

Paper II

Density functional calculations of Ti nano-clusters in the meta-stable Mg-Ti system.

I.J.T. Jensen, S. Diplas, and O. M. Løvvik,

Physical review B **82**, 174121 (2010)

PHYSICAL REVIEW B **82**, 174121 (2010)

Density functional calculations of Ti nanoclusters in the metastable Mg-Ti system

I. J. T. Jensen,[1,*] S. Diplas,[2,3] and O. M. Løvvik[1,2]
[1]*Department of Physics, University of Oslo, P.O. Box 1048, Blindern, 0316 Oslo, Norway*
[2]*SINTEF Materials and Chemistry, P.O. Box 124, Blindern, 0314 Oslo, Norway*
[3]*Center for Materials Science and Nanotechnology, P.O. Box 1126, Blindern, 0318 Oslo, Norway*

(Received 14 January 2010; revised manuscript received 14 July 2010; published 19 November 2010)

Mg-Ti-H thin films exhibit interesting optical and electrical properties, offering a wide range of possible applications from coatings on solar collectors and smart windows to optical hydrogen sensors and semiconductor devices. However, Ti is known to be immiscible in Mg, and the microstructure of Mg-Ti thin films is not fully understood. In this work density functional theory calculations were used to investigate the $Mg_{100-y}Ti_y$ system with $1.56 \leq y \leq 98.44$. The crystal structure, mixing enthalpy, and electronic structure were compared for two different distributions of Ti: quasirandom and segregated. It was found that although the crystal structures did not differ significantly, the formation enthalpy per Ti atom was lowered by up to ~0.5 eV when Ti was arranged in nanoclusters. This gives support to previous experimental findings of chemical short-range order in Mg-Ti thin films [R. Gremaud *et al.*, Phys. Rev. B **77**, 144204 (2008)]. As a consequence of the decrease in the mixing enthalpy upon clustering the occurrence of short-range chemical order in all reported metastable Mg-Ti alloys with extended solubility is proposed. Further inquires into the influence of the size of the clusters revealed that the mixing enthalpy reaches a minimum after which further growth makes little difference, indicating that the phenomenon of nanoscale clustering must be understood separately from the larger scale phase separation occurring in an equilibrium process. The relaxed crystal structures were compared to experimental values from several sources and lattice-parameter variations as well as deviations from Vegard's law were discussed. Dependence of the size and shape of the nanoclusters on synthesis method is offered as an explanation for the large variation among the experimental lattice parameters. Local density of states calculations illustrated how segregated Ti forms a local environment resembling pure Ti while it was necessary to perform Bader analysis in order to obtain the correct picture of the charge transfer between Mg and Ti. Randomly distributed Ti atoms affect the charge distribution severely and the further the Ti atoms are apart the larger is the charge transfer from Mg. It was shown that a very limited amount of Ti nearest neighbors is sufficient for Ti to experience an imitation of elemental state, removing the driving force for further nucleation.

DOI: 10.1103/PhysRevB.82.174121 PACS number(s): 61.66.Dk, 71.20.Be

I. INTRODUCTION

With the discovery of switchable mirrors by Huiberts *et al.* in 1996 (Ref. 1) a new group of materials with remarkable optical properties has emerged. It was found that upon hydrogenation La and Y thin films go through drastic optical changes, from reflecting in the metallic state to transparent in the hydride state. Later this has been seen for several other compounds as well,[2–5] including the Mg-Ti-H system.[6]

The tunable electrical and optical properties of Mg-based thin-film hydrides make them interesting for a variety of applications. One example is the possible use of thin-film hydrides as switchable absorbers in solar collectors.[6] Another example is switchable coatings for smart windows, where there is a potential for significant reduction in energy losses through building windows. The band gap exhibited in many hydrides also represents possibilities in semiconductor electronics, for instance in *p-n* junction-based electronic devices such as solar cells.[7] Furthermore the hydride thin films have an obvious application as optical hydrogen sensors.[8] The optical changes related to hydride formation can also be utilized in the search for suitable new hydrogen-storage materials. Employing the hydrogenography technique[9] a compositional gradient film can be used to map the formation enthalpy of thousands of alloy compositions in a single experiment.

Mg is a particularly interesting hydrogen-storage material due to its low weight with a theoretical hydrogen-storage capacity of 7.7 wt % H. Unfortunately the high thermal stability and slow kinetics make it unsuited for practical use. Extensive effort has been put into circumventing these problems[10–14] and in 2005 excellent hydrogen-storage capacity was reported for Mg-Ti-H thin films of different compositions by Niessen *et al.*[15] The geometric structure of such compounds is not obvious, neither with nor without H, as the solubility of Ti in Mg is known to be very limited. Further investigations by Rutherford backscattering spectrometry, x-ray diffraction (XRD) and transmission-electron microscopy suggested a coherent structure; the samples were found to be single phase crystalline from before hydrogen absorption throughout to after hydrogen desorption.[16] An *in situ* electrochemical XRD study of (de)hydrogenation of thin films by Vermeulen *et al.*[17] further supported the hypothesis of only one phase present in the samples. They concluded that if Ti is segregated from Mg it must be in small particles of sizes below the XRD detectable range. Indeed, evidence for such chemical short-range order was found from simulation of optical isotherms obtained by the hydrogenography technique in a study by Gremaud *et al.*[18] in 2008. Recently this was further verified by a combination of x-ray diffraction and extended x-ray absorption fine-structure spectroscopy.[19]

©2010 The American Physical Society

Vapor deposited $Mg_{100-y}Ti_y$ samples with y up to 25.3 have been investigated by x-ray photoelectron spectroscopy by Mitchell *et al.*[20] Auger parameter measurements and charge-transfer calculations indicated charge transfer from Mg to Ti. Experimental lattice parameters were reported for the compositions $1.7 \leq y \leq 21.8$. Vermeulen *et al.*[21] also determined the lattice parameters of similar samples with $y = 10$, 20, and 30. dc/rf sputtered samples were measured with and without hydrogen using *in situ* x-ray diffraction. In all above cases the as deposited samples had a hexagonal-closed-packed structure similar to the structure of pure Mg and Ti. For the hydrides, however, a face-centered-cubic symmetry was found for the hydrogenated $Mg_{70}Ti_{30}$ and $Mg_{80}Ti_{20}$ compounds while the unit cell of hydrogenated $Mg_{90}Ti_{10}$ was body-centered tetragonal.

Due to the immiscibility of Ti in Mg there is limited density functional theory (DFT) work done on this system. Recently the *hydride* phase of Mg-Ti thin films was investigated by DFT calculations by Pauw *et al.*[22] and Er *et al.*[23] It was found that above a transition point at 20 at. % Ti the Mg-Ti hydride changes from the body-centered-tetragonal structure of pure MgH_2 into a face-centered-cubic structure similar to that of TiH_2, consistent with the experimental findings cited above.[21]

In the present work a modeling study of the Mg-Ti alloy system is carried out using DFT. It is investigated how different arrangements of Ti in Mg influence the total energy and the structural parameters. Details of the calculations are described in Sec. II. Results are presented in Sec. III with focus on formation enthalpies and relaxed crystal structures in the first part and electronic structure in the second part.

II. COMPUTATIONAL METHODS

DFT calculations were performed using the Vienna *ab initio* simulation package (VASP).[24,25] The Kohn-Sham equations were solved using a basis of projector augmented wave functions[26] with a plane-wave energy cut-off of 350 eV. The Perdew-Burke-Ernzerhof 96 generalized gradient approximation was used for the electron exchange-correlation functional.[27] The criterion for electronic convergence was a change in the total energy less than 10^{-5} eV.

Calculations were done for $Mg_{100-y}Ti_y$ with compositions $1.56 \leq y \leq 98.44$. The compositions with $y > 50$ were mirrored versions of the corresponding compositions with $y < 50$. Parallel calculations were performed for Ti distributed both quasirandomly and arranged in nanoclusters. The standard hexagonal structure of Mg was used as a starting point. For most calculations a $4 \times 4 \times 2$ Mg unit cell was used, containing 64 atoms. In the quasirandom calculations the Ti atoms were distributed in the 64 atom cell at random. The number of Ti atoms in the first coordination sphere of Ti $N_{\text{Ti-Ti}}$ ranged from 0 when $y = 1.56$ to <2 for $y = 0.25$. Most of the models of segregated Ti were constructed by using planes of four Ti atoms stacked together in the a direction while a more quadratic shape was used for the composition with $y = 25$. These first segregated models were labeled *original*. Figures showing segregated and quasirandom distributions can be found in Sec. III. There are many ways to construct segregated clusters and calculations were also performed for certain *alternative* nanoclusters of Ti, as will be explained later. In the segregated case it was necessary to use a $4 \times 4 \times 3$ Mg unit cell containing 96 atoms for the compositions with 25 at. % Ti. This was done in order to avoid unphysical configurations such as slabs or sheets of Ti. A $5 \times 5 \times 7$ Gamma sampling of k points was used to model the Brillouin zone for the cell containing 64 atoms and a $5 \times 5 \times 5$ sampling was used for the cell containing 96 atoms.

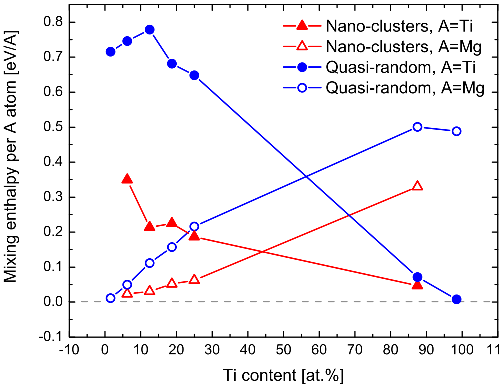

FIG. 1. (Color online) Calculated mixing enthalpy per A atom ($A = \text{Ti}, \text{Mg}$), showing the difference between quasirandom and nanocluster distributions. Lines are included as guides to the eye.

Structural optimizations were performed with volume, lattice parameters, and atom positions allowed to change simultaneously. The break condition for the relaxation loop was set to forces < -0.05 eV/Å. The mixing enthalpy of the alloys was calculated as follows:

$$\Delta H_f = E_{Mg_{100-y}Ti_y} - (100 - y)E_{Mg} - yE_{Ti}, \qquad (1)$$

where $E_{Mg_{100-y}Ti_y}$, E_{Mg}, and E_{Ti} are the calculated energies of alloy, pure Mg, and pure Ti, respectively. In this work the mixing enthalpy *per* Ti *atom* was used for comparisons between the different compositions. Isosurface plots were generated with the VASPVIEW program.[28]

III. RESULTS AND DISCUSSION

A. Structure and mixing enthalpy

The mixing enthalpies were calculated for both the quasirandom and the nanocluster case. Figure 1 reveals that on the Mg-rich side of the scale the formation enthalpy per Ti atom is, in fact, systematically lowered by as much as ~0.5 eV when Ti is arranged in nanoclusters. The availability of data for comparison appears to be rather limited. In the work of Rowlands *et al.*[29] the total energy per atom was calculated as a function of short-range order for $Cu_{50}Zn_{50}$ using a charge self-consistent Korringa-Kohn-Rostoker nonlocal coherent-potential approximation method. For the *whole* range from ideal ordering to ideal clustering the change in energy was in that case only $\sim$0.03 eV with ordering being more stable. Here one should note that Cu and Zn are not immiscible like Mg and Ti.

The substantial gain in energy upon segregation supports the findings of chemical short-range order presented in the work of Gremaud *et al.*[18] and Baldi *et al.*[19] This is also in agreement with the general tendency in *equilibrium* thermodynamics according to which phase separation is more favorable than mixing for Ti and Mg. Nevertheless it is worth contemplating the implications of the calculated results. In its most simplified representation the early stages of precipitation can be thought of as a battle of surface tension against enthalpy. From our calculations, where even segregation of just a handful of Ti atoms results in a significant reduction in the total mixing enthalpy, it becomes clear that the surface tension comes up short already from the beginning. In the literature nucleation and surface tension in condensed-matter physics are treated and understood mainly at a phenomenological level. Although models have been proposed to deal with some of these aspects from first principles,[29,30] a comprehensive understanding at the level of electrons and atomic nuclei seems yet to be established. There appears to be no previous reported atomistic studies of Ti clusters of this scale. In the following the influence of size and shape of the clusters will be investigated in order to shed more light on the nature of this nanoscale precipitation.

As a first consequence of the calculated gain in energy we can propose that short-range chemical order occurs in all reported Mg-Ti samples with extended solubility.[20,31,32] An inherent tendency for Ti clustering in the Mg-Ti system can for instance help explaining the lack of success in obtaining significant improvements in the overall corrosion behavior of Mg-Ti PVD alloys. Ti has a more positive corrosion potential compared to Mg and its presence as a solute in a Mg matrix is expected to ennoble the alloy. However, the presence of Ti nanoclusters and subsequent galvanic phenomena at the nanoscale provide a good explanation for the difficulties in producing reliable corrosion resistant Mg-Ti alloys.

To explore the benefit of segregation of Ti atoms more thoroughly, calculations were performed for a variety of alternative nanoclusters. In order to analyze differences in formation enthalpy the average number of Ti in the first coordination sphere around a Ti atom $N_{\text{Ti-Ti}}$ was calculated, see Table I. The first coordination sphere was defined to contain the 12 nearest-neighbor atoms, giving $N=12$. For 6.25 at. % Ti calculations of a more symmetric and more close-packed Ti cluster resulted in a lowering of the mixing enthalpy per Ti atom by 0.08 eV. For 25 at. % Ti on the other hand, the mixing enthalpy per Ti atom differs by less than a tenth of this value, even though the relative difference in $N_{\text{Ti-Ti}}$ between the two compositions was not correspondingly large. However, the shape of the cluster was fundamentally altered in the case of 6.25 at. % Ti causing a change in $N_{\text{Ti-Ti}}$ for *all* the Ti atoms while for the larger cluster in the 25 at. % Ti composition the changes mainly involved atoms close to the Ti-Mg interface, leaving Ti atoms in the center of the particle unchanged. Taking a systematic approach the original cluster of the 12.5 at. % Ti composition was split into two equal parts and separated in the *ab* plane. The new model was labeled *two parts*. Figure 2 shows the first three models for the 12.5 at. % Ti composition. As can be seen in Table I the splitting of the cluster in two halves causes the mixing enthalpy to increase with 0.13 eV. Hence higher $N_{\text{Ti-Ti}}$ values are found to give a lower value for the mixing enthalpy but as seen above the effect appears to decline with increasing cluster size. Figure 3 shows the mixing enthalpy as a function of s for a number of different compositions and cluster configurations, see Table I for details. Rather than approach-

TABLE I. Average number of Ti atoms on nearest-neighbor sites around Ti $N_{\text{Ti-Ti}}$ and corresponding values for the mixing enthalpy per Ti atom. The unit-cell name gives the number of Mg and Ti atoms. Original nanocluster models used in Fig. 5 in bold. Experimental values (Ref. 18) in *italic*.

Composition	Unit cell	$N_{\text{Ti-Ti}}$	s	Mixing enthalpy per Ti (eV/Ti)
$Mg_{93.75}Ti_{6.25}$	**Mg63Ti1**	2.500	0.16	0.349
	Mg63Ti1	3.000	0.20	0.273
$Mg_{87.50}Ti_{12.50}$	**Mg56Ti8**	4.500	0.29	0.214
	Mg56Ti8-(2parts)	3.000	0.14	0.345
	Mg189Ti27	6.666	0.49	0.190
	Mg252Ti36	5.666	0.40	0.246
	Mg252Ti36	7.030	0.53	0.184
$Mg_{81.25}Ti_{18.75}$	**Mg52Ti12**	5.167	0.30	0.225
$Mg_{80.00}Ti_{20.00}$		*4.32*	*0.20*	
$Mg_{75.00}Ti_{25.00}$		*5.70*	*0.30*	
$Mg_{75.00}Ti_{25.00}$	**Mg72Ti24**	6.708	0.41	0.187
	Mg72Ti24	5.917	0.32	0.194
$Mg_{70.00}Ti_{30.00}$		*6.46*	*0.34*	
$Mg_{65.00}Ti_{35.00}$		*6.94*	*0.35*	
$Mg_{61.00}Ti_{39.00}$		*7.32*	*0.36*	
$Mg_{12.50}Ti_{87.50}$	**Mg8Ti56**	4.500[a]	0.29[a]	0.330

[a] $N_{\text{Mg-Mg}}$.

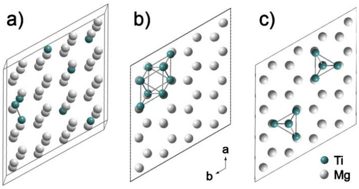

FIG. 2. (Color online) Different distributions of Ti in a unit cell containing 12.5 at. % Ti: (a) quasirandom, (b) original nanocluster, and (c) original nanocluster divided in two parts. Dark and light balls represent Ti and Mg atoms.

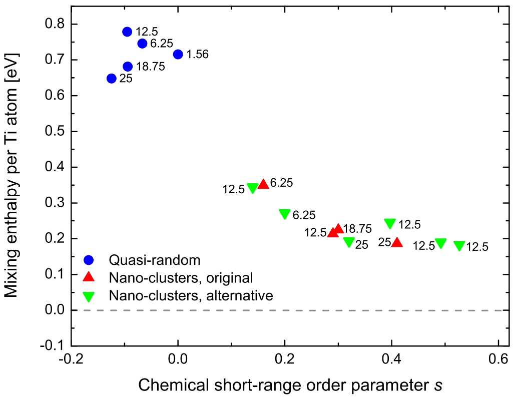

FIG. 3. (Color online) Mixing enthalpy per Ti atom as a function of chemical short-range order parameter s. The labels indicate composition in at. % Ti.

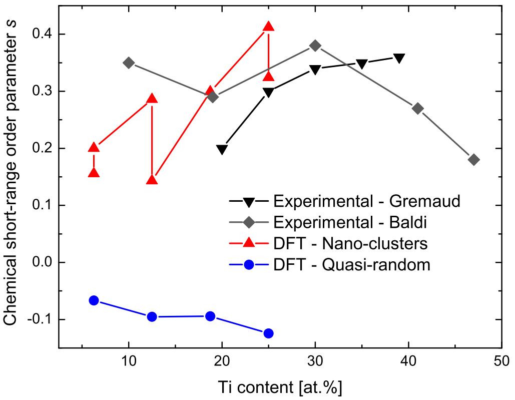

FIG. 4. (Color online) The chemical short-range order parameter s defined in [Eq. (2)] as a function of composition. Our model values are compared to experimental results by Gremaud (Ref. 18) and Baldi (Ref. 19).

ing 0 eV for increasing cluster size, the mixing enthalpy appears to reach a minimum somewhere between 0.2 and 0.1 eV. Obviously, at some point the surface area of a (spherical) cluster becomes small compared to the volume. The fact that this serves to attenuate the gain in energy upon further segregation, rather than to speed up the process comes as a bit of a surprise. Normally the free energy of formation of a nucleus as a function of its radius will have a concave shape, resulting in a critical radius above which growth of a nucleus lowers the free energy. Below the critical radius the cost of creating the interface, the surface tension, outweighs the gain in bulk free energy and hinders nucleation. In the Mg-Ti system, however, the situation appears to be opposite. The Mg-Ti interaction seems to favor segregation, making the interface between cluster and matrix a driving force *for* nucleation rather than against. We will return to this when addressing the electronic structure of the system in Sec. III B.

Table I also gives $N_{\text{Ti-Ti}}$ values presented in the work of Gremaud *et al.*[18] Their chemical short-range order parameters s was transformed into $N_{\text{Ti-Ti}}$ by the equation[33]

$$s = 1 - \frac{N - N_{\text{Ti-Ti}}}{N(1-y)}, \tag{2}$$

where $(1-y)$ is the atomic fraction of Mg and N is the total number of atoms in the first coordination sphere.

Figure 4 shows s as a function of composition for both calculated and experimental data. The nanocluster models constructed in this work are found to correspond rather well to the level of chemical short-range order found experimentally. In the data by Gremaud *et al.*[18] the slope of the chemical short-range order is, in fact, found to decrease with Ti content, although approaching a somewhat higher s value than predicted in Fig. 3. However, the *decrease* in s value observed by Baldi *et al.*[19] is more curious. From our modeling results it is evident that segregation of Ti will only represent a gain in energy up to a certain point but there is nothing to indicate such a decrease in s. This suggests that the trend in the chemical short-range order found by Baldi *et al.* is a result of a trade off between the lowering of energy by segregation of Ti and the kinetic restrictions of the system. As no overall phase separation is found experimentally, one can assume that solid-state diffusion of Ti at ambient conditions is negligible. Thus the window of segregation will be related to the sputtering process itself. Thus the decrease in s value with composition found by Baldi *et al.* can possibly be explained by the fact that the sputtering rate was increased with the amount of Ti, leaving the Ti clusters less time to grow.

Lattice parameters were calculated for quasirandom and segregated distributions with different Ti contents. Figure 5 shows the deviations from Vegard's law. Some of the calculated unit cells deviate slightly from the original hexagonal symmetry, all with differences between the a and b axes less than 0.01 Å and angular deviation within 1° of perfect hexagonal shapes. This is within the uncertainty limit of the method[38] and can be considered hexagonal. The limited size of the model unit cell will in some cases cause artificial symmetry breaks, yielding different a and b axes. Therefore, an average of the a and b axes is used in the figure. The plots in Fig. 5 reveal a convex deviation from Vegard's law. Also included in the figures are several experimental values reported in the literature. There appears to be considerable variations even among real samples with comparable content of Ti.

The differences in s values for the two experiments in Fig. 4 illustrate how the size (and probably shape) of the nanoclusters is likely to be affected by the method of synthesis. This realization may very well be the key to understanding the diverging experimental lattice parameters presented in Fig. 5, where samples were prepared both by dc/rf sputtering,[21] physical vapor deposition,[20] and different variations in ball milling.[31,32,37] Different techniques leading to different Ti distributions may, in turn, lead to differences in lattice parameters. Another feature in Fig. 5 is the deviation

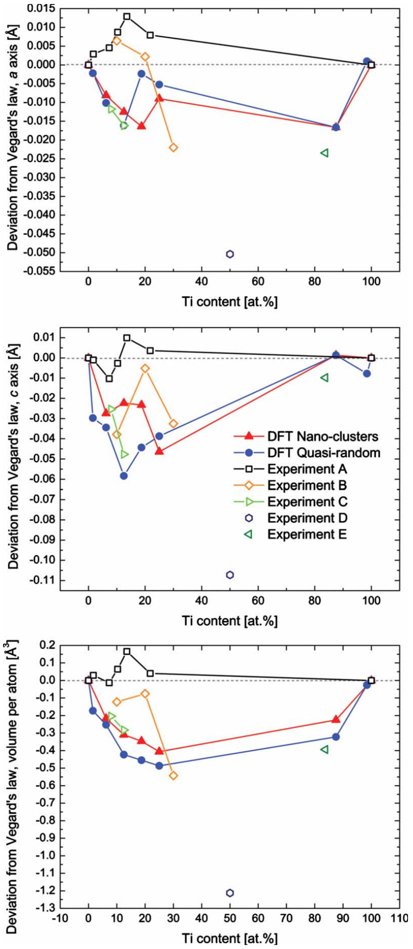

FIG. 5. (Color online) Calculated and experimental deviation from Vegard's law: a axis (top), c axis (middle), and volume (bottom). Experimental values for the pure elements were taken from the Inorganic Crystal Structure Database (ICSD) (Ref. 34): a $=3.208$ Å and $c=5.211$ Å for Mg (Ref. 35) and $a=2.951$ Å and $c=4.684$ Å for Ti (Ref. 36) Experiment A, B, C, D, and E from Mitchell (Ref. 20), Vermeulen (Ref. 21), Liang (Ref. 31), Rousselot (Ref. 32), and Wilkes (Ref. 37), respectively. Lines are included as guides to the eye.

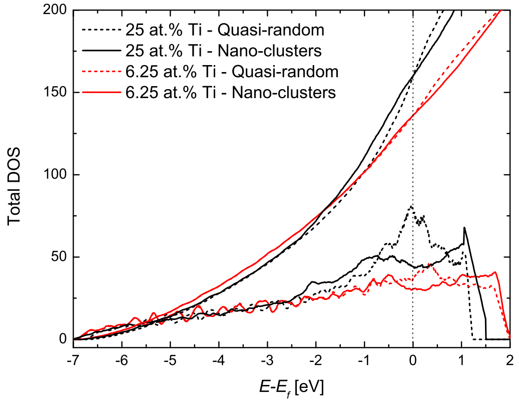

FIG. 6. (Color online) Comparison of total DOS for the nanocluster and quasirandom model for two different compositions. Upper lines show integrated total DOS.

of both experimental and calculated lattice parameters from Vegard's law. Can this also be rationalized along the lines discussed above? Just by considering the boundary conditions of binary mixing, namely, solid solution and complete phase separation, one would expect Vegard's law to work better the closer the system is to solid solution. A model for calculating the lattice parameters as a function of composition and short-range order in alloys was proposed already by Dienes[39] in 1958, showing some influence of ordering on departures from Vegard's law. Later, several examples of relations between dimensional variations and local ordering have been found experimentally, as presented in the review by Povolo and Mosca.[40] Thus the variations in experimental cell parameters and the failure to obey Vegard's law both in calculations and experimentally further support the occurrence of nanoclustering in the Mg-Ti system.

The segregated configuration displays an increase in volume relative to the quasirandom configuration for all concentrations of Ti. Thus there appears to be something in the mixing of Ti and Mg that leads to a negative deviation from Vegard's law, which is again counteracted by the formation of nanoclusters. Another interesting detail can be observed for the simplest case, the 1.56 at. % Ti composition with just a single Ti atom in the calculated unit cell. From Fig. 5 it can be seen that the calculated a axis is only slightly shorter than the value predicted by Vegard's law while the c axis shows a significant negative deviation. Thus already in the quasirandom substitution of Ti in Mg there is an intrinsic effect causing the c axis to decrease more than the a axis. If considering the compositions <20 at. % Ti it is clearly seen that arranging Ti in moderate nanoclusters is opposing this intrinsic decrease in the c axis. The composition 98.44 at. % Ti with a single Mg atom in a Ti matrix does not show the same degree of asymmetry in the deviation of the a and c axes. We will return to this point in the following section.

B. Electronic structure

The Hume-Rothery rules are frequently used to evaluate the occurrence of solid solubility. As Mg and Ti score high on three out of four criteria; they both have the same crystal structure, the atomic radii differs by less than 15% and the electronegativities are similar, the lack of solubility may come as a surprise. However, this leaves the criterion regarding valency, warranting an investigation of the electronic structure of the system. In the following section it is shown how the electronic structure changes between the two different models. Figure 6 gives total density of states (DOS) and

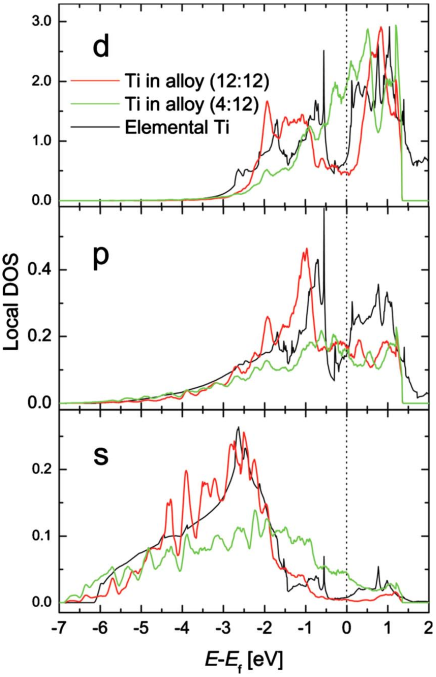

FIG. 7. (Color online) Local DOS for single Ti atoms in nanoclusters with 25 at. % Ti. The s, p, and d projections are shown in the bottom, mid, and top panels, respectively. Ti completely surrounded by other Ti atoms (12:12) is compared to Ti at the boundary of the nanocluster having only four nearest-neighbor Ti atoms (4:12) and to elemental Ti.

integrated total DOS for two different compositions. The segregation causes the valence states to retract from the Fermi level compared to those of the quasirandom distribution. The valence electrons are thus more strongly bonded as a result of segregation; this difference is larger the higher the content of Ti.

To investigate the local environment of different atoms in the segregated case local DOS was calculated using covalent radii as the Wigner-Seitz radii for the atoms, $r(\text{Mg}) = 1.41$ Å and $r(\text{Ti}) = 1.60$ Å.[41] Figure 7 shows an example of local DOS plots for 25 at. % Ti. Single Ti atoms in different sites are compared to the pure element. Figure 8 shows the corresponding results for Mg. For the Ti s states it is clearly seen how the Ti atom in the middle of the nanocluster resembles elemental Ti while the Ti atom at the interface has an s state very close to that of Mg. For the Ti p and d states the situation is the same, only with the states of the Ti atom in the middle of the nanocluster shifted *away* from the Fermi level compared to elemental Ti. In the Mg case the p states of the Mg atom without Ti neighbors are shifted *toward* the Fermi level. At first glance it may look like the Mg atom near the interface of the nanocluster is actually resembling elemental Mg more. However, a more careful consideration reveals that this is probably from the influence of the Ti p state, which has a peak at approximately the same energy.

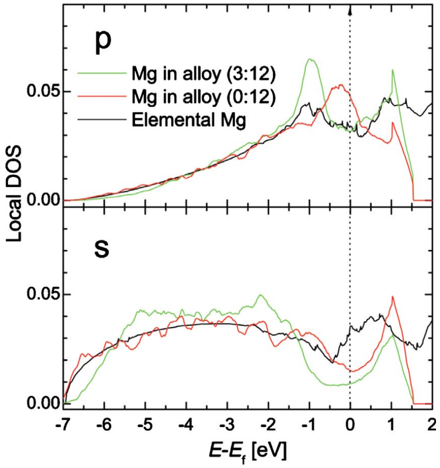

FIG. 8. (Color online) Local DOS for single Mg atoms in nanoclusters with 25 at. % Ti. The s and p projections are shown in the bottom and top panels, respectively. Mg at the boundary of the nanocluster having three nearest-neighbor Ti atoms (3:12) is compared to Mg without nearest-neighbor Ti atoms (0:12) and to elemental Mg.

What can be suspected from the DOS plots in Figs. 7 and 8 and confirmed from the integrated total DOS of *all* Ti atoms (not shown) is that both in the quasirandom and the nanocluster case Ti seems to have lost states to Mg. However, charge transfer from Ti to Mg is inconsistent with their electronegativity values and indicates that the topic should be investigated more closely. Bader analysis was carried out to describe single atoms in an alternative way.[42] In this approach the atoms are confined in volumes which surfaces are drawn perpendicular to minima in the charge density. While using a sphere for each atom leaves the voids in between unaccounted for, the Bader division will be able to pick up most of the charge present in the unit cell. Figure 9 shows the results for three different 12.5 at. % Ti models. Contrary to what was seen above, the Bader analysis shows that mixing Mg and Ti leads to charge transfer from Mg to Ti, thus Bader analysis was necessary to obtain a correct picture of the charge transfer in this system. Charge transfer from Mg to Ti is in agreement with their electronegativity values and the experimental findings of Mitchell *et al.*[20] The further a Ti atom is placed from another Ti atom, the more charge is drawn from Mg. It is clear that a sole Ti atom in a Mg matrix behaves very differently from a Ti atom in a Ti matrix. A Ti atom in the middle of a nanocluster ($N_{\text{Ti-Ti}} = 12$) has the least charge, less than that of the pure metal. By looking at the calculated average charge it is clear that the segregation affects the charge of both Mg and Ti in a way that brings it closer to the values for pure metals. The difference between the quasirandom and the nanocluster models is already considerable for the nanocluster consisting of only eight Ti atoms in a 64 atoms unit cell. Increasing the unit cell to 288 atoms with a nanocluster of 36 Ti atoms results in only minor

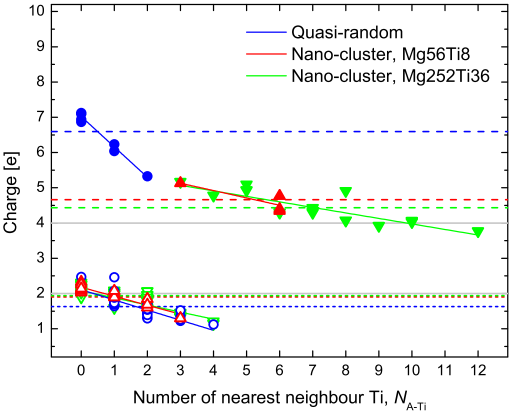

FIG. 9. (Color online) Result of Bader analysis for the composition 25 at. % Ti. Solid symbols represents Ti and open symbols represents Mg. The charge of each atom is plotted against the number of Ti atoms on the 12 nearest and second nearest-neighbor positions ($N_{\text{Ti-}A}, A=\text{Mg},\text{Ti}$). Variations in charge for identical $N_{\text{Ti-}A}$ are due to different configurations within the neighbor sphere. The linear fit for each species is included as a guide to the eyes. Dotted lines show the average charge for each species. Solid lines show the elemental charge for Mg ($2e$) and Ti ($4e$).

adjustments. This corresponds very well to the flattening of the curve in Fig. 3. Evidently a limited amount of Ti nearest neighbors is enough for Ti to experience an imitation of elemental state and thus the gain in energy upon further segregation becomes negligible.

Finally the difference in charge density between the alloy and the procrystal (a hypothetical material of noninteracting atoms with the same crystal structure) has been calculated. The largest drain of charge is found in the interstitial sites between Ti atoms inside the nanoclusters while the largest gain is around the Ti cores. The former helps explain the diverging results for the charge of local atoms presented above. Charge is also lost from the interstitial sites between Ti and Mg atoms at the interface as well as from the interstitial sites in the Mg rich area. Figure 10 shows isosurface plots of the charge difference for the quasirandom and nanocluster model with 12.5 at. % Ti. It offers a possible explanation for the previously mentioned asymmetry in the deviation of the a and c axes from Vegard's law. In the quasirandom arrangement the isosurface of a single Ti atom shows a distinct elongation in the c direction. However, placing just a few Ti atoms together in two layers in the c direction shaves off this elongation completely. This illustrates in yet another way how single Ti atoms in a Mg matrix behaves differently from Ti in elemental Ti. As stated above this can be counteracted even by Ti clusters of very limited size. However, the charge difference plots suggests that the orientation of the clusters is not indifferent, favoring bonds in the c direction. The corresponding structures with 12.5 at. % Mg do not show any clear orientational effects.

IV. CONCLUSIONS

Density functional calculations were used to investigate the $\text{Mg}_{100-y}\text{Ti}_y$ system with compositions $1.56 \leq y \leq 98.44$. The crystal structure, mixing enthalpy, and electronic structure were compared for two different distributions of Ti: quasirandom and segregated. It was found that although the relaxed crystal structures did not differ significantly in the two cases, for the Mg rich compositions the mixing enthalpy per Ti atom was lowered by ~0.5 eV when Ti was segregated into nanoclusters. This is in correspondence with experimental findings of chemical short-range order in the same material system.[18] As a consequence of the decrease in the mixing enthalpy upon clustering we propose the occurrence of short-range chemical order in all reported Mg-Ti samples with extended solubility limit. The substantial gain in energy upon clustering of only a few Ti atoms is in itself surprising considering the overwhelmingly large surface to bulk ratio of such particles. Further investigation revealed that the mixing enthalpy does in fact reach a minimum after which further increase in cluster size is of no consequence. This suggests that there is no direct transition between this formation of nanoclusters and the larger scale phase separation occurring in an equilibrium process.

The relaxed crystal structures were compared to experimental values from several sources and lattice-parameter variations as well as deviations from Vegard's law were discussed. Dependence of synthesis method on the size and shape of the nanoclusters is offered as an explanation for the large variation in the different experimental lattice param-

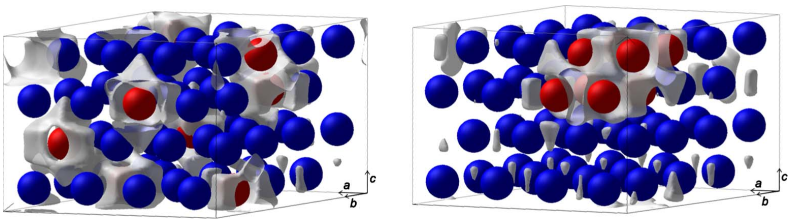

FIG. 10. (Color online) Isosurface plots of the charge difference for the quasirandom model with 12.5 at. % Ti distributed quasirandomly (left) and in nanoclusters (right). See the text for definition of the charge difference. The isosurfaces are drawn at a charge loss of 0.020 $e/\text{Å}^3$. The areas just inside each surface have experienced larger charge losses while the areas outside the surfaces have experienced smaller losses or gained charge. Charge gain occurs closer around the atomic sites, more for Ti than for Mg.

eters. Variations in cluster size and shape due to variations in sample preparation will in turn lead to variations in lattice parameters and inevitably to deviations from Vegard's law.

Electronic density of states calculations revealed that the electrons are more strongly bound in the nanocluster model than the quasirandom model. Local DOS calculations illustrated how segregated Ti forms a local environment resembling pure Ti while it was necessary to perform Bader analysis in order to obtain the correct picture of the charge transfer between Mg and Ti. Charge is transferred from Mg to Ti, consistent with their electronegativity values. Randomly distributed Ti atoms affect the charge distribution severely and the further the Ti atoms are apart the larger is the charge transfer from Mg. Thus, when Ti atoms are arranged in nanoclusters it helps both Ti and Mg to create a local environment resembling the elements in their pure state. The difference in charge transfer between the quasirandom and the nanocluster models is already considerable for the nanocluster consisting of only eight Ti atoms in a 64 atoms unit cell. Quadrupling the unit cell resulted in only minor adjustments, showing that a very limited amount of Ti nearest neighbors is sufficient for Ti to experience an imitation of elemental state and thus the driving force for further nucleation vanishes. Interpreting charge difference calculations in view of changes in the c/a ratio upon clustering suggested that there may also be a preferential orientation of the Ti-Ti bonds, along the c axis.

From the present work it is clear that Ti behaves markedly different in solution and in elemental form and that the microstructure of Mg-Ti solid solutions is formed in a complex process involving several factors. Inherently connected to the presence of single Ti atoms in a Mg matrix is some unwanted electronic behavior which the system opposes by clustering of Ti. However, the fact that just a handful of Ti atoms will do to achieve the desired effect indicates that the phenomenon of nanoscale clustering must be understood separately from the larger scale precipitation occurring in an equilibrium process. On top of this comes variations in cluster size and shape due to variations in sample preparation, which will in turn lead to the variations in lattice parameters seen for real samples.

---

*i.j.t.jensen@fys.uio.no

[1] J. Huiberts, R. Griessen, J. Rector, R. Wijngaarden, J. Dekker, D. de Groot, and N. Koeman, Nature (London) **380**, 231 (1996).

[2] P. van der Sluis, M. Ouwerkerk, and P. Duine, Appl. Phys. Lett. **70**, 3356 (1997).

[3] T. Richardson, J. Slack, R. Armitage, R. Kostecki, B. Farangis, and M. Rubin, Appl. Phys. Lett. **78**, 3047 (2001).

[4] E. Shalaan, H. Schmitt, and K. Ehses, Thin Solid Films **489**, 330 (2005).

[5] G. Srinivas, V. Sankaranarayanan, and S. Ramaprabhu, J. Appl. Phys. **104**, 064504 (2008).

[6] D. Borsa, A. Baldi, M. Pasturel, H. Schreuders, B. Dam, R. Griessen, P. Vermeulen, and P. Notten, Appl. Phys. Lett. **88**, 241910 (2006).

[7] S. Karazhanov, A. Ulyashin, P. Vajeeston, and P. Ravindran, Philos. Mag. **88**, 2461 (2008).

[8] M. Pasturel, M. Slaman, D. Borsa, H. Schreuders, B. Dam, and R. Griessen, Appl. Phys. Lett. **89**, 021913 (2006).

[9] R. Gremaud, C. Broedersz, D. Borsa, A. Borgschulte, P. Mauron, H. Schreuders, J. Rector, B. Dam, and R. Griessen, Adv. Mater. **19**, 2813 (2007).

[10] A. Zaluska, L. Zaluski, and J. O. Ström-Olsen, Appl. Phys. A: Mater. Sci. Process. **72**, 157 (2001).

[11] M. Dornheim, N. Eigen, G. Barkhordarian, T. Klassen, and R. Bormann, Adv. Eng. Mater. **8**, 377 (2006).

[12] F. von Zeppelin, H. Reule, and M. Hirscher, J. Alloys Compd. **330-332**, 723 (2002).

[13] J. F. Pelletier, J. Huot, M. Sutton, R. Schulz, A. R. Sandy, L. B. Lurio, and S. G. J. Mochrie, Phys. Rev. B **63**, 052103 (2001).

[14] X. Yao, C. Wu, A. Du, G. Lu, H. Cheng, S. Smith, J. Zou, and Y. He, J. Phys. Chem. B **110**, 11697 (2006).

[15] R. Niessen and P. Notten, Electrochem. Solid-State Lett. **8**, A534 (2005).

[16] D. M. Borsa, R. Gremaud, A. Baldi, H. Schreuders, J. H. Rector, B. Kooi, P. Vermeulen, P. H. L. Notten, B. Dam, and R. Griessen, Phys. Rev. B **75**, 205408 (2007).

[17] P. Vermeulen, H. Wondergem, P. Graat, D. Borsa, H. Schreuders, B. Dam, R. Griessen, and P. Notten, J. Mater. Chem. **18**, 3680 (2008).

[18] R. Gremaud, A. Baldi, M. Gonzalez-Silveira, B. Dam, and R. Griessen, Phys. Rev. B **77**, 144204 (2008).

[19] A. Baldi, R. Gremaud, D. Borsa, C. Baldè, A. van der Eerden, G. Kruijtzer, P. de Jongh, B. Dam, and R. Griessen, Int. J. Hydrogen Energy **34**, 1450 (2009).

[20] T. Mitchell, S. Diplas, P. Tsakiropoulos, J. F. Watts, and J. A. D. Matthew, Philos. Mag. A **82**, 841 (2002).

[21] P. Vermeulen, P. Graat, H. Wondergem, and P. Notten, Int. J. Hydrogen Energy **33**, 5646 (2008).

[22] B. Pauw, W. Kalisvaart, S. Tao, M. Koper, A. Jansen, and P. Notten, Acta Mater. **56**, 2948 (2008).

[23] S. Er, D. Tiwari, G. A. de Wijs, and G. Brocks, Phys. Rev. B **79**, 024105 (2009).

[24] G. Kresse and J. Furthmüller, Phys. Rev. B **54**, 11169 (1996).

[25] G. Kresse and J. Furthmüller, Comput. Mater. Sci. **6**, 15 (1996).

[26] G. Kresse and D. Joubert, Phys. Rev. B **59**, 1758 (1999).

[27] J. P. Perdew, K. Burke, and M. Ernzerhof, Phys. Rev. Lett. **77**, 3865 (1996).

[28] http://vaspview.sourceforge.net/

[29] D. A. Rowlands, A. Ernst, B. L. Gyorffy, and J. B. Staunton, Phys. Rev. B **73**, 165122 (2006).

[30] V. Vaithyanathan, C. Wolverton, and L. Q. Chen, Phys. Rev. Lett. **88**, 125503 (2002).

[31] G. Liang and R. Schultz, J. Mater. Sci. **38**, 1179 (2003).

[32] S. Rousselot, M.-P. Bichat, D. Guay, and L. Roué, J. Power Sources **175**, 621 (2008).

[33] B. Warren, B. Averbach, and B. Roberts, J. Appl. Phys. **22**, 1493 (1951).

[34] http://icsd.fiz-karlsruhe.de/, 2010.

[35] E. A. Owen, L. Pickup, and I. O. Roberts, Z. Kristallogr. **91**, 70 (1935).

[36] R. M. Wood, Proc. Phys. Soc. London **80**, 783 (1962).

[37] D. Wilkes, P. Goodwin, C. Ward-Close, K. Bagnall, and J.

Steeds, Mater. Lett. **27**, 47 (1996).

[38] O. M. Løvvik, O. Swang, and S. M. Opalka, J. Mater. Res. **20**, 3199 (2005).

[39] G. J. Dienes, Acta Mater. **6**, 278 (1958).

[40] F. Povolo and H. O. Mosca, Phys. Status Solidi A **164**, 609 (1997).

[41] B. Cordero, V. Gómez, A. Platero-Prats, M. Revés, J. Echeverría, E. Cremades, F. Barragán, and S. Alvarez, Dalton Trans. **2008**, 2832.

[42] G. Henkelman, A. Arnaldsson, and H. Jónsson, Comput. Mater. Sci. **36**, 354 (2006).

Paper III

Combined XPS and first principle study of meta-stable Mg-Ti thin films.

I.J.T. Jensen, O. M. Løvvik, H. Schreuders, B. Dam and S. Diplas

Surface and interface analysis **42**, 1140-1143 (2012)

Paper IV

Hydrogen induced stabilization of meta-stable Mg-Ti.

I.J.T. Jensen, S. Diplas, and O. M. Løvvik

Applied Physics Letters **100**, 111902 (2012)

APPLIED PHYSICS LETTERS **100**, 111902 (2012)

Hydrogen induced stabilization of meta-stable Mg-Ti

I. J. T. Jensen,[1,a)] S. Diplas,[2,3] and O. M. Løvvik[1,2]
[1]*Department of Physics, University of Oslo, P.O. Box 1048 Blindern, 0316 Oslo, Norway*
[2]*SINTEF Materials and Chemistry, P.O. Box 124 Blindern, 0314 Oslo, Norway*
[3]*Center for Materials Science and Nanotechnology, P.O. Box 1126 Blindern, 0318 Oslo, Norway*

(Received 1 December 2011; accepted 18 February 2012; published online 12 March 2012)

The hydrogenation of $Mg_{0.8125}Ti_{0.1875}$ was investigated by density functional calculations, using a model where Ti was segregated into nano-clusters. Introducing small amounts of hydrogen resulted in significant stabilization, with the mixing enthalpy (cohesive energy relative to standard state elements) becoming negative for hydrogen contents exceeding 0.07 H per metal. H prefers sites on the interface between Mg and Ti, with hydrogenation energies down to –115 kJ/(mol H_2). Trapping of H on these very stable sites is proposed as an alternative explanation to why the reversibility of Mg-Ti thin films, which are initially meta-stable, can be preserved over many cycles of hydrogenation. © *2012 American Institute of Physics*. [http://dx.doi.org/10.1063/1.3692578]

$Mg_{1-y}Ti_yH_x$ thin films behave as switchable mirrors, belonging to a group of materials with remarkable optical properties. Upon hydrogenation $Mg_{1-y}Ti_yH_x$ goes through drastic optical changes, from reflecting in the metallic state to highly absorbent in the hydride state.[1] The tunability of the electrical and optical properties makes this group of materials interesting for a variety of applications ranging from coatings on solar collectors[1] and smart windows[2] to optical hydrogen sensors[3] and semiconductor devices such as solar cells.[4] Furthermore, excellent hydrogen storage capacity has been reported for Mg-Ti-H thin films of different compositions.[5] Hydrogen uptake is fast and can be done at room temperature and low H_2 pressure. Experimentally one finds that the hydrogen uptake is somewhat less than the stoichiometric 2 H per metal.[6] Mg is in itself an interesting hydrogen storage material due to its low weight, but unfortunately the high thermal stability and slow kinetics make it unsuited for practical use. Circumventing these problems have proven difficult, in spite of extensive efforts like including additives[7,8] and/or manipulating the particle size down to the nanoscale.[7,9–11] A particular issue is obtaining good hydrogen storage properties over many cycles, as many Mg-based systems tend to disproportionate upon hydrogenation.[12,13] $Mg_{1-y}Ti_yH_x$ thin films on the other hand maintain favourable hydrogen storage properties upon repeated cycling, in spite of Mg and Ti being immiscible.[14]

The lack of stable binary phases of Mg and Ti and the near zero solubility of Ti in Mg have raised questions about the geometric structure of Mg-Ti thin films at the atomic scale. Mg-Ti thin films can be made by non-equilibrium synthesis procedures like magnetron sputtering, in which no large-scale separation of Mg and Ti has been found.[6,15] However, evidence for chemical short range order was discovered both from simulation of optical isotherms obtained by the hydrogenography technique[16] and a combination of X-ray diffraction and Extended X-ray absorbtion fine structure spectroscopy.[17] In a recent work, we used density functional theory (DFT) calculations to explore the possibility of nano-scale segregation, finding that the formation enthalpy per Ti atom was indeed lowered by up to 0.5 eV when Ti was arranged in nano-clusters rather than distributed quasi-randomly.[18] To explain the stability of the structure upon hydrogen cycling, it has been suggested that TiH_2 is formed first and that the coincidental volumetric match between TiH_2 and unhydrogenated Mg relieves strain in the structure, removing the drive for Ti and Mg to separate.[6] In a recent study,[19] a segregated fcc hydride structure of composition $Mg_{0.75}Ti_{0.25}$ was reported to be stable already at very low H contents. This is in apparent correspondence with some of the experimental findings but does not explain why the system returns to the initial metal phase upon dehydrogenation. How meta-stable Mg-Ti thin films can preserve reversibility upon several cycles of hydrogenation is still not fully understood.

In this work, we investigate this reversibility by looking at the hydrogenation of $Mg_{1-y}Ti_y$ with $y = 0.1875$. We show that when Ti is arranged in nano-clusters the structure is stabilized upon introduction of small amounts of hydrogen. H prefers sites at the interface between the matrix and the nano-clusters and we claim that it is in fact these very stable H sites on the Mg-Ti interface that are responsible for the repeated reversibility of the system, rather than the volumetric equality of Mg and TiH_2. Our results are seen in view of the experimental findings for magnetron sputtered Mg-Ti thin films, where a kinetically stable initial material with Ti finely dispersed in the Mg matrix has been observed.[16,17]

DFT calculations at the PBE-GGA level[20] were performed for a $Mg_{81.25}Ti_{18.75}$ composition using the Vienna *ab-initio* simulation package (VASP).[21,22] For the metal phase (hcp), a $4 \times 4 \times 2$ Mg unit cell (64 atoms) was used as a starting point, see Ref. 18 for more details. We found that the TiH_2 type hydride structure is more stable than the MgH_2-type for this composition. Thus for the hydride phase, a $2 \times 2 \times 3$ TiH_2-type (fcc) unit cell (48 atoms) was used, with the experimental lattice parameters of Vermeulen *et al.*[23] as a starting point. Ti was segregated into *nano-clusters*, see Figure 1. In both structures, H has the choice of occupying octahedral (oct) or tetrahedral (tet) sites and several hydrogen configurations and contents were investigated. Total energy structural minimizations were performed, with volume, lattice parameters, and atom positions

---

[a)] Electronic mail: i.j.t.jensen@fys.uio.no.

Downloaded 12 Mar 2012 to 129.240.152.33. Redistribution subject to AIP license or copyright; see http://apl.aip.org/about/rights_and_permissions

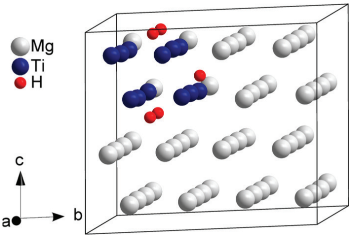

FIG. 1. (Color online) Example of nano-cluster model with segregated Ti: metal (fcc) structure with 5 H atoms.

allowed to change simultaneously. The mixing enthalpy for $Mg_{1-y}Ti_yH_x$ was calculated as follows:

$$\Delta H_f = E_{\mathrm{Mg-Ti-H}} - (1-y)E_{\mathrm{Mg}} - yE_{\mathrm{Ti}} - \frac{x}{2}E_{\mathrm{H_2}}, \quad (1)$$

where $y = 0.1875$ and $E_{\mathrm{Mg-Ti-H}}, E_{\mathrm{Mg}}, E_{\mathrm{Ti}}$, and $E_{\mathrm{H_2}}$ are the calculated total electronic energies of alloy, pure Mg, pure Ti, and H_2 gas, respectively. For comparisons, the enthalpy of formation per H_2 was used. The hydrogenation energy was defined as $E_{\mathrm{Mg-Ti-H}} - (E_{\mathrm{Mg-Ti}} + \frac{x}{2}E_{\mathrm{H_2}})$, where the former is either fcc hydride structure or hcp metal structure with H and the latter is the hcp metal structure without H.

In Figure 2, the mixing enthalpy ΔH_f versus the number of nearest neighbor Ti atoms (nn_{Ti}) is plotted for a single H atom placed at different sites in the hcp metal structure. The results are compared to the mixing enthalpy of the same structure without H, revealing that introducing H to the sites with $nn_{\mathrm{Ti}} \geq 1$ has a stabilizing effect on the system. From Figure 2, it is clear that the oct sites are the most energetically favourable in general and that the sites with equal number of Mg and Ti nearest neighbors ($nn_{\mathrm{Ti}} = 3$) stand out among them. There are two different types of sites with $nn_{\mathrm{Ti}} = 3$; the most stable ones lie between Mg and Ti in the c direction, while the remaining sites are placed around the Ti cluster in the ab plane. This anisotropy is consistent with our previous work, where we found that the largest difference in the electronic structure between nano-cluster and quasi-random arrangement occurred in the c direction.[18] Evidently, modifications in the c direction plays a special role in lowering the mixing enthalpy of the system.

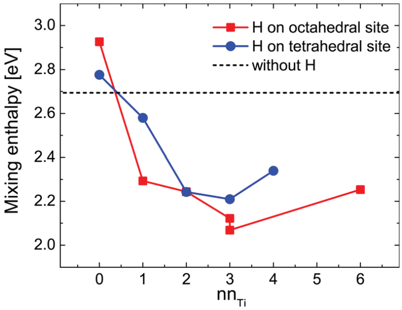

FIG. 2. (Color online) The mixing enthalpy ΔH_f of $Mg_{0.8125}Ti_{0.1875}$ with a single H atom placed at different sites in the metal structure. The sites are labeled by the number of Ti atoms among the nearest metal neighbors of H.

For further hydrogenation of the hcp metal structure, we chose to fill the oct sites. The occurrence of each site with $nn_{\mathrm{Ti}} = 6, 3, 2, 1$ and 0 in the unit cell is 2, 10, 8, 14, and 30, respectively. Figure 3 shows the calculated mixing enthalpy per H_2 and hydrogenation energy of different metal and hydride configurations. A gradual filling of the 10 available sites with $nn_{\mathrm{Ti}} = 3$ shows that the mixing enthalpy of the metallic hcp structure turns negative for small amounts of H. By line fitting the mixing enthalpy, the turning point is found to occur at a composition $Mg_{0.8125}Ti_{0.1875}H_x$ with $x = 0.07$; corresponding to between 4 and 5 H atoms added to the 64 atom unit cell. At this level of H filling, the fcc hydride structure is still far from stable, as can be seen in Figure 3. This is inconsistent with the work of Tao *et al.*[19] However, the Ti atoms in their segregated structure appear to be connected in one direction. The discrepancy in results illustrates the importance of choosing a sufficiently large unit cell to avoid unphysical configurations like strings or sheets instead of clusters of Ti.

From Figure 3, it is clear that H prefers to occupy the sites with $nn_{\mathrm{Ti}} = 3$ at the cluster-matrix interface rather than the sites with $nn_{\mathrm{Ti}} = 6$ inside the Ti nano-clusters. For two H atoms (x = 0.0313), the sites with $nn_{\mathrm{Ti}} = 3$ are more stable than those with $nn_{\mathrm{Ti}} = 6$ by more than 30 kJ/(mol H_2). For increasing amounts of H, the trend weakens and after filling all 10 sites with $nn_{\mathrm{Ti}} = 3$ ($x = 0.1563$), the hydrogenation sequence becomes more ambiguous. For instance, occupying the two $nn_{\mathrm{Ti}} = 6$ sites is more energetically favourable than occupying two of the $nn_{\mathrm{Ti}} = 2$ sites (12 H atoms, $x = 0.1875$), but full occupation of the $nn_{\mathrm{Ti}} = 2$ sites is more favourable than having two replaced by $nn_{\mathrm{Ti}} = 6$ (18 H atoms,

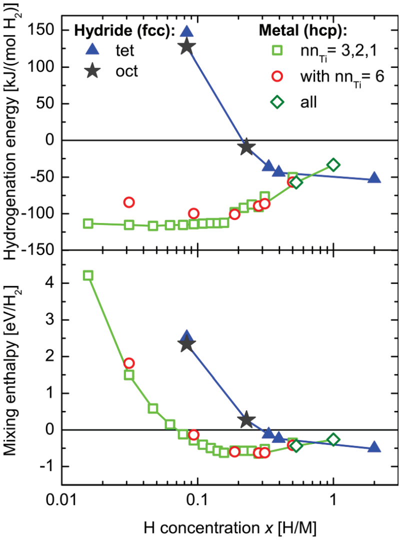

FIG. 3. (Color online) Calculated mixing enthalpy per H_2 and hydrogenation energy for hcp metal and fcc hydride structures. In the metal, the octahedral interface sites are filled gradually in the order $nn_{\mathrm{Ti}} = 3, 2, 1$ (squares) or with two sites replaced by $nn_{\mathrm{Ti}} = 6$ (circles). All oct sites with $nn_{\mathrm{Ti}} \geq 1$ and all oct sites in total were also calculated (diamonds). For the hydride, both oct (stars) and tet sites (triangles) were tested.

Downloaded 12 Mar 2012 to 129.240.152.33. Redistribution subject to AIP license or copyright; see http://apl.aip.org/about/rights_and_permissions

$x = 0.2813$). However, the differences in enthalpy per H_2 were modest, 0.03 eV or less. In any case, it is clear that all the sites with $nn_{Ti} \geq 1$ are filled before the pure Mg sites come into use. In our previous paper,[18] we showed how arranging Ti in nano-clusters rather than in a quasi-random manner lowered the mixing enthalpy. We found that a significant charge transfer takes place from Mg to Ti but that this effect is reduced when Ti is arranged in nano-clusters, primarily for the Ti atoms inside the clusters. A similar analysis of the present model suggests that H accepts this extra charge, allowing even Ti on the cluster interface to return to near elemental charge.

Based on our results, we conclude that the stabilization due to H on the Mg-Ti interface is a good explanation for the reversibility of the system. The H bonding at the $nn_{Ti} = 3$ sites is very strong (see Figure 3), with hydrogenation energies below –115 kJ/(mol H_2). To put such numbers into perspective, the rule of thumb says that for an equilibrium pressure of 1 bar H_2 at 300 K, the enthalpy change is -39.2 kJ/(mol H_2).[24] Thus the hydrogenation energies are so low that the hydrogen atoms are likely to be trapped at the Mg-Ti interface sites for all relevant experimental conditions. This way the H atoms at the cluster-matrix interface promote a return to the metal structure upon dehydrogenation. The coincidental volumetric match between Mg and TiH_2 pointed out by Borsa *et al.*[6] is certainly intriguing, but does not seem to be a necessary requirement. Our approach also provides a reasonable explanation to why $Mg_{1-y}Ti_yH_x$ will only store about 1.7 H reversibly. In our model, the $nn_{Ti} = 3$ sites, which have the lowest hydrogenation energy, only amounts to a composition of 0.16 H per metal, but if sites with $nn_{Ti} = 2$ and 6 are also included the composition becomes 0.31 H per metal. It is likely that this amount of H will be trapped in the material as the hydrogenation energy is below -75 kJ/(mol H_2) for all these sites. One should also remember that the number of available sites in and around Ti will depend on the shape and size of the nano-clusters.

To find out more about the phase transformation from metal to hydride structure, various compositions and configurations of the fcc hydride structure have also been investigated. For low hydrogen contents, the model with H in oct positions had the lowest mixing enthalpy per H_2, while for full occupancy hydrogen resides in the tet voids similar to in TiH_2.[25] Compared to the hcp metal structure, a significantly higher H content is needed to stabilize the fcc hydride structure. Naively one might expect the phase transformation between metal and hydride phase to occur at half occupancy, when all the oct sites are filled and it becomes necessary to start using the tet sites. However, Figure 3 gives reason to suspect that the transformation happens at lower hydrogen contents, around 0.7 H per metal. At this composition, all the sites with $nn_{Ti} \geq 1$ are occupied. TiH_2 first starts to form inside the nano-clusters and as the sites in the Mg matrix come into play, the whole system transforms from Mg-type to TiH_2-type structure

So far, we have calculated the hydrogenation energy with hydrogen in the gas phase as the reference. However, one could argue that TiH_2 is a more relevant reference phase due to its high stability. We have calculated the hydrogenation energy of TiH_2 to be -126 kJ/(mol H_2), which is even lower than the values calculated for hydrogen in Mg-Ti. However, TiH_x is not as stable for the first absorbed hydrogen atoms. When calculating the enthalpy for TiH_x with $x = 0.25$, $1, 1.25$ and 1.5, we found that a hydrogen to Ti ratio between 1 and 1.5 is necessary for bulk TiH_x to compete with the stability of hydrogen at sites with $nn_{Ti} = 3$ in the segregated model. In our system, this corresponds to at least 12 H atoms. Thus, at low hydrogen content, the thermodynamic driving force to create bulk TiH_2 is greatly reduced for a real sample with Ti already arranged in nano-clusters. Furthermore, it is seen experimentally that above a certain Ti content, the whole Mg-Ti system adapts the TiH_2-type structure upon hydrogenation.[23] This gives a qualitative indication of the importance of the Mg-Ti interface and further supports the view that the properties of bulk TiH_2 are not directly transferable to a system with Ti arranged in nano-clusters.

In conclusion, the meta-stable $Mg_{0.8125}Ti_{0.1875}H_x$ system is found to be stabilized upon introduction of small amounts of H ($x = 0.07$). The H atoms prefer sites on the interface between Ti nano-clusters and the Mg matrix, rather than the sites in the pure Ti environment inside the Ti nano-clusters. At these sites, the hydrogenation energy is very low, down to around –115 kJ/(mol H $_2$). We state that these very stable H sites on the Mg-Ti interface are the main cause of the reversibility of the system. This also gives a probable explanation for why experimentally only 1.7 H per metal can be stored reversibly, as the missing 0.3 H per metal remains in the metal structure after dehydrogenation to keep it stable. Our results suggest that the phase transformation from metal to hydride occurs when all the sites with $nn_{Ti} \geq 1$ are occupied and the sites within the Mg matrix come into use.

A grant of computational time from the NOTUR consortium is gratefully acknowledged.

[1] D. M. Borsa, A. Baldi, M. Pasturel, H. Schreuders, B. Dam, R. Griessen, P. Vermeulen, and P. H. L. Notten, Appl. Phys. Lett. **88**, 241910 (2006).
[2] A. Anders, J. L. Slack, and T. J. Richardson, Thin Solid Films **517**, 1021 (2008).
[3] M. Pasturel, M. Slaman, D. M. Borsa, H. Schreuders, B. Dam, and R. Griessen, Appl. Phys. Lett. **89**, 021913 (2006).
[4] S. Z. Karazhanov, A. G. Ulyashin, P. Vajeeston, and P. Ravindran, Philos. Mag. **88**, 2461 (2008).
[5] R. A. H. Niessen and P. H. L. Notten, Electrochem. Solid-State Lett. **8**, A534 (2005).
[6] D. M. Borsa, R. Gremaud, A. Baldi, H. Schreuders, J. H. Rector, B. Kooi, P. Vermeulen, P. H. L. Notten, B. Dam, and R. Griessen, Phys. Rev. B **75**, 205408 (2007).
[7] A. Zaluska, L. Zaluski, and J. O. Strm-Olsen, Appl. Phys. A: Mater. Sci. Process **72**, 157 (2001).
[8] M. Dornheim, N. Eigen, G. Barkhordarian, T. Klassen, and R. Bormann, Adv. Eng. Mater. **8**, 377 (2006).
[9] F. von Zeppelin, H. Reule, and M. Hirscher, J. Alloys Compd. **330**, 723 (2002).
[10] J. F. Pelletier, J. Huot, M. Sutton, R. Schulz, A. R. Sandy, L. B. Lurio, and S. G. J. Mochrie, Phys. Rev. B **63**, 052103 (2001).
[11] X. D. Yao, C. Z. Wu, A. J. Du, G. Q. Lu, H. M. Cheng, S. C. Smith, J. Zou, and Y. He, J. Phys. Chem. B **110**, 11697 (2006).
[12] D. G. Nagengast, A. T. M. van Gogh, E. S. Kooij, B. Dam, and R. Griessen, Appl. Phys. Lett. **75**, 2050 (1999).
[13] D. Sun, F. Gingl, Y. Nakamura, H. Enoki, M. Bououdina, and E. Akiba, J. Alloys Compd. **333**, 103 (2002).
[14] P. Vermeulen, R. A. H. Niessen, and P. H. L. Notten, Electrochem. Commun. **8**, 27 (2006).
[15] P. Vermeulen, H. J. Wondergem, P. C. J. Graat, D. M. Borsa, H. Schreuders, B. Dam, R. Griessen, and P. H. L. Notten, J. Mater. Chem. **18**, 3680 (2008).

Downloaded 12 Mar 2012 to 129.240.152.33. Redistribution subject to AIP license or copyright; see http://apl.aip.org/about/rights_and_permissions

[16] R. Gremaud, A. Baldi, M. Gonzalez-Silveira, B. Dam, and R. Griessen, Phys. Rev. B **77**, 144204 (2008).

[17] A. Baldi, R. Gremaud, D. M. Borsa, C. P. Bald, A. M. J. van der Eerden, G. L. Kruijtzer, P. E. de Jongh, B. Dam, and R. Griessen, Int. J. Hydrogen Energy **34**, 1450 (2009).

[18] I. J. T. Jensen, S. Diplas, and O. M. Lvvik, Phys. Rev. B **82**, 174121 (2010).

[19] S. X. Tao, P. H. L. Notten, R. A. van Santen, and A. P. J. Jansen, J. Alloys Compd. **509**, 210 (2011).

[20] J. P. Perdew, J. A. Chevary, S. H. Vosko, K. A. Jackson, M. R. Pederson, D. J. Singh, and C. Fiolhais, Phys. Rev. B **46**, 6671 (1992).

[21] G. Kresse and J. Furthmller, Phys. Rev. B **54**, 11169 (1996).

[22] G. Kresse and J. Furthmller, Comput. Mater. Sci. **6**, 15 (1996).

[23] P. Vermeulen, P. C. J. Graat, H. J. Wondergem, and P. H. L. Notten, Int. J. Hydrogen Energy **33**, 5646 (2008).

[24] A. Zttel, Naturwiss. **91**, 157 (2004).

[25] S. Er, D. Tiwari, G. A. de Wijs, and G. Brocks, Phys. Rev. B **79**, 024105 (2009).

Downloaded 12 Mar 2012 to 129.240.152.33. Redistribution subject to AIP license or copyright; see http://apl.aip.org/about/rights_and_permissions

Paper V

X-ray photoelectron spectroscopy investigation of magnetron sputtered Mg-Ti-H thin films.

I.J.T. Jensen, A. Thøgersen, O. M. Løvvik, H. Schreuders, B. Dam, and S. Diplas

Submitted to International journal of hydrogen energy (2012)

Paper VI

High energy XPS and X-AES study of $Mg_{80}Ti_{20}$ thin films with and without hydrogen

I.J.T. Jensen, A. Thøgersen, O. M. Løvvik, B. Dam,H. Schreuders, J. Watts and S. Diplas

In preparation